

NAVAL POSTGRADUATE SCHOOL

Monterey, California



THESIS

**DEVELOPMENT OF PRECISION POINTING
CONTROLLERS WITH AND WITHOUT VIBRATION
SUPPRESSION FOR THE NPS PRECISION POINTING
HEXAPOD**

by

Ronald Michael Bishop Jr.

December 2002

Thesis Advisor:
Second Reader:

Brij Agrawal
Hong-Jen Chen

Approved for public release; distribution is unlimited

THIS PAGE INTENTIONALLY LEFT BLANK

REPORT DOCUMENTATION PAGE			<i>Form Approved OMB No. 0704-0188</i>	
Public reporting burden for this collection of information is estimated to average 1 hour per response, including the time for reviewing instruction, searching existing data sources, gathering and maintaining the data needed, and completing and reviewing the collection of information. Send comments regarding this burden estimate or any other aspect of this collection of information, including suggestions for reducing this burden, to Washington headquarters Services, Directorate for Information Operations and Reports, 1215 Jefferson Davis Highway, Suite 1204, Arlington, VA 22202-4302, and to the Office of Management and Budget, Paperwork Reduction Project (0704-0188) Washington DC 20503.				
1. AGENCY USE ONLY (Leave blank)		2. REPORT DATE December 2002	3. REPORT TYPE AND DATES COVERED Engineer's Thesis	
4. TITLE AND SUBTITLE: Development of Precision Pointing Controllers with and Without Vibration Suppression for the NPS Precision Pointing Hexapod			5. FUNDING NUMBERS	
6. AUTHOR(S) Ronald M. Bishop, Jr.				
7. PERFORMING ORGANIZATION NAME(S) AND ADDRESS(ES) Naval Postgraduate School Monterey, CA 93943-5000			8. PERFORMING ORGANIZATION REPORT NUMBER	
9. SPONSORING /MONITORING AGENCY NAME(S) AND ADDRESS(ES) N/A			10. SPONSORING/MONITORING AGENCY REPORT NUMBER	
11. SUPPLEMENTARY NOTES The views expressed in this thesis are those of the author and do not reflect the official policy or position of the Department of Defense or the U.S. Government.				
12a. DISTRIBUTION / AVAILABILITY STATEMENT Approved for public release; distribution is unlimited			12b. DISTRIBUTION CODE	
13. ABSTRACT (maximum 200 words) <p>Satellite optical payloads demand better vibration control and finer precision pointing than ever before. Fortunately, the Stewart-Gough platform offers the potential of accomplishing both of these simultaneously.</p> <p>Using the Precision Pointing Hexapod at NPS (a Stewart-Gough platform), several controllers for precision pointing, with and without vibration disturbances, were developed. Unlike the traditional means of pointing a hexapod, (i.e. sensing and controlling strut length to orient payload), this research used the payload orientation derived from payload mounted position sensors to determine orientation and provide feedback to the actuator controller. Small and large angle controllers were developed and evaluated for accuracy using static pointing and dynamic tracking tasks. The pointing controllers were then added to an Adaptive Disturbance Canceller and evaluated for pointing accuracy and vibration suppression performance given a single tone disturbance.</p> <p>The results showed a static pointing accuracy of $\pm 0.008^\circ$ and a dynamic pointing accuracy ranging from $\pm 0.05^\circ$ to $\pm 0.2^\circ$, depending on the size and speed of the circular trajectory. Vibration suppression down to the noise floor was achieved in all static orientations tested. As for dynamic circle-tracking performance, at least a 20 dB reduction in the fundamental disturbance was obtained without degradation in pointing accuracy.</p>				
14. SUBJECT TERMS Precision Pointing, Hexapod, Steward Platform, Vibration Suppression, Adaptive Disturbance Canceller			15. NUMBER OF PAGES 117	
			16. PRICE CODE	
17. SECURITY CLASSIFICATION OF REPORT Unclassified	18. SECURITY CLASSIFICATION OF THIS PAGE Unclassified	19. SECURITY CLASSIFICATION OF ABSTRACT Unclassified	20. LIMITATION OF ABSTRACT UL	

THIS PAGE INTENTIONALLY LEFT BLANK

Approved for public release; distribution is unlimited

**DEVELOPMENT OF PRECISION POINTING CONTROLLERS WITH AND
WITHOUT VIBRATION SUPPRESSION FOR THE NPS PRECISION
POINTING HEXAPOD**

Ronald M. Bishop, Jr.
Lieutenant Commander, United States Navy
B.S., United States Naval Academy, 1991

Submitted in partial fulfillment of the
requirements for the degree of

AERONAUTICAL AND ASTRONAUTICAL ENGINEER DEGREE

and

MASTER OF SCIENCE IN ASTRONAUTICAL ENGINEERING

from the

**NAVAL POSTGRADUATE SCHOOL
December 2002**

Author: Ronald M. Bishop, Jr.

Approved by: Brij Agrawal, Thesis Advisor

Hong-Jen Chen, Second Reader

Max Platzer, Chairman
Department Aeronautics and Astronautics

THIS PAGE INTENTIONALLY LEFT BLANK

ABSTRACT

Satellite optical payloads demand better vibration control and finer precision pointing than ever before. Fortunately, the Stewart-Gough platform offers the potential of accomplishing both of these simultaneously.

Using the Precision Pointing Hexapod at NPS (a Stewart-Gough platform), several controllers for precision pointing, with and without vibration disturbances, were developed. Unlike the traditional means of pointing a hexapod, (i.e. sensing and controlling strut length to orient payload), this research used the payload orientation derived from payload mounted position sensors to determine orientation and provide feedback to the actuator controller. Small and large angle controllers were developed and evaluated for accuracy using static pointing and dynamic tracking tasks. The pointing controllers were then added to an Adaptive Disturbance Canceller and evaluated for pointing accuracy and vibration suppression performance given a single tone disturbance.

The results showed a static pointing accuracy of $\pm 0.008^\circ$ and a dynamic pointing accuracy ranging from $\pm 0.05^\circ$ to $\pm 0.2^\circ$, depending on the size and speed of the circular trajectory. Vibration suppression down to the noise floor was achieved in all static orientations tested. As for dynamic circle-tracking performance, at least a 20 dB reduction in the fundamental disturbance was obtained without degradation in pointing accuracy.

THIS PAGE INTENTIONALLY LEFT BLANK

TABLE OF CONTENTS

I.	INTRODUCTION.....	1
A.	MOTIVATION	1
B.	OBJECTIVES	2
C.	HISTORICAL BACKGROUND.....	2
II.	HARDWARE DESCRIPTION.....	7
A.	OVERVIEW	7
B.	PRECISION POINTING HEXAPOD	8
III.	MATHEMATICAL ANALYSIS	19
A.	COORDINATE SYSTEM.....	19
B.	POSITION ANALYSIS OF STEWART-GOUGH PLATFORM.....	21
C.	ANGULAR VELOCITY AND ACCELERATION ANALYSIS OF A STEWART-GOUGH PLATFORM	21
D.	JACOBIAN OF A STEWART-GOUGH PLATFORM.....	22
E.	STATIC FORCE ANALYSIS	23
F.	PAYLOAD VERTICAL SENSOR CONFIGURATION ANALYSIS.....	24
G.	ADAPTIVE DISTURBANCE CANCELLER ANALYSIS	25
IV.	PRECISION POINTING CONTROLLER DEVELOPMENT AND EXPERIMENTAL RESULTS.....	27
A.	SCOPE	27
B.	EXPERIMENTAL SETUP AND CALIBRATION.....	28
C.	SMALL ANGLE CONTROLLER (JACOBIAN MODEL)	36
D.	LARGE ANGLE CONTROLLER MODEL	56
V.	PRECISION POINTING CONTROLLER WITH VIBRATION SUPPRESSION EXPERIMENTAL RESULTS	65
A.	SCOPE AND SETUP.....	65
B.	POINTING CONTROLLER PERFORMANCE WITH SINGLE TONE (40 HZ) DISTURBANCE.....	66
C.	BASELINE VIBRATION SUPPRESSION PERFORMANCE OF THE ADAPTIVE DISTURBANCE CANCELLER.....	69
D.	COMBINED VIBRATION SUPPRESSION AND PRECISION POINTING RESULTS	71
VI.	CONCLUSIONS AND RECOMMENDATIONS	81
A.	CONCLUSIONS	81
B.	RECOMMENDATIONS.....	83
	LIST OF REFERENCES	85
	APPENDIX A	89
	INITIAL DISTRIBUTION LIST	99

THIS PAGE INTENTIONALLY LEFT BLANK

LIST OF FIGURES

Figure 1	Nominal Stewart-Gough Platform (from [18])	4
Figure 2	Fault-Tolerant Decoupled Pointing Approach.....	6
Figure 3	Precision Pointing Hexapod Experiment Setup.....	7
Figure 4	Precision Pointing Hexapod.....	8
Figure 5	Hexapod Modes	8
Figure 6	PPH Strut Actuator	10
Figure 7	PPH Power Supply.....	11
Figure 8	Position Sensing Module and Amplifier.....	11
Figure 9	The KD-2300 Measuring System with Sensor	13
Figure 10	The KD-2300 Target Configuration	14
Figure 11	The KD-2300 Sensor layout top view	14
Figure 12	PPH Accelerometers	15
Figure 13	Aura Bass Shaker and Custom Adapter.....	16
Figure 14	dSPACE Connection Panel.....	17
Figure 15	Stewart-Gough Platform Coordinate Frames (from [18])	19
Figure 16	Adaptive Disturbance Canceller	25
Figure 17	Typical Control Desk Operator Interface	29
Figure 18	Position Sensing Device Angular Measurement and Error Illustration.....	30
Figure 19	Differences in Kaman and PSD Sensor Angular Displacement Measurements for Rotations about the X-axis.....	32
Figure 20	Differences in Kaman and PSD Sensor Angular Displacement Measurements for Rotations about the Y-axis.....	32
Figure 21	Sensor Noise Induced Displacement Error	34
Figure 22	Sensor Noise Induced Angular Displacement Error	34
Figure 23	Sensor-to-Target Offset Angle Error	35
Figure 24	Small Angle controller Model	36
Figure 25	Response to Single-Axis Rotations using the Manufacturer provided Transformation Matrix.....	37
Figure 26	Response to Single-Axis Rotations using the Derived Jacobian Matrix	37
Figure 27	Error Comparison of the Different Transformation Matrices.....	38
Figure 28	PID Controller Block Diagram	39
Figure 29	Bode Diagram for the Standard PID Compensator ($K_p=2$, $K_i=6$, and $K_d=0.17$).....	40
Figure 30	ϕ and θ Errors for Static Commands.....	41
Figure 31	PID Transient Performance for Simultaneous $+1^\circ$ Rotations about the x and y-axes	41
Figure 32	Static Hunting about the X-axis.....	42
Figure 33	Commanded and Actual Trajectories for Single Axis Rotations.....	43
Figure 34	Differences between Open Loop and Closed Loop ϕ and θ Errors for Single Axis Rotations	43
Figure 35	Nominal Circular Tracking Trajectories ($\pm 1^\circ$ at 0.1 Hz).....	44

Figure 36	ϕ and θ Errors for Nominal Circular Tracking Trajectories($\pm 1^\circ$ at 0.1 Hz)	44
Figure 37	Actuator Voltage Commands for Nominal Circular Trajectory	46
Figure 38	ϕ and θ Errors Corresponding to 0.1 Hz Circular Trajectories for Various Radii.....	47
Figure 39	ϕ and θ Errors Corresponding to 2.0 Hz Circular Trajectories for Various Radii.....	47
Figure 40	ϕ and θ Errors Corresponding to Clockwise, 1.0° Radius, Circular Trajectories for Various Tracking Speeds	48
Figure 41	ϕ and θ Errors Corresponding to Counter-Clockwise, 1.0° Radius, Circular Trajectories for Various Tracking Speeds	48
Figure 42	Circular Tracking Trajectories for Various Tracking Speeds (1° radius).....	49
Figure 43	Modified PID Compensator Block Diagram	50
Figure 44	Comparison of ϕ and θ Errors for Static Commands Between PID and Modified PID Compensators	51
Figure 45	Modified PID Compensator Transient Performance for Simultaneous $+1^\circ$ Rotations about the x and y-axes	51
Figure 46	Commanded and Actual Trajectories for Single Axis Rotations using the Modified PID Compensator.....	52
Figure 47	Differences in the ϕ and θ Errors for Single Axis Rotations of the PID and Modified PID Compensators	53
Figure 48	Comparison of the Nominal Circular Tracking Trajectories between the PID and Modified PID Compensators	54
Figure 49	Comparison of ϕ and θ Errors for the Nominal Circular Tracking Trajectories between the PID and Modified PID Compensators.....	54
Figure 50	ϕ and θ Errors Corresponding to 0.1 Hz Circular Trajectories for Various Radii using the Modified PID Compensator.....	55
Figure 51	ϕ and θ Errors Corresponding to Clockwise, 1.0° Radius, Circular Trajectories for Various Tracking Speeds using the Modified PID Compensator	55
Figure 52	Large Angle Controller Block Diagram	56
Figure 53	ϕ and θ Errors for Static Commands using the Large Angle Controller with Modified PID Compensator.....	57
Figure 54	Comparison of the Large Angle Controller Static Errors between the PID and Modified PID Compensators.....	58
Figure 55	Large Angle Controller Transient Performance for Simultaneous $+1^\circ$ Rotations about the x and y-axes (PID vs. Mod-PID)	58
Figure 56	Large Angle Controller ϕ and θ Commanded and Actual Trajectories for Single Axis Rotations	59
Figure 57	Large Angle Controller ϕ and θ Errors for Single Axis Rotations	60
Figure 58	Large Angle Controller Nominal Circular Tracking Trajectory ($\pm 1^\circ$ at 0.1 Hz).....	61
Figure 59	Large Angle Controller ϕ and θ Errors for Nominal Circular Trajectory.....	62
Figure 60	Large Angle Controller ϕ and θ Errors Corresponding to 0.1 Hz Circular Trajectories for Various Radii	62

Figure 61	Large Angle Controller ϕ and θ Errors Corresponding to Clockwise, 1.0° Radius, Circular Trajectories for Various Tracking Speeds	63
Figure 62	Ambient Noise Power Spectral Density	67
Figure 63	Power Spectral Density of the System Response to a Single Tone (40 Hz) Disturbance	68
Figure 64	Pointing Error at the Nominal Payload Orientation with a Single Tone (40 Hz) Disturbance	69
Figure 65	Combined Vibration Suppression and Pointing Controller (Simplified).....	70
Figure 66	Adaptive Disturbance Canceller Baseline Performance	70
Figure 67	Power Spectral Density of the System Response to a Single Tone Disturbance (40 Hz) at an Orientation of $+1^\circ$ about the x-axis and -1° about the y-axis.	71
Figure 68	Pointing Error with a Single Tone Disturbance (40 Hz) at a Pose of $+1^\circ$ about the x-axis and -1° about the y-axis.....	72
Figure 69	Performance of ADC with a 0.1° Radius Circular Trajectory at 0.1 Hz	73
Figure 70	Performance of ADC with a 0.5° Radius Circular Trajectory at 0.1 Hz	73
Figure 71	Performance of ADC with a 1.0° Radius Circular Trajectory at 0.1 Hz	74
Figure 72	Performance of ADC with a 0.1° Radius Circular Trajectory at 2.0 Hz	75
Figure 73	Performance of ADC with a 0.5° Radius Circular Trajectory at 2.0 Hz	75
Figure 74	Performance of ADC with a 1.0° Radius Circular Trajectory at 2.0 Hz	76
Figure 75	Pointing Error for 0.1° Radius Circular Trajectory at a Speed 0.1 Hz	77
Figure 76	Pointing Error for 1.0° Radius Circular Trajectory at a Speed 0.1 Hz	77
Figure 77	Pointing Error for 0.1° Radius Circular Trajectory at a Speed 2.0 Hz	78
Figure 78	Pointing Error for 1.0° Radius Circular Trajectory at a Speed 2.0 Hz	79

THIS PAGE INTENTIONALLY LEFT BLANK

LIST OF TABLES

Table 1	PPH Geometry	9
Table 2	PPH Actuator Specifications.....	10
Table 3	Kaman KD-2300 (type 8C) Sensor Specifications	13
Table 4	Vertical Sensor Locations	14
Table 5	Accelerometer Specifications	15
Table 6	Bass Shaker Specifications	15
Table 7	Mathematical Nomenclature	20
Table 8	PPH Joint Locations.....	20
Table 9	Measurement Errors.....	33
Table 10	Ambient Noise Environment Baseline for Fixed Orientation and Dynamic Tracking Trajectories without Disturbance	67

THIS PAGE INTENTIONALLY LEFT BLANK

ACKNOWLEDGMENTS

The author would like to thank Professor Brij Agrawal for providing an environment conducive to academic learning and quality research. The office space was a rarity at NPS and not many people can say that they had an actual satellite in their office. Also to Dr. Hong-Jen Chen, for his meticulous attention to detail and insightful recommendations throughout this entire research process.

I'd also like to recognize the contributions of my family, without whose support this work would not have been completed. Andrew's (5) daily prayers for daddy to "not get frustrated with his paperwork" warmed my heart. Not many five year olds know how to say "hexapod", nonetheless know what one is. Abigail's (3) special trips to daddy's work for lollipops and using the "weigher" (scale) will never be forgotten. And for Amanda's (1) smiles, which praise God, just seem to put the whole world into the proper prospective.

Finally I like to thank my most trusted counsel and my best friend for her support and words of encouragement. Pamela you are a breed apart and I am truly blessed to have you by my side. Thank You just isn't enough to express my gratitude for keeping me "pointed" in the right direction.

THIS PAGE INTENTIONALLY LEFT BLANK

I. INTRODUCTION

A. MOTIVATION

Precision pointing and vibration isolation of spacecraft payloads is an area of great interest within the space industry. The current trend in spacecraft design is to build a lighter, less rigid spacecraft bus to minimize weight and save launch costs. The result is a spacecraft that more readily transmits noise and vibrations throughout the spacecraft. Noise sources on a typical spacecraft bus are generally the result of rotating machinery, either within the spacecraft bus or with the payload itself (e.g. a reaction wheel or a cryogenic cooler pump), but can extend themselves to other forms such as thermal “twang” from rapid thermal expansion or contraction, appendage movement, thruster induced vibrations, or external forces such as docking. In contrast, advances in imaging technology such as improved spatial and spectral resolution, higher bandwidths and smaller fields of regard have demanded a greater requirement for jitter control. Furthermore, these advances will mandate an increased tendency toward decoupling the imaging payload from the spacecraft attitude dynamics and control system in order to achieve the desired pointing accuracies required. One possible solution to this dichotomy between spacecraft bus and payload requirements is the use of a Stewart-Gough platform or hexapod; to both provide precision pointing and active vibration isolation and suppression to the payload.

Theoretical analysis and laboratory experimentation have shown great promise in the use of parallel manipulators such as the 6 degree of freedom (DOF) Stewart-Gough platform to simultaneously provide precision pointing while isolating the spacecraft bus noise from the payload (or suppressing a vibration source from within the payload itself). Vibration isolation and suppression techniques have proliferated the literature for quite some time and significant advances have been made. Recent works have included the classical Least Mean Squared (LMS) method [1], the clear box method [2,3,4], and most recently at the Spacecraft Research and Design Center (SRDC) at the Naval Postgraduate School (NPS), the Adaptive Disturbance Canceller (ADC) [5]. However, it has not been until the mid-to-late 1990’s that precision pointing and combined precision pointing and vibration isolation techniques using hexapods have emerged.

Most notable has been the Vibration Isolation, Suppression, and Steering System (VISS) [6,7,8] which was one of the first fielded hexapods that was designed to provide both pointing and active vibration isolation and suppression. This system provided the basis for which this research was to build upon.

B. OBJECTIVES

The primary focus of this research was to develop precision pointing controllers using the Precision Pointing Hexapod the Naval Postgraduate School. This research first developed a small angle controller using a decoupling matrix to control the actuator lengths for pointing control. A large angle controller was then developed using the vector loop equations of each actuator to control the payload platform orientation without the small angle approximations used in the small angle model. Once complete, the small angle controller was then combined with the Adaptive Disturbance Canceller, which was previously implemented at NPS, to demonstrate precision pointing with vibration suppression. This research was both analytical and experimental in nature, and supported the ongoing development of the bi-focal relay mirror project of the Spacecraft Research and Design Center (SRDC) at the Naval Postgraduate School.

C. HISTORICAL BACKGROUND

1. Precision Pointing

Since the early days of satellites, there has been a need to have some degree of pointing. The first pointing techniques were really more appropriately called attitude dynamics and controls, in which the spacecraft was oriented correctly with respect to the Earth and/or Sun. Some of the first techniques included spin-stabilized spacecraft like Explorer VI (circa 1958) [9] and then later included gravity gradient booms like the Applications Technology Satellite (ATS) program (circa 1966)[10]. Magnetic torque rods and reaction wheels were later fielded to do much the same thing; three-axis stabilized spacecraft, such as LANDSAT (circa 1970) soon followed [11]. Recently, control momentum gyroscopes (CMG) have been used to control the attitude of large spacecraft such as the International Space Station [12]. While highly accurate, development of such spacecraft was, and still is, costly. Such spacecraft also require the

spacecraft attitude dynamics and control system to be closely married to the payload subsystem. Some recent projects that have attempted to decouple the spacecraft attitude control system from the payload system for fine pointing have included such systems like the Middeck Active Control Experiment (MACE and MACE II) in 1995 [13]. These experiments used a dual-gimbal assembly to put the imaging payload in the desired orientation without strict reliance on the attitude control system of the host spacecraft. Recently in the late 1990's, the VISS program was launched which used a Stewart-Gough platform to provide both active vibration isolation and suppression as well as modest position pointing for a mid-wave infrared sensor [6].

2. Vibration Isolation and Suppression

In space applications, vibration sources are numerous such as:

- Launch Loading
- Man-induced accelerations like on the Shuttle or space station
- Solar Array drive assemblies
- Reaction wheels
- Control Momentum Gyroscopes
- Tape and disk drives
- Cryogenic cooler pumps [14]

Such sources can be found both within the spacecraft bus, and within the sensitive payload itself. Therein lies the basis for the distinction between vibration isolation and vibration suppression. Isolation refers to a technique that separates the dynamics of the spacecraft bus from that of the payload (e.g. a reaction wheel within the spacecraft bus). This is also known as the “quiet box” problem. Suppression, on the other hand, is a technique that must compensate for vibration within the payload (e.g., a cryogenic cooler) so that it does not affect the performance of the sensor on the payload. This is known as the “dirty box” problem [15]. In general, vibration isolation requires a relatively soft stiffness mount (e.g. an air bearing) to absorb the energy, while vibration suppression requires a relatively hard stiffness mount to transmit vibrations throughout the spacecraft structure.

The first generation vibration isolation and suppression techniques were mostly passive in nature such as springs or tuned mass dampers (TMD), which isolated the noise source from the rest of the spacecraft. Furthermore, the spacecraft structure was fairly rigid; to both endure the launch loads, and minimize vibration dynamics. Second generation techniques were again mostly passive, using magnetic bearings and attempting to manufacture quieter subsystems. Third generation techniques have now included active vibration isolation and suppression especially at lower frequencies where passive isolation is ineffective. Without a doubt, future systems will make use of active vibration isolation and suppression especially as spectral and spatial resolution technology improves and spacecraft bus structures become more flexible.

3. Stewart-Gough Platform

a. History

The Stewart-Gough platform is a six-legged parallel manipulator. In other words, six actuators join the base platform to the payload platform as illustrated in Figure 1. First used in 1949 by Gough as a universal tire-testing machine [16], this manipulator was re-discovered in 1965 by D. Stewart for use in aircraft simulators [17]. The platform is generally called a Stewart Platform, however in deference to both inventors, some texts have chosen to refer to them as Stewart-Gough Platforms [18], as this thesis will do. While the Stewart-Gough platform has been in use for decades, it was not until the 1980's that serious analytical work was devoted to solving the kinematics of the Stewart-Gough Platform.

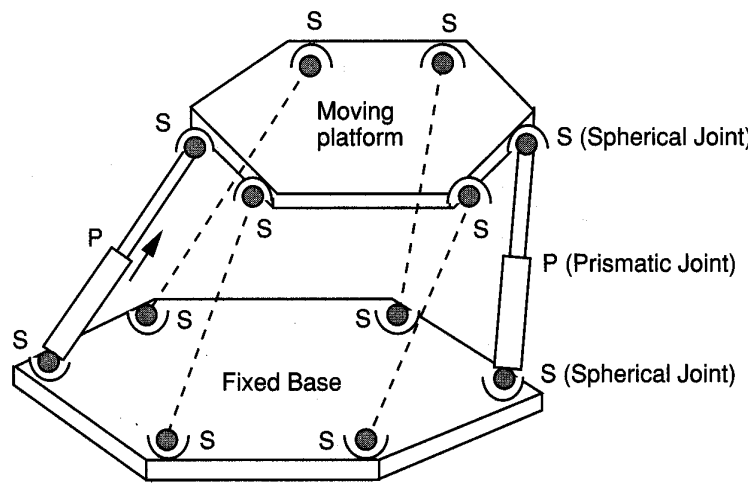


Figure 1 Nominal Stewart-Gough Platform (from [18])

b. Kinematic Developments

The static force analysis of the Stewart-Gough Platform is shown in Merlet [19] and is presented in Chapter III of this thesis. Fichter extended this analysis and incorporated the gravity and dynamic forces on the platform and formulated the inverse dynamics with massless legs and frictionless joints [20]. Do and Yang solved the inverse dynamics problem by the Newton-Euler method assuming frictionless joints and symmetrical and thin legs [21]. Geng et al developed the Lagrangian equations of motion with the platform position and orientation variables as generalized coordinates [22] in 1992. Liu et al did much the same in 1993 but in joint space [23]. Ji considered leg inertia and studied its effect on platform dynamics also in 1993 [24]. Dasgupta and Mruthyunjaya in 1998 formulated the inverse dynamics using the Newton-Euler approach but eliminated unwanted force components to form a system of six linear equations with six unknowns to obtain the required leg input forces directly [25]. In 2000, Pernechele et al developed a neural network algorithm for controlling a Stewart-Gough Platform [26].

c. Recent Vibration Isolation and Precision Pointing Applications

Two recent military space applications have used Stewart-Gough platforms for active vibration isolation and suppression. The first one, mentioned earlier is called VISS [12]. This system had the capability to provide both active vibration isolation and suppression and course steering instructions to a mid-wave infrared (MWIR) payload through the Stewart-Gough Platform. On orbit, VISS demonstrated the desired steering accuracy and passive vibration isolation, but the active vibration isolation and suppression suffered an irresolvable noise issue when powered (noticeable mainly because the passive isolation did so well), limiting the amount of active vibration isolation and suppression that could be accomplished. As a result, combined isolation, suppression, and steering operations were not extensively conducted [27]. More recently, an experiment launched by the Air Force Research Laboratory (AFRL) called the Satellite Ultraquiet Isolation Technology Experiment (SUITE) on PicoSAT, is currently on-orbit and is used as a test bed for emerging vibration isolation control algorithms [28]. To date, most of the work by the guest investigators on SUITE has

been system identification work with several controller experiments to be evaluated in the upcoming year. SUITE has no organic pointing capability and was designed solely as a vibration isolation experiment.

Recent analytical work published in the area of precision pointing has mostly come out of the University of Wyoming by John McInroy and collaborators. Much of his earlier work focused on fault-tolerant approaches to precision pointing that were reconfigurable in the event of an actuator failure. [29,30]. Figure 2 illustrates the approach. The reconfiguration algorithm was straightforward in that only the failed actuators had to be determined, and then through a look-up table the resulting decoupling matrix, calculated a priori, could be applied. More recent work out of the University of Wyoming has been in improving precision pointing through the modeling of flexure joint dynamics [31,32], and sinusoidal disturbance cancellation [33] while using Stewart-Gough platforms.

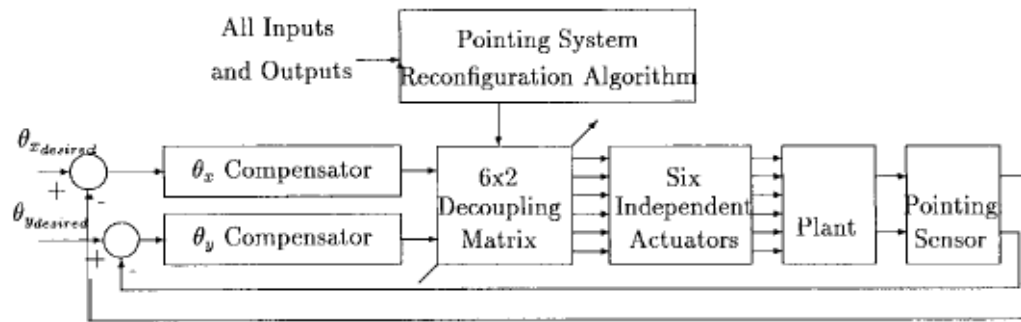


Figure 2 Fault-Tolerant Decoupled Pointing Approach

II. HARDWARE DESCRIPTION

A. OVERVIEW

The experimental setup is shown in Figure 3. At the center of the setup is the Precision Pointing Hexapod with accelerometers located on each actuator and distance measuring sensors on the payload platform. The control signals to the actuators came from the Host Computer through a PowerPC dedicated controller and into a power amplifier before going to the actuators. Accelerometer and positioning sensor power was regulated through a control box that provided the proper AC-DC conversion. The outputs from these sensors were routed through the control box, which converted the outputs to the proper connector type, and were then sent to the PowerPC controller and processed in the host computer.

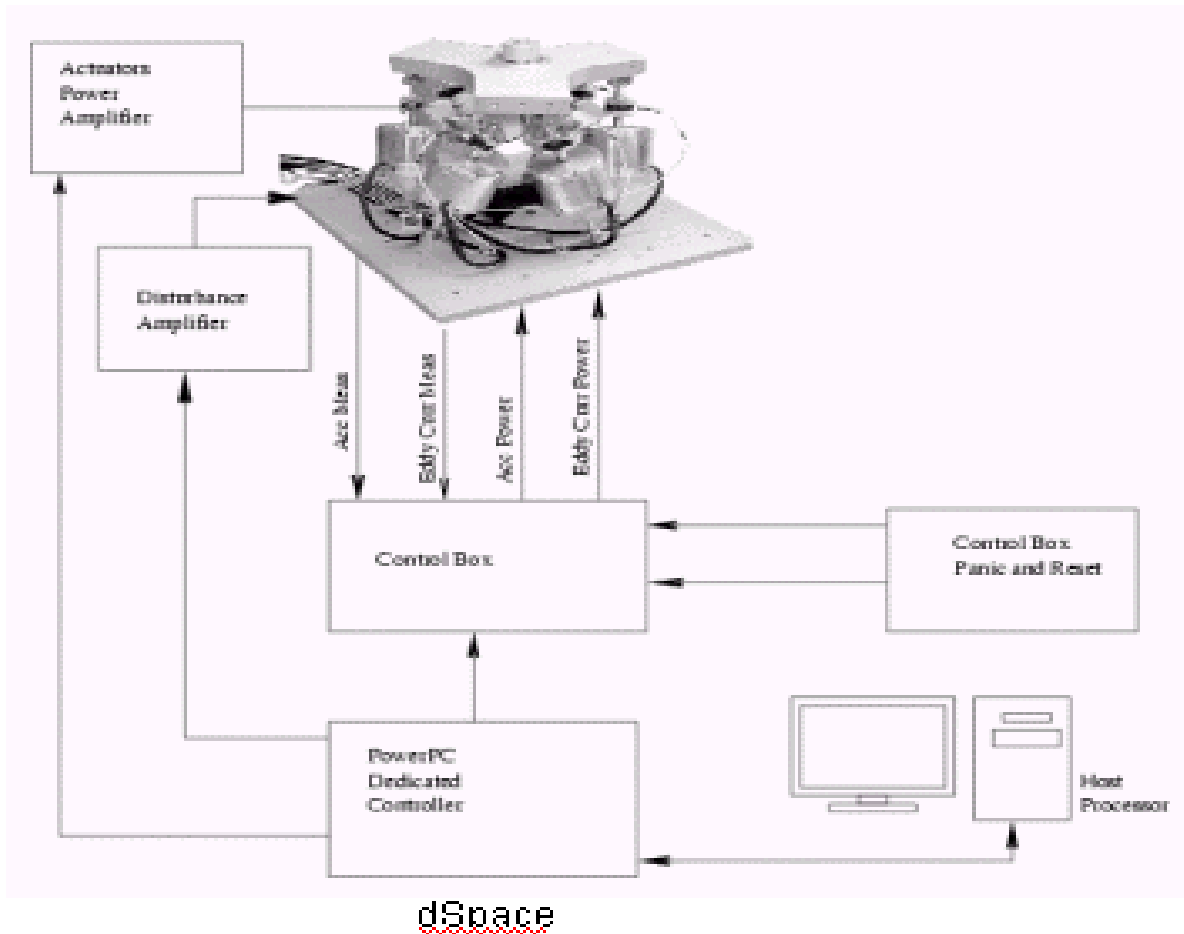


Figure 3 Precision Pointing Hexapod Experiment Setup

B. PRECISION POINTING HEXAPOD

Uniquely designed and constructed by CSA Engineering, Inc, the Precision Pointing Hexapod shown in Figure 4 was designed as a 6-DOF manipulator. It was designed to provide over ± 5.5 mm of axial travel, ± 20 mm of XY shear (translation), more than $\pm 2.5^\circ$ of tip/tilt and up to $\pm 10^\circ$ of twist. Figure 5 illustrates the various modes

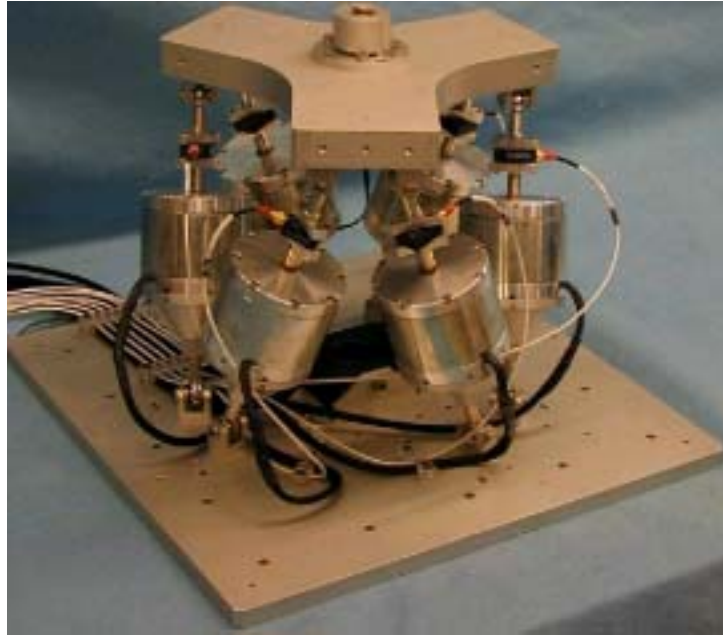


Figure 4 Precision Pointing Hexapod

and Table 1 describes the geometry. It was capable of being outfitted with a variety of sensors depending on the specific application, such as for investigating vibration isolation, vibration suppression, and position pointing/tracking control algorithms [34].

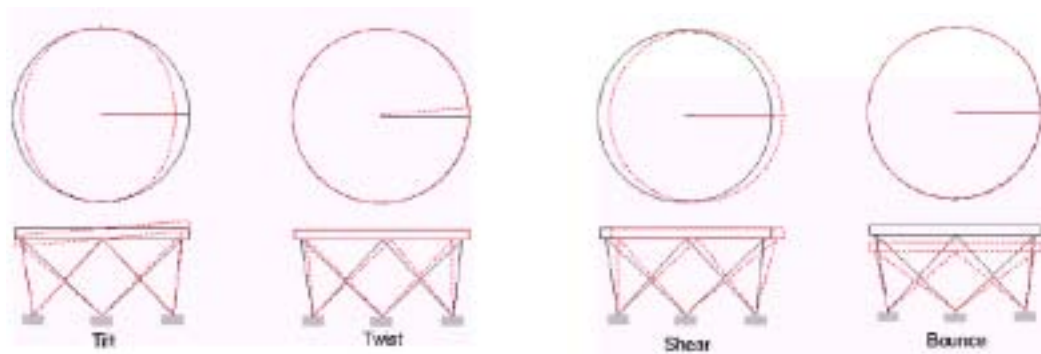


Figure 5 Hexapod Modes

Table 1 PPH Geometry

Parameter	Value
Upper Radius of payload platform ¹	0.1143 m
Lower Radius of base mounts	0.1588 m
Upper Angle ²	25°
Lower Angle	25°
Separation Height ³	
Absolute Minimum	0.2513 m
Minimum at -4 V	0.2527 m
Nominal at 0 V	0.2565 m
Midstroke ⁴	0.2584 m
Maximum at 4 V	0.2642 m
Absolute Maximum	0.2654 m
Mass of platform, including movable actuator links	2.849 kg
Moment of inertia of platform	$\begin{bmatrix} 0.0277 & 0.0 & 0.0 \\ 0.0 & 0.0277 & 0.0 \\ 0.0 & 0.0 & 0.0533 \end{bmatrix} \text{kg-m}^2$

Notes

- ¹ Radius is measured from center of platform (payload or base) to the joint attachment on that platform
- ² Angle measurement is between actuators measured at the joint attachment
- ³ Measured from top of bottom plate to bottom of top payload plate
- ⁴ The 1.9 mm difference between nominal and midstroke parameters is due to gravity loading from the payload platform on to the actuators.

1. Actuator Strut Assembly

The actuator strut was a Motran AXF-70 self-supporting electromagnetic voice coil actuator and is illustrated in Figure 5. Each actuator was connected to the base plate and payload platform using metal flexure joints and had an in-line bracket for accelerometer mounting. Power was supplied to the actuator through a five-foot cable with a three-pin male switchcraft audio connector. Actuator specifics are shown in Table 2.

Table 2 PPH Actuator Specifications

Parameter	Value
Size	0.0790 m diameter, 0.06985 m tall
Total Mass	1250 grams
Moving Mass	440 grams
Operating Range	± 10 V, ± 4 amps, 0-40 W
Linear output range	± 5 mm
DC Holding Force	70 N at 40 W DC
Resonance Force	100 N at 40 W _{rms} sine
Internal Resonance	11 Hz
Effective mechanical stiffness	2200 N/m
Resistance	2.5 Ohm (across pins 1 & 2)
Time Constant	1 millisecond



Figure 6 PPH Strut Actuator

The actuators were powered by a custom power supply composed of six independent switching inverting amplifiers (29 kHz switching frequency) and are shown in Figure 7. The amplifier had a negative gain (-1) and accepted a voltage range of ± 4 V

through coaxial cables. The output of the amplifier was directly connected to the actuators.



Figure 7 PPH Power Supply

2. Position Sensing Device (PSD)

The position sensing device (PSD) was designed as an independent sensor used to evaluate pointing algorithms by providing a direct measurement of displacement in two degrees of freedom along the X-Y plane of the base plate. The PSD could be used to evaluate the motion of the payload plate with respect to the base plate. This motion included shear motion in the X-Y plane and tip/tilt motion of the payload platform about the x and y-axis, but not simultaneously. The PSD consisted of three components shown in Figure 8: the Compact Laser Diode Module (not shown), the position-sensing module, and the position-sensing amplifier.

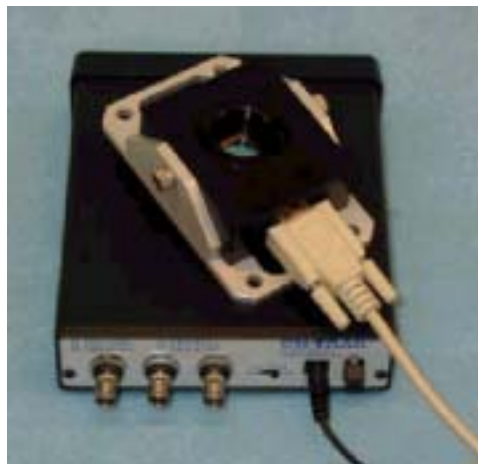


Figure 8 Position Sensing Module and Amplifier

a. Compact Laser Diode Module

The LDM145 Compact Laser Diode Module was a class II laser manufactured by Imatronic. It had an output power of 0.9mW at 670nm wavelength. The beam size aperture was 5 mm and the beam size at the nearest focus was 100 μ m. The module operated at 4-6 V with a current drain of 60 milliamps. It was 49 mm long with a diameter of 16mm and weighed less than 20 gm. The module had two mounts which allowed mounting in either the vertical (z-axis) or horizontal (x or y-axis) at the center of the payload platform.

b. Position Sensing Module (PSM)

The PSM (model 2-10) position-sensing module was a fully packaged silicon position sensing photodiode that provided an analog output directly proportional to the position of a light spot on the detector area. Made by On-Trak Photonics, Inc., the PSM had a 10x10 mm active area with a position non-linearity of less than 0.8% (typical non-linearity was 0.3%). The PSM was mounted at the center of the base plate and had a DB9 subminiature 9-pin connector which connected directly to the OT-301 Position Sensing Amplifier. The direction of the cable mount represented the +x-direction.

c. Position Sensing Amplifier

The OT-301 position-sensing amplifier was made by On-Trak Photonics and was designed to provide an X-Y position output and sum output from the PSM through BNC connectors. The amplifier required 12V DC and 500mA, which was provided by an AC Adapter. The output voltage range was ± 10 v and had a frequency response from DC to 16 kHz.

3. Kaman Eddy Current Sensors

The Kaman Instrumentation's Multi-Purpose Variable Impedance transducer measuring system, the KD-2300, was a non-contact linear proximity measuring system (Figure 9) . This system used six Kaman type 8C sensors and was designed for sensing the orientation of the payload platform with respect to metallic targets fixed on the base plate as shown in Figure 10. The six sensors were arranged on the payload platform as shown in Figure 11. The locations of the three vertical sensors from the centroid of the payload plate are given in Table 4. Each sensor was powered by a Kaman 6-channel,

± 15 V DC power source. The sensor output was routed through a noise filter before going into the controller and the host computer. The sensors were calibrated using Plexiglas spacers of known thickness (2.244 mm) to align the sensor spacing to the target and to adjust the linearity of the KD-2300. Sensor specifications are shown in Table 3.

Table 3 Kaman KD-2300 (type 8C) Sensor Specifications

Parameter	Value
Target Material	Non-magnetic and metallic
Measuring Range	12.7 mm
Offset	1.25 mm
Nonlinearity	± 0.127 mm
Mid-range Static Resolution	$1.3\mu\text{m}$
Output Range	0-1.270 V
Frequency Response	DC to 50 kHz

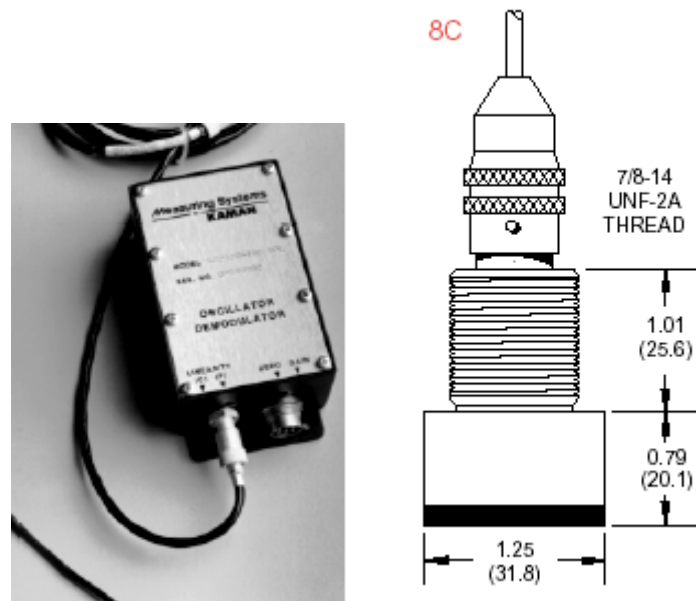


Figure 9 The KD-2300 Measuring System with Sensor

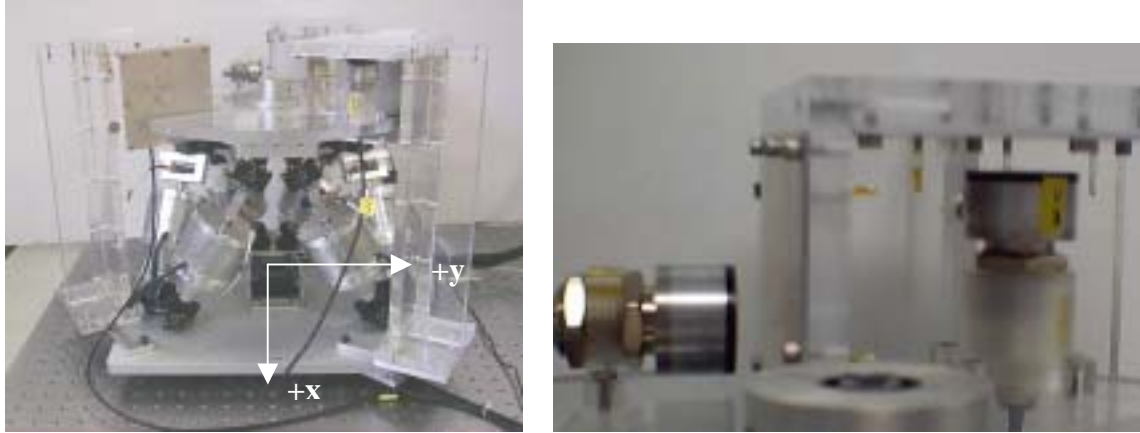


Figure 10 The KD-2300 Target Configuration

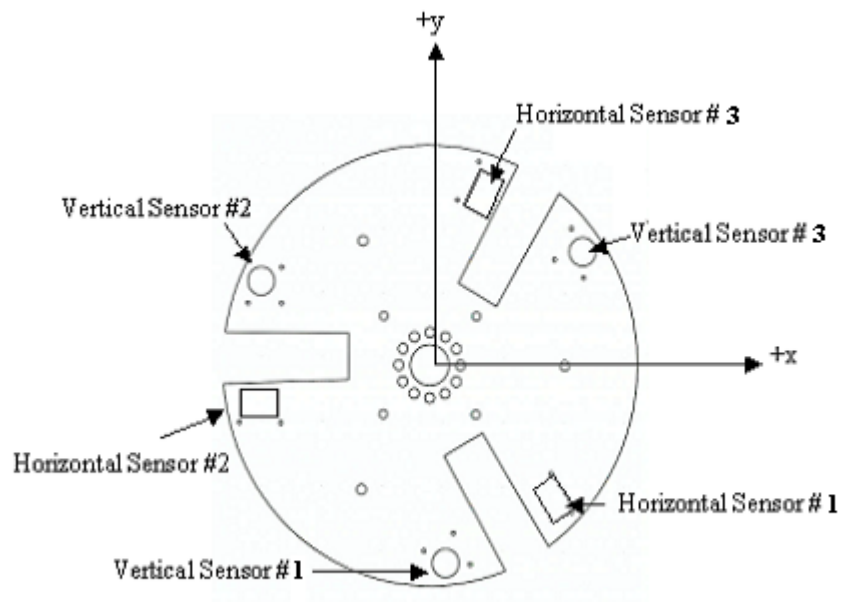


Figure 11 The KD-2300 Sensor layout top view

Table 4 Vertical Sensor Locations

Sensor	x-distance (mm)	y-distance (mm)
Vertical #1	14.12	-153.51
Vertical #2	-140.00	64.53
Vertical #3	125.88	88.98

4. Accelerometers

Each actuator was equipped with a Kistler 8304B2 K-Beam accelerometer mounted in-line with the strut axis as shown in Figure 6. The specifications for the accelerometers, shown in Figure 12 are given in Table 5.



Figure 12 PPH Accelerometers

Table 5 Accelerometer Specifications

Parameter	Value
Range	± 2 g
Sensitivity	1000 mV/g
Frequency response $\pm 5\%$	0-300 Hz
Linear Range	0-200 Hz
Resolution	0.1 mg _{rms}

5. Disturbance Generator

The disturbance generator consisted of an Aura Bass shaker AST-2B-4 mounted on a custom adapter, shown in Figure 13, and a 2-channel Pioneer SA-950 Stereo Amplifier. The Aura Bass Shaker was connected to the output of the stereo amplifier, which was connected directly to the controller and host computer. The bass shaker specifications are shown in Table 6.

Table 6 Bass Shaker Specifications

Parameter	Value
Magnet type	Ceramic
Power rating	50 W
Nominal Force at resonance	132 N
Weight	1.125 kg
Resonance frequency	42 Hz
Frequency Range	20-100 Hz



Figure 13 Aura Bass Shaker and Custom Adapter

6. Floating Table and Environment Isolation

The entire experimental setup was mounted on a Newport Stabilizer laminar flow isolator table to prevent the seismic and building vibrations from interfering with the experiment. Additionally, the precision pointing hexapod was installed on the table using very soft rubber pads to passively dampen any remaining high frequency vibrations. The rubber pads wore out over time and were replaced before each experiment to ensure continuity in experimental results.

7. Electronic Support

The experiment was supported by two custom made electronic packages: The control box and the anti-aliasing and noise suppression filter. The control box was the primary interface between the sensors (accelerometers and Kaman position sensors) and the rest of the experiment. The control box provided both $\pm 5V$ and $\pm 12V$ electrical power to the sensors through a standard DB25 connector. The control box also received the output signals from the sensors, converted it to the proper connector type, and sent them to the anti-aliasing and noise suppression filters.

The control box also had shock detection, emergency shutdown, and manual reset features to protect the system should any instability arise. This was accomplished by sampling the signal from the accelerometer mounted on actuator #1 and sending it to a window comparator. Should the accelerometer output voltage be smaller than 0.5 V or greater than 4.5V, indicating that the dynamic range of the accelerometer (± 2 g) had been exceeded, an interrupt signal would be sent disconnecting the actuators and

disturbance amplifiers from the 110V rail power. Power was restored to the actuators and disturbance amplifiers by manually depressing the reset button at the operator's station. Additionally, a panic button was also at the operator's station that allowed the operator to manually disconnect power to the actuators and disturbance generator.

The anti-aliasing and noise suppression filters were fourth order switched capacitor Butterworth filters. The corner frequency was adjustable by changing the oscillator frequency with a potentiometer. The corner frequency was defined as $f_c = f_{osc}/50$. The filter was actually a digital filter implemented with analog components, and therefore the operator had to ensure that no frequencies above $f_c/2$ were being sampled when selecting f_{osc} to satisfy the Nyquist sampling theorem. From the anti-aliasing and noise suppression filters, the signal was then sent to the controller and host computer.

8. Controller and Host Computer

The experiment controller was a dedicated PowerPC-based board, the dSPACE DS1103, which was installed inside the host PC. A connection panel was attached to the board shown in Figure 14 and provided all external communication to the controller as shown in Figure 3.

The host computer was a PC Dell Dimension XPS T500. The controller board was accessed and controlled by using dSPACE ControlDesk and the Real Time Workshop by MathWorks. All filtering, disturbance generation, and I/O were implemented using Simulink block diagrams and converted to C using the Real Time Workshop. All data logging was performed by ControlDesk, which allowed the desired output variables to be streamed to disk in a *.IDF or *.MAT format for data reduction and analysis.



Figure 14 dSPACE Connection Panel

THIS PAGE INTENTIONALLY LEFT BLANK

III. MATHEMATICAL ANALYSIS

A. COORDINATE SYSTEM

Figure 15 illustrates the coordinate systems used in the analysis of the Stewart-Gough platform and how it applies to the PPH. The nomenclature used in the mathematical analysis is summarized in Table 7. The X-Y-Z coordinate frame is fixed to the stationary base at point O, the center of the base plate. The u-v-w coordinate frame was attached to the payload platform at the center point P and moved with the payload platform. In the nominal position, the X-Y-Z fixed base coordinate system was co-aligned with the moveable u-v-w coordinate frame but was offset by the vector \mathbf{p} , whose magnitude was the separation distance between the payload platform and the base plate, and whose direction was along the +Z-axis. The base plate joints are represented by A_i and the payload platform joints by B_i where $i = 1$ to 6, depending on the actuator that attaches the joints. Table 8 lists the actual joint measurements from the PPH. On the PPH, actuator #1 is located in the first quadrant of the base coordinate system and the remaining actuators are numbered counter-clockwise. The vector aligned with each actuator, \mathbf{d}_i had a magnitude equal to the length of that actuator. The vector \mathbf{a}_i was from the fixed origin O to the corresponding A_i joint. The vector ${}^B\mathbf{b}_i$ was from the moving platform origin P to the B_i joint in the payload frame, u-v-w (\mathbf{b}_i in fixed X-Y-Z frame).

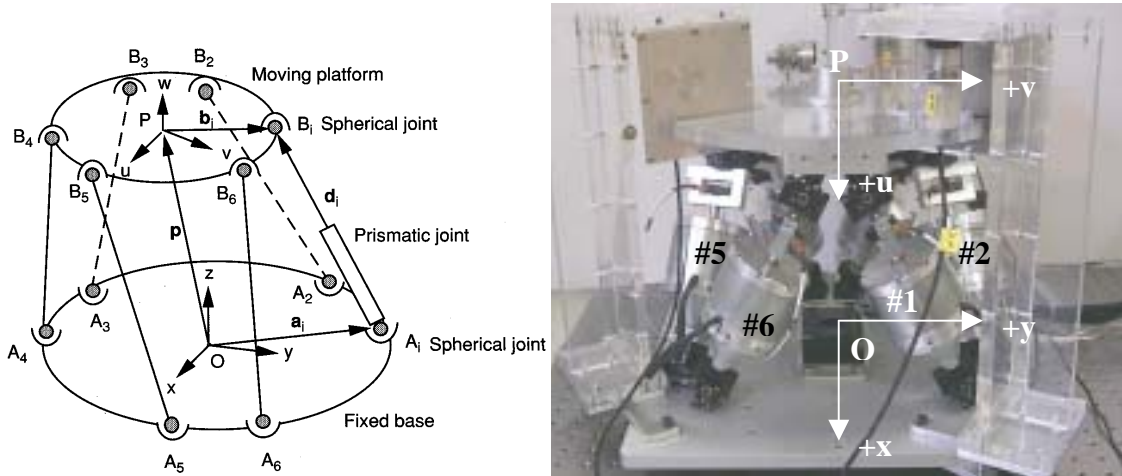


Figure 15 Stewart-Gough Platform Coordinate Frames (from [18])

Table 7 Mathematical Nomenclature

Symbol	Parameter
P	Vector from base origin to payload origin
a_i	Vector from point O to the base actuator joint A_i
$b_i, {}^B b_i$	Vector from point P to the payload platform actuator joint B_i . ${}^B b_i$ denotes the moving payload coordinate system (u-v-w).
e_{iv}	Vector from point P to the i th vertical (v) or horizontal (h) sensor. See Table 4.
ΔZ_i	Vertical displacement along Z-axis of the i th vertical sensor
d_i	Scalar length of the i th actuator
$A_i B_i, d_i$	Vector of the i th actuator (from joint A_i to joint B_i)
s_i	Unit vector direction of the i th actuator
ω_i, ω_b	Angular rate of the payload platform in inertial frame and body frame
v_p	Translational velocity vector of payload platform
ψ	Payload rotation about Z-axis
θ	Payload rotation about the v' axis
ϕ	Payload rotation about the u'' axis
$[{}^A R_B]$	Direction cosine matrix for payload with respect to the fixed (X-Y-Z) frame
\dot{x}	6 x 1 vector of translational and rotational velocities
\dot{q}	6 x 1 vector of the change in actuator lengths $\dot{q} = [\dot{d}_1, \dot{d}_2, \dots, \dot{d}_6]^T$
$[J]$	Jacobian matrix
O	Origin point of fixed base plate and X-Y-Z coordinate frame
P	Origin point of moving payload platform and u-v-w coordinate frame
M	Moments about point P
f, f_i, f_i	Total force vector or force vector along i th actuator. Scalar quantity is the force magnitude along i th actuator

Table 8 PPH Joint Locations

Joints	Location in mm $[x, y, z]^T$
Base plate (Measured from Point O in the fixed X-Y-Z frame)	$a_1 = [+96.61, +125.88, 0]^T$ $a_2 = [+60.71, +146.61, 0]^T$ $a_3 = [-157.31, +20.73, 0]^T$ $a_4 = [-157.31, -20.73, 0]^T$ $a_5 = [+60.71, -146.61, 0]^T$ $a_6 = [+96.61, -125.88, 0]^T$
Payload Plate (Measured from Point P in the moving u-v-w frame)	$b_1 = [+112.95, +15.60, 0]^T$ $b_2 = [-42.95, +105.61, 0]^T$ $b_3 = [-70.00, +90.02, 0]^T$ $b_4 = [-70.00, -90.02, 0]^T$ $b_5 = [-42.95, -105.61, 0]^T$ $b_6 = [+112.95, -15.60, 0]^T$

Using a 3-2-1 Euler angle transformation, where ψ was a rotation about the Z-axis, followed by a θ rotation about the rotated v-axis designated v', and then a ϕ rotation about the new u-axis designated u''. The combined rotation matrix, ${}^A\mathbf{R}_B$ is shown in (1).

$${}^A\mathbf{R}_B = \begin{bmatrix} \cos\theta\cos\psi & \cos\theta\sin\psi & -\sin\theta \\ \sin\phi\sin\theta\cos\psi - \cos\phi\sin\psi & \sin\phi\sin\theta\sin\psi + \cos\phi\cos\psi & \sin\phi\cos\theta \\ \cos\phi\sin\theta\cos\psi + \sin\phi\sin\psi & \cos\phi\sin\theta\sin\psi - \sin\phi\cos\psi & \cos\phi\cos\theta \end{bmatrix} \quad (1)$$

B. POSITION ANALYSIS OF STEWART-GOUGH PLATFORM

A vector-loop equation of the i th actuator can be written as (2):

$$\mathbf{A}_i\mathbf{B}_i = \mathbf{d}_i = \mathbf{p} + [{}^A\mathbf{R}_B]^B\mathbf{b}_i - \mathbf{a}_i, \forall i = 1 \dots 6 \quad (2)$$

The length of the i th actuator is then obtained by a dot product of $\mathbf{A}_i\mathbf{B}_i$ with itself:

$$d_i = \pm \sqrt{[\mathbf{p} + [{}^A\mathbf{R}_B]^B\mathbf{b}_i - \mathbf{a}_i]^T [\mathbf{p} + [{}^A\mathbf{R}_B]^B\mathbf{b}_i - \mathbf{a}_i]}, \forall i = 1 \dots 6 \quad (3)$$

or

$$d_i = \pm \sqrt{\mathbf{p}^T\mathbf{p} + {}^B\mathbf{b}_i^T {}^B\mathbf{b}_i + \mathbf{a}_i^T\mathbf{a}_i + 2\mathbf{p}^T [{}^A\mathbf{R}_B]^B\mathbf{b}_i - 2\mathbf{p}^T\mathbf{a}_i - 2[[{}^A\mathbf{R}_B]^B\mathbf{b}_i]^T\mathbf{a}_i} \quad (4)$$

$$\forall i = 1 \dots 6$$

and then finally compactly:

$$d_i = |\mathbf{p} + \mathbf{b}_i - \mathbf{a}_i|, \forall i = 1 \dots 6 \quad (5)$$

C. ANGULAR VELOCITY AND ACCELERATION ANALYSIS OF A STEWART-GOUGH PLATFORM

Given the 3-2-1 Euler angle transformation and the combined rotation matrix in (1), the angular velocity of the moving payload platform $\boldsymbol{\omega}_p$, written in terms of the Euler angles and the body fixed, non-orthogonal coordinate system w- v'- u'' described above, becomes:

$$\omega_p = \dot{\psi}w + \dot{\theta}v' + \dot{\phi}u'' \quad (6)$$

Expressing this in the fixed base plate reference frame X-Y-Z, the equation becomes:

$$\omega_p = \begin{bmatrix} -\dot{\psi} \sin \theta + \dot{\phi} \\ \dot{\psi} \cos \theta \sin \phi + \dot{\theta} \cos \phi \\ \dot{\psi} \cos \theta \cos \phi - \dot{\theta} \sin \phi \end{bmatrix} \quad (7)$$

Taking the derivative of (7), the equation for acceleration becomes:

$$\dot{\omega}_p = \begin{bmatrix} -\ddot{\psi} \sin \theta - \dot{\psi} \dot{\theta} \cos \theta + \ddot{\phi} \\ \ddot{\psi} \cos \theta \sin \phi - \dot{\psi} \dot{\theta} \sin \theta \sin \phi + \dot{\psi} \dot{\phi} \cos \theta \cos \phi + \ddot{\theta} \cos \phi - \dot{\theta} \dot{\phi} \sin \phi \\ \ddot{\psi} \cos \theta \cos \phi - \dot{\psi} \dot{\theta} \sin \theta \cos \phi - \dot{\psi} \dot{\phi} \cos \theta \sin \phi - \ddot{\theta} \sin \phi - \dot{\theta} \dot{\phi} \cos \phi \end{bmatrix} \quad (8)$$

D. JACOBIAN OF A STEWART-GOUGH PLATFORM

The Jacobian matrix [J] transforms the velocity states of the end-effector or payload platform into joint rates in actuator space. The desired output in actuator space is the change in the actuator lengths given by $\dot{\mathbf{q}} = [\dot{d}_1, \dot{d}_2, \dots, \dot{d}_6]^T$, while the required input is described by the linear and angular velocity of the payload platform centroid:

$$\dot{\mathbf{x}} = \begin{bmatrix} v_p \\ \omega_B \end{bmatrix} \quad (9)$$

Thus the equation to solve is:

$$\dot{\mathbf{q}} = [\mathbf{J}] \dot{\mathbf{x}} \quad (10)$$

To find [J], rearrange (2) such that:

$$\mathbf{p} + [{}^A R_B]^B \mathbf{b}_i = \mathbf{a}_i + \mathbf{A}_i \mathbf{B}_i, \forall i = 1 \dots 6 \quad (11)$$

and differentiate with respect to time:

$$\mathbf{v}_p + \omega_B \times \mathbf{b}_i = \dot{d}_i \omega_i \times \mathbf{s}_i + \dot{d}_i \mathbf{s}_i, \forall i = 1 \dots 6 \quad (12)$$

Where \mathbf{s}_i is the unit vector along the actuator vector, and \mathbf{d}_i and $\boldsymbol{\omega}_i$ are the angular velocity with respect to the fixed base plate frame of the i th actuator. Next eliminate $\boldsymbol{\omega}_i$ by taking the dot product of both sides of (12) with \mathbf{s}_i to yield:

$$\mathbf{s}_i^T \mathbf{v}_p + (\mathbf{b}_i \times \mathbf{s}_i)^T \boldsymbol{\omega}_B = \dot{d}_i, \forall i = 1 \dots 6 \quad (13)$$

With some manipulation it can be shown that equations (10) and (13) are indeed equivalent with:

$$[J] = \begin{bmatrix} \mathbf{s}_1^T & (\mathbf{b}_1 \times \mathbf{s}_1)^T \\ \mathbf{s}_2^T & (\mathbf{b}_2 \times \mathbf{s}_2)^T \\ \vdots & \vdots \\ \mathbf{s}_6^T & (\mathbf{b}_6 \times \mathbf{s}_6)^T \end{bmatrix} \quad (14)$$

E. STATIC FORCE ANALYSIS

Next lets find the actuator forces f_1, f_2, \dots, f_6 required to produce an output force \mathbf{f} and an output moment \mathbf{m} at the centroid of the payload platform, point P. First lets assume the gravitational forces are negligible, actuator forces act axially along the actuator, and there is no moment transmitted to the actuators due to the joint geometry. Therefore the force acting on the moving platform by each actuator is:

$$\sum_{i=1}^6 f_i \mathbf{s}_i = \sum_{i=1}^6 \mathbf{f}_i = \mathbf{f} \quad (15)$$

and the moments contributed by all the forces about the moving centroid P:

$$\sum_{i=1}^6 f_i \mathbf{b}_i \times \mathbf{s}_i = \mathbf{m} \quad (16)$$

Combining (11) and (12) into matrix form:

$$\begin{bmatrix} \mathbf{f} \\ \mathbf{m} \end{bmatrix} = \begin{bmatrix} \mathbf{s}_1 & \mathbf{s}_2 & \cdots & \mathbf{s}_6 \\ \mathbf{b}_1 \times \mathbf{s}_1 & \mathbf{b}_2 \times \mathbf{s}_2 & \cdots & \mathbf{b}_6 \times \mathbf{s}_6 \end{bmatrix} \begin{bmatrix} f_1 \\ f_2 \\ \vdots \\ f_6 \end{bmatrix} \quad (17)$$

F. PAYLOAD VERTICAL SENSOR CONFIGURATION ANALYSIS

Given the configuration of the sensors shown in Figure 11 and the locations of the vertical sensors described by e_{1v} , e_{2v} , and e_{3v} (magnitude only), the vertical displacement sensed by a given sensor (ΔZ_1 , ΔZ_2 , ΔZ_3) for a rotation of the payload plate about the u-axis (ϕ) or the v-axis (θ) is described by the following sets of equations:

$$\Delta Z_1 = -e_{1v_y} \sin \phi - e_{1v_x} \sin \theta \quad (18)$$

$$\Delta Z_2 = e_{2v_y} \sin \phi + e_{2v_x} \sin \theta \quad (19)$$

$$\Delta Z_3 = e_{3v_y} \sin \phi - e_{3v_x} \sin \theta \quad (20)$$

Invoking the small angle approximation, combining displacement terms, and assuming a positive displacement is in the direction of the +Z-axis, the equations become:

$$\begin{aligned} \Delta Z_1 &= -\phi e_{1v_y} - \theta e_{1v_x} \\ \Delta Z_2 &= \phi e_{2v_y} + \theta e_{2v_x} \\ \Delta Z_3 &= \phi e_{3v_y} - \theta e_{3v_x} \end{aligned} \quad (21)$$

Rearranging terms and subtracting the first equation of (21) from the third, then solving for ϕ yields:

$$\phi = \frac{\Delta Z_3 e_{1v_x} - \Delta Z_1 e_{3v_x}}{e_{1v_y} e_{3v_x} + e_{3v_y} e_{1v_x}} \quad (22)$$

θ can now be found by replacing either the first or second equation of (21) with (22). To make use of the third sensor, the second equation of (21) was used and the equation for θ becomes:

$$\theta = \frac{\Delta Z_2 - \phi e_{2v_y}}{e_{2v_x}} = \frac{1}{e_{2v_x}} \left[\Delta Z_2 - e_{2v_y} \left(\frac{\Delta Z_3 e_{1v_x} - \Delta Z_1 e_{3v_x}}{e_{1v_y} e_{3v_x} + e_{3v_y} e_{1v_x}} \right) \right] \quad (23)$$

While any combination of the three equations of (21) will result in a valid description of ϕ and θ , the above derivation was chosen to minimize the effect of the small value of e_{1vx} on the results.

G. ADAPTIVE DISTURBANCE CANCELLER ANALYSIS

The Adaptive Disturbance Canceller (ADC) for the PPH was implemented at the Naval Postgraduate School by Christian Taranti. A complete description of the ADC can be found in [5]; only a brief description from that reference follows. The ADC was developed following the approach proposed in 1998 by Bertran and Mortoro [35]. This approach stated that assuming that the plant was linear and stable, it is possible to generate an arbitrary sinusoidal at the output of the system to cancel any sinusoidal disturbance. Such a canceller would require: a stable linear single input single output (SISO) plant, knowledge of the frequency of the disturbance, and a plant not having any zeros at the frequencies of interest. Figure 16 is a block diagram illustrating this control approach.

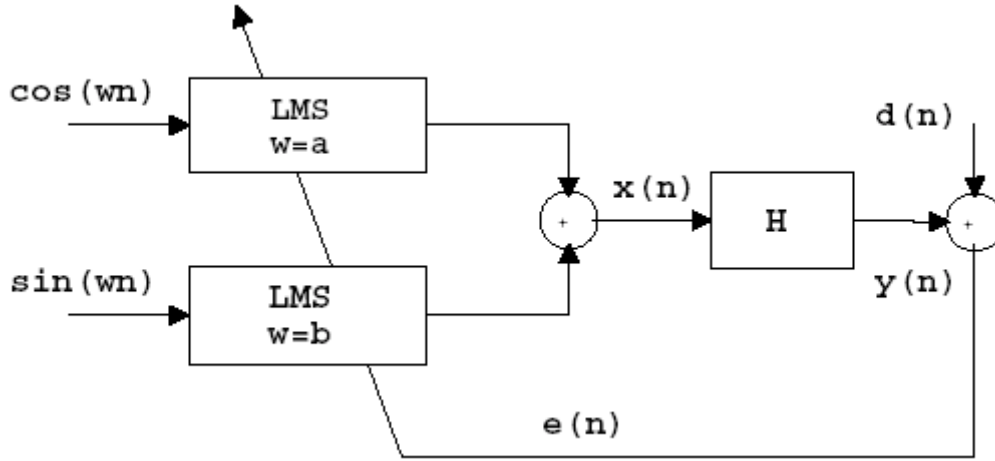


Figure 16 Adaptive Disturbance Canceller

Referring to Figure 16, assuming the plant H is linear, then for any sinusoidal signal $d[n]$ with frequency ω_c it is possible to find a sinusoidal input $x[n]$ such that $y[n] = -d_n$ (if $H(e^{j\omega_c}) \neq 0$). This input can be written as:

$$x[n] = X \cos(\omega_c n + \beta_x) \quad (24)$$

There exists several algorithms for finding the optimal value of $x[n]$ to minimize the error, $e[n]=y[n] + d[n]$, assuming $y[n]$ is linear. Using this assumption, (24) can be changed to the equivalent form:

$$x[n] = a \cos(\omega_c n) + b \sin(\omega_c n) \quad (25)$$

Assuming that $H(e^{j\omega_c}) = \alpha e^{j\beta}$, with α as the magnitude and β the phase, the steady-state output $y[n]$ can then be written as:

$$y[n] = a\alpha \cos(\omega_c n + \beta) + b\alpha \sin(\omega_c n + \beta) \quad (26)$$

Using this form the output $y[n]$ is linear in the parameters a and b and can be found by an adaptive algorithm. The update for these parameters was similar to the LMS method and was defined by Bertran and Montoro as:

$$a[n+1] = a[n] + \mu e[n] \cos(\omega_c n) \quad (27)$$

$$b[n+1] = b[n] + \mu e[n] \sin(\omega_c n) \quad (28)$$

where μ is a learning factor to be determined.

IV. PRECISION POINTING CONTROLLER DEVELOPMENT AND EXPERIMENTAL RESULTS

A. SCOPE

The scope of the precision pointing experiments was to evaluate the accuracy of the PPH using both small angle and large angle controllers with two slightly different PID compensators under a variety of payload orientations and trajectories. These controllers were evaluated for angular position accuracy during static (i.e. fixed orientation) and dynamic (i.e. following a commanded trajectory) tasks.

The static orientations were pseudo-randomly generated rotations about the v' (θ) and u'' (ϕ) axes, hereafter referred to as the x and y axis (i.e. the movable coordinates attached to the payload platform) between -0.8° and 0.8° . Rotation about the Z-axis was not commanded ($\Psi = 0^\circ$). The seeds used to generate the pseudo-random orientations in Simulink were 0.4 about the x-axis and 1.0 about the y-axis. The orientation was changed every 5 seconds for 250 seconds for a total of 50 different orientations. The data was recorded just prior to a new orientation being commanded to ensure steady state data were being recorded. Additionally, the transient performance of the controller was evaluated during a single command of $+1^\circ$ about the x and y-axes simultaneously. A static friction experiment was also conducted on the small angle controller to evaluate the hunting effect caused by static friction on pointing performance.

For the dynamic tasks, the controllers were evaluated for pointing accuracy during constant speed, single axis rotations and circular trajectories. The single axis trajectories were rotations about the x and y-axes individually from -1° to $+1^\circ$ at a constant rate of $0.5^\circ/\text{sec}$. This rate represented an angular rate that was approximately 5 times faster than the rate required for ground tracking in low Earth orbit. The nominal circular trajectory was a circle with a radius formed by a maximum of $\pm 1^\circ$ rotations about the x and/or y-axis and at a speed of 0.1 Hz (i.e. one circle every 10 seconds) in the clockwise direction. The experiments also included pointing accuracy evaluations at various radii (0.1° , 0.5° , and 1.0°) and various rotational frequencies (0.1, 0.5, 1, and 2 Hz). A detailed actuator control voltage experiment was also conducted on the nominal

circle trajectory in an attempt to characterize the source of the pointing errors. The controller was “tuned” at a $\pm 1^\circ$ radius at 2 Hz for all of these experiments. The controller was considered tuned when the actual trajectory trace overlaid the commanded trajectory trace, but not necessarily synchronized (e.g. lag between the commanded position and the actual position may exist). In general for the PPH, K_p and K_d shaped the actual circle trajectory (i.e. elongated it in either the x or y direction and determined the radius), while K_i was the dominant gain controlling how well the actual and commanded trajectories were synchronized. $K_i = 6$ was chosen from trial and error as a reasonable gain to keep the system stable and minimize synchronization errors; it remained fixed for all of the experiments.

B. EXPERIMENTAL SETUP AND CALIBRATION

1. ControlDesk Application

As mentioned in Chapter II, the primary interface between the operator and the PPH was through the host computer using the dSPACE application, ControlDesk. Figure 17 illustrates the typical graphical user interface (GUI) created to control and conduct the experiments once the models were built in Simulink and converted to C using the Real Time Workshop. This interface allowed the operator to control the input commands to the hexapod (i.e. circles, manual, random angles, ramps, etc), allowed real-time adjustment of the PID gains, real-time monitoring of all sensors both numerically and graphically, monitoring of actuator commands, and data recording control.

2. Sensor Calibration

a. Alignment

The Kaman eddy current sensors had to be calibrated such that at the desired initial conditions (no tip/tilt/twist/translation), the sensors reported identical displacements which when transformed using (22) and (23), read zero degrees for tip and tilt (i.e. ϕ and θ). For the other degrees of freedom (translation and twist), the vertical Kaman Sensors provided no useful information and were not used in the control laws or feedback. This greatly simplified the control problem from six degrees of freedom to two degrees of freedom: one about the x-axis and the other about the y-axis.

The sensors were calibrated using the bipolar method described in the sensor operator's manual, reference [36], and Plexiglas spacers of known thickness. Each spacer had a thickness of 2.244 ± 0.003 mm and a unique set of five spacers were used to calibrate each sensor. The spacers were required for the minimum displacement distance (1 spacer), nominal displacement distance (4 spacers), and the maximum displacement distance (5 spacers) from the target for calibration. Manual translation along the Z-axis of the payload platform using the ControlDesk GUI ensured the spacers were firmly positioned between the sensor and the target during calibration. The sensor output signal was conditioned through a noise filter resulting in about a 4dB signal loss and was then sent through a low pass filter (corner frequency = 4.78 Hz or 3.0 rad/sec) in Simulink to filter the remaining high frequency noise. All sensor calibrations were done post-filtering using the values reported in ControlDesk.

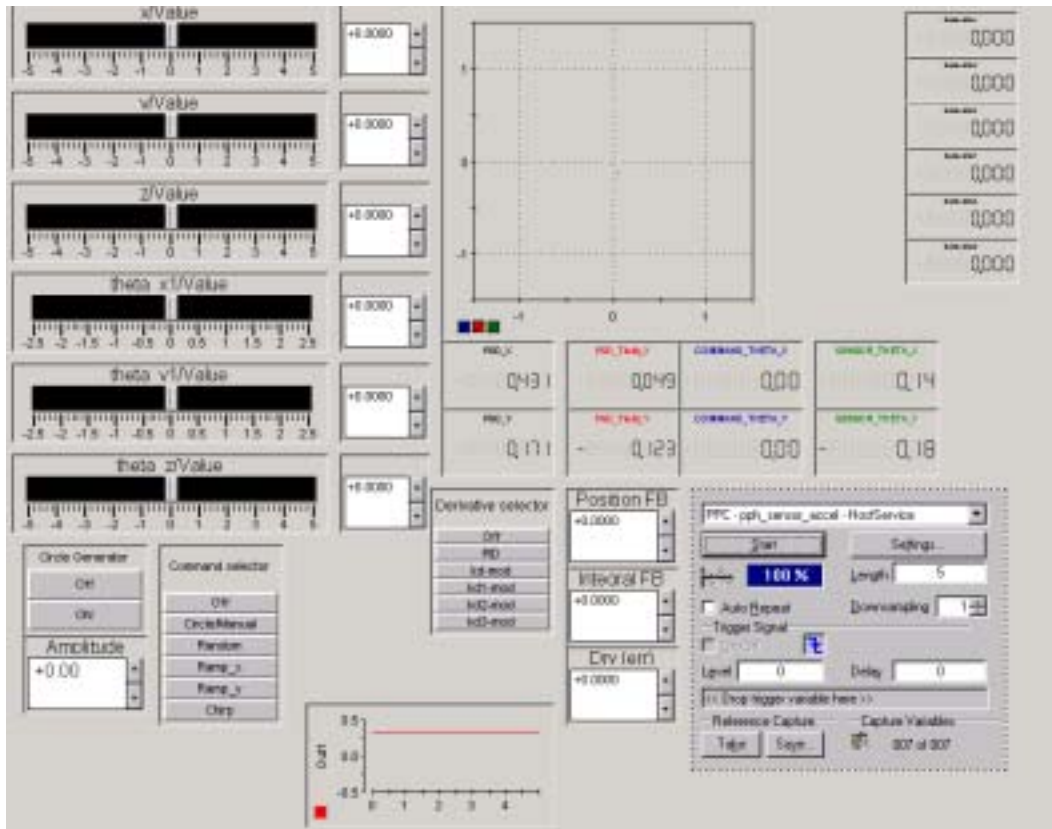


Figure 17 Typical Control Desk Operator Interface

To verify that these sensors were adequately calibrated and that the displacement-to-angular measurement transformation equations (22) and (23) were properly implemented, qualitative and quantitative techniques were employed.

Qualitatively, the angular displacement response to an angular position command about either axis was reasonable in magnitude and direction. Cross-coupling was apparent, but not significant, and some was to be expected due to the “ride along” effect cited in [34], which states that there will be motion in all actuators for a single actuator command causing unintended translation and/or rotation in the open loop. An example illustrating these results can be seen in Section C of this chapter where the open loop single-axis trajectories are shown (Figure 25).

Quantitative verification using the position-sensing device (PSD) was then conducted, but was limited by the special attention required to obtain an accurate angular reference using the PSD. In order to obtain an angular measurement from the PSD that was equal to the rotation angle of the payload platform, the laser light had to be precisely centered on the photo-diode and the offset distance between the photo-diode and the center of rotation of the payload platform (i.e. point P) where the laser was located, had to be accurately known and remain stationary during operation. With that, and the lateral displacement of the laser measured by the photo diode, the angular displacement could be determined using the \tan^{-1} trigonometric function. Using this setup, the payload platform was free to twist and translate as it was rotated about the x and/or y-axis. This caused a problem in that the center of rotation of the payload platform could be easily misaligned with the center of the photo-diode from which the angular displacements were measured. Figure 18 illustrates the problem. Furthermore,

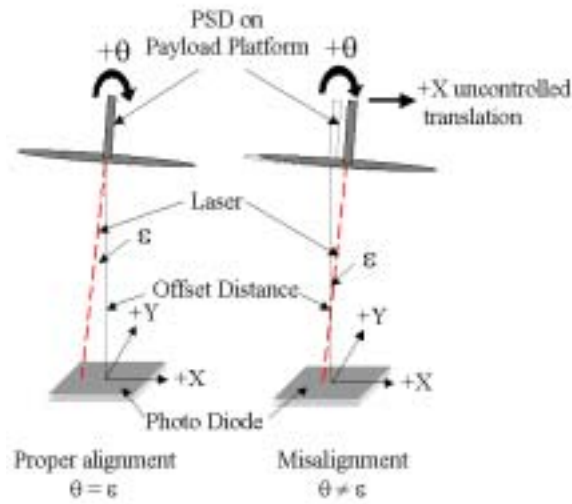


Figure 18 Position Sensing Device Angular Measurement and Error Illustration

such translation and twist was not observable with any sensor and therefore was not controlled. As a result, as the payload platform was tipped or tilted, there was either some vertical or horizontal translation that resulted in erroneous angular calculations from the PSD readings. Figure 19 and Figure 20 illustrate the results. Using an open loop control scheme, these plots show the magnitudes of the total error vs. commanded position. For each plot, the payload platform was initially at the nominal zero tip/tilt position and the angular displacement about an axis was increased to the maximum allowable by the PSD (1.5 degrees). It was then reset to the nominal position and a negative rotation was commanded. This was done for rotations about both the x and y-axes. As shown by the figure, small rotations about either axis resulted in fairly constant errors (which were correctable with proper calibration), however as the commanded angles became greater than about $\pm 0.25^\circ$ to $\pm 0.5^\circ$, the errors began to grow. This was expected since the angular measurements from the Kaman sensors were unaffected by the lateral translations of the payload platform, while the angular measurements using the PSD were significantly affected. Therefore, based on the small angle results obtained, it was inferred that the Kaman sensors were properly aligned and the transformation equations were indeed correct. Furthermore, due to the indeterminate nature of the payload platform orientation with a single PSD, the derived angular displacements measured from the Kaman sensors were considered as the output for the system throughout this thesis.

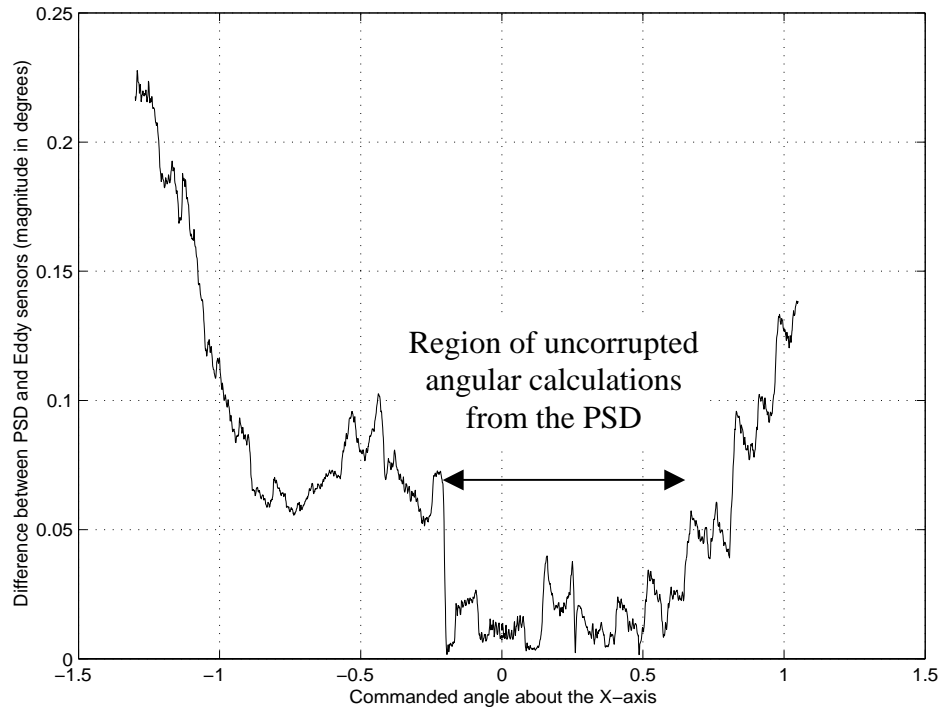


Figure 19 Differences in Kaman and PSD Sensor Angular Displacement Measurements for Rotations about the X-axis

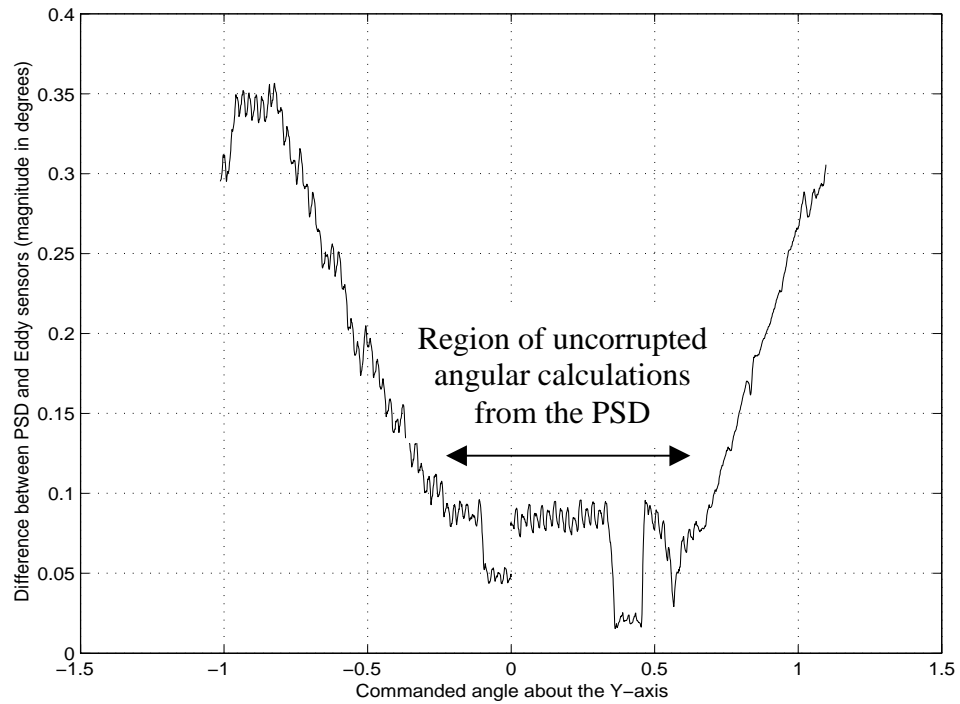


Figure 20 Differences in Kaman and PSD Sensor Angular Displacement Measurements for Rotations about the Y-axis

b. Sensor Precision

Once the sensor alignment and calibration was verified, the next step was to evaluate the level of precision of the sensors. The source of errors from these sensors included the noise on each sensor, errors associated with the small angle approximations used in transforming the sensor displacements into angular displacements, the errors associated with an angular offset of the sensor to the target, and the measurement errors of the spacers used for calibration. The target plates were assumed to be a level reference for these calculations. Table 9 summarizes the errors.

Table 9 Measurement Errors

Parameter	Displacement Accuracy	Angular Error
Sensor Noise	± 0.002 mm	$\pm 0.0010^\circ$ (17 μ rad)
Small Angle Approximation (2.5° maximum angle-PPH limited)	N/A	$\pm 0.0008^\circ$ (14 μ rad)
Sensor to Target angular offset error ($\pm 2.36^\circ$ maximum angle-sensor limited)	N/A	$\pm 0.0020^\circ$ (35 μ rad)
Spacer Error	± 0.01 mm	$\pm 0.0075^\circ$ (131 μ rad)
Total Total (corrected)		$\pm 0.0113^\circ$ (197 μrad) $\pm 0.0038^\circ$ (66 μrad).

Figure 21 and Figure 22 illustrate the sensor noise induced error in position displacement and in angular displacement. In order to minimize the noise present on each sensor, an extensive investigation into the noise sources was conducted. It was determined that a significant source of noise was the PPH power amplifiers. When turned on, the electromagnetic interference generated by the amplifiers coupled into the power source, which happened to be the same power source as the Kaman sensors. Therefore, the power to the Kaman sensors was placed on a completely different power circuit from the rest of the system. That, in addition to the noise filter in the control box, reduced the sensor noise induced errors to the reported level. The small angle approximations were used in the sensor transformation equations to convert the sensed displacement into angular displacement. The PPH was designed to have a

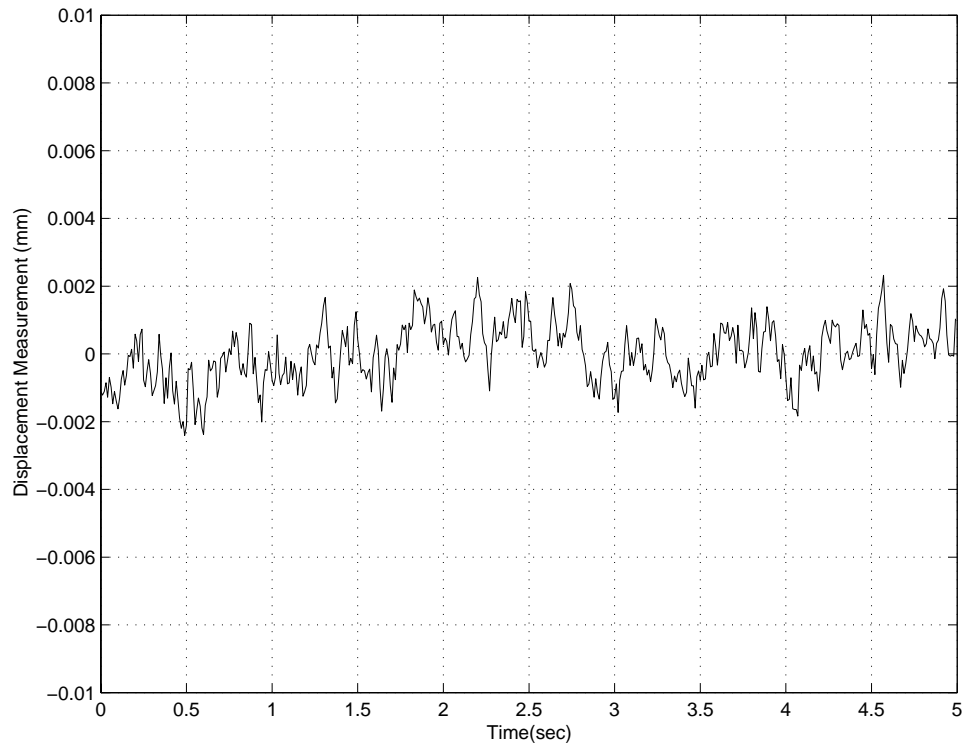


Figure 21 Sensor Noise Induced Displacement Error

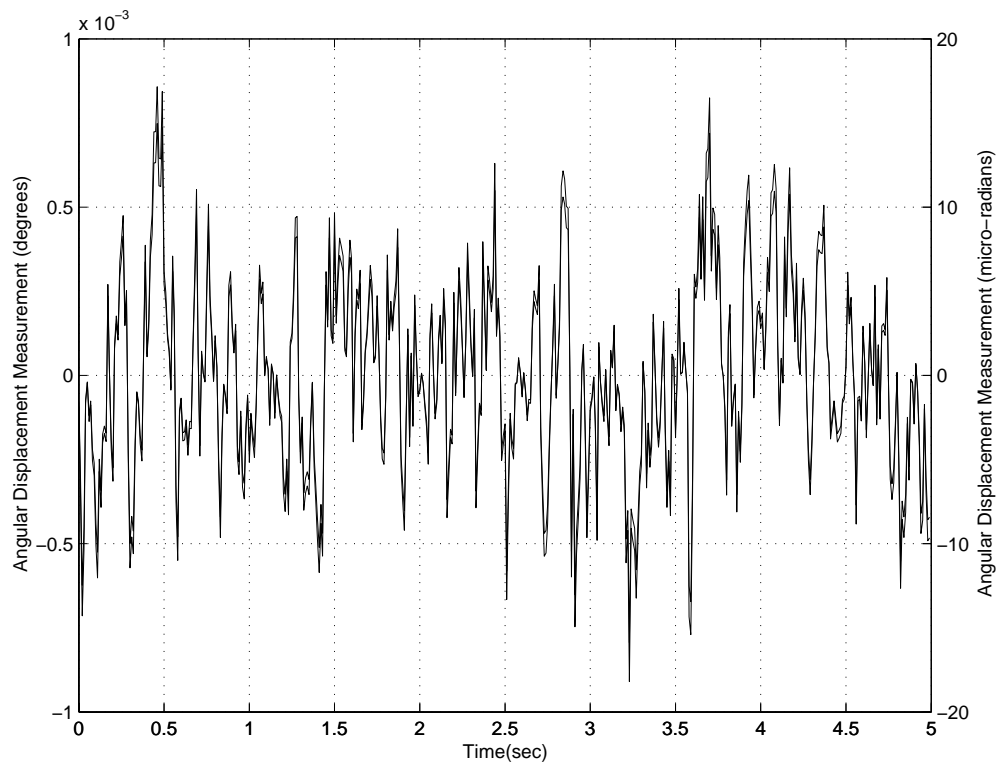


Figure 22 Sensor Noise Induced Angular Displacement Error

maximum rotation about the x-axis (ϕ) and y-axis (θ) of $\pm 2.5^\circ$, thus limiting the error caused by the small angle approximation to $\pm 0.0008^\circ$ (14 μrad). The sensor-to-target offset angle error was caused by a misalignment of the sensor face to the target (i.e. faces not parallel) as shown in Figure 23. This misalignment occurred anytime the

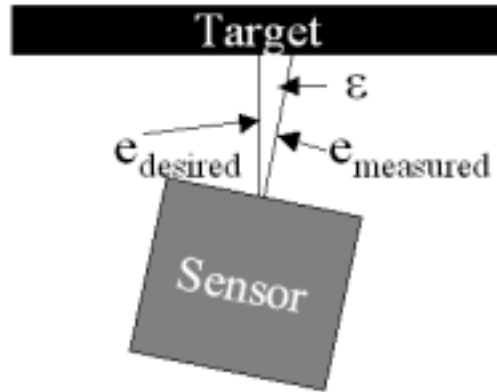


Figure 23 Sensor-to-Target Offset Angle Error

payload platform was actually rotated. The resulting error affected the displacements measured by the Kaman sensor such that $e_{\text{desired}} = e_{\text{measured}} |\cos(\epsilon)|$. Since the Kaman sensors were limited to measuring displacements that were no greater than 12.7 mm from the target, the maximum angular displacement that could be calculated from the Kaman sensor in the configuration was $\epsilon = \pm 2.36^\circ$. Since ϵ was not be easily determined at each sensor, the $\cos(\epsilon)$ term was neglected, inducing the error. Finally, the spacer error was a result of the variability in spacer thickness. While the spacers could be measured to ± 0.001 mm, the thickness between spacers varied by ± 0.003 mm. Spacers for each sensor were selected to keep the total spacer error of five spacers to within ± 0.01 mm. The use of more accurate spacers (e.g. calibrated ceramic spacers) could easily reduce these errors by an order of magnitude, however for the purposes of these experiments, an accuracy of ± 0.01 mm was sufficient. Furthermore, the spacer error was a constant and did not contribute to the variability in the results obtained. Consequently, for these experiments, the spacer error was subtracted from the total error resulting in a corrected pointing accuracy of $\pm 0.0038^\circ$ (66 μrad). However for a deployed system, the spacer errors would have to be added to properly characterize the system accuracy.

C. SMALL ANGLE CONTROLLER (JACOBIAN MODEL)

The first controller was the small angle controller illustrated in Figure 24. This controller implemented equation (10), evaluated at the nominal payload platform position, with a PID compensator. For this controller, it was assumed that a ± 1 -volt input to an actuator resulted in a ± 1 mm change in actuator length. Two Jacobian matrices and two PID compensators were evaluated for angular positioning accuracy.

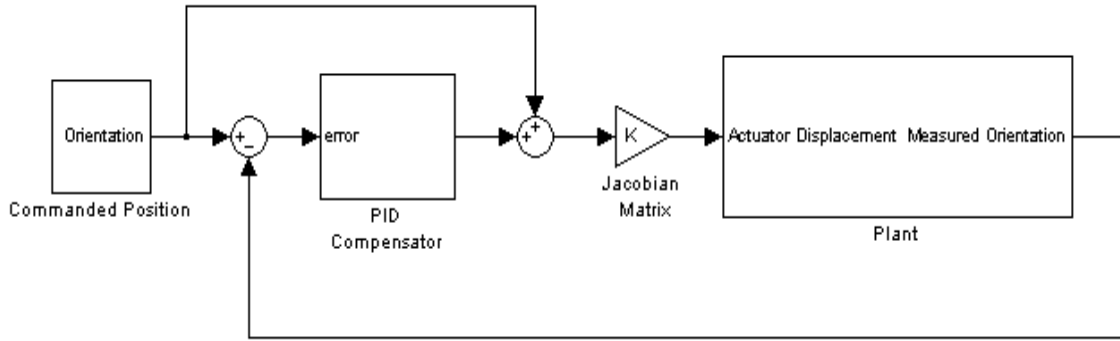


Figure 24 Small Angle controller Model

1. Jacobian Selection

The two Jacobian matrices implemented were the manufacturer provided transformation matrix and a kinematically derived Jacobian matrix from equation (14). The manufacturer provided transformation matrix was derived from the system dynamics equations using a finite element model of the PPH at the nominal zero position. The resulting matrix was then normalized column-wise, such that the highest value in each column was considered one. This matrix was considered constant throughout the range of the PPH, although strictly speaking, it had to be recalculated for every new position of the payload platform. This matrix and the program used to develop it are shown in Appendix A. Similarly, the derived Jacobian matrix was also considered constant throughout its range, however it was not normalized like the manufacturer provided matrix. Figure 25 shows the open loop results (i.e. without PID compensator) for single axis commands about the x and y-axis (ϕ and θ respectively) at a rate of $0.5^\circ/\text{sec}$ for the manufacturer provided Jacobian matrix. Figure 26 shows the same thing for the derived Jacobian matrix. Comparing the figures, it can be seen that

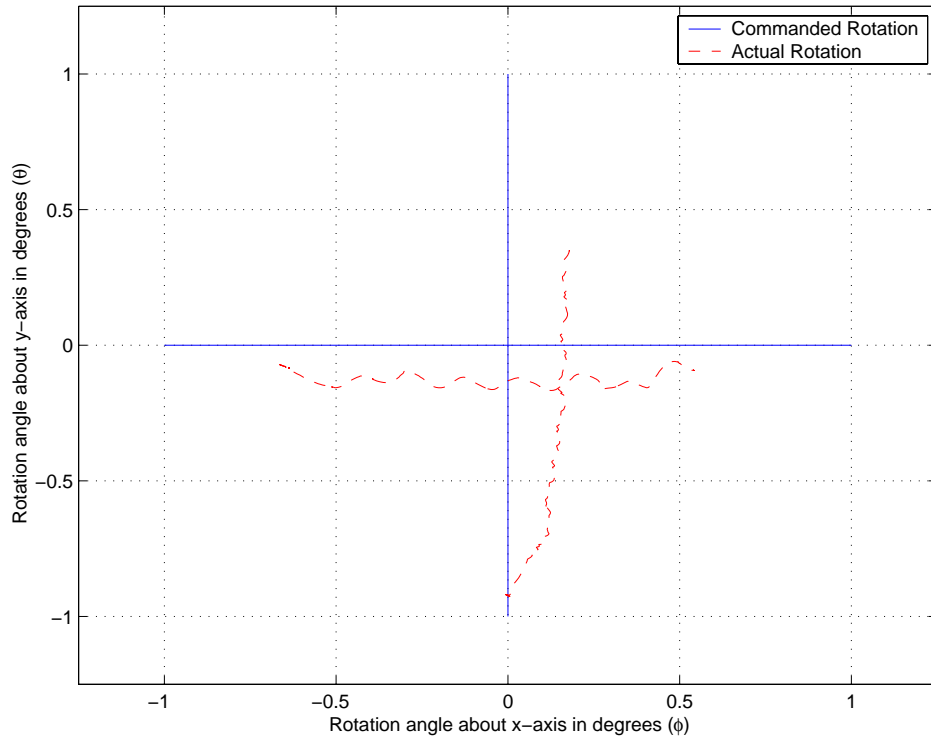


Figure 25 Response to Single-Axis Rotations using the Manufacturer provided Transformation Matrix

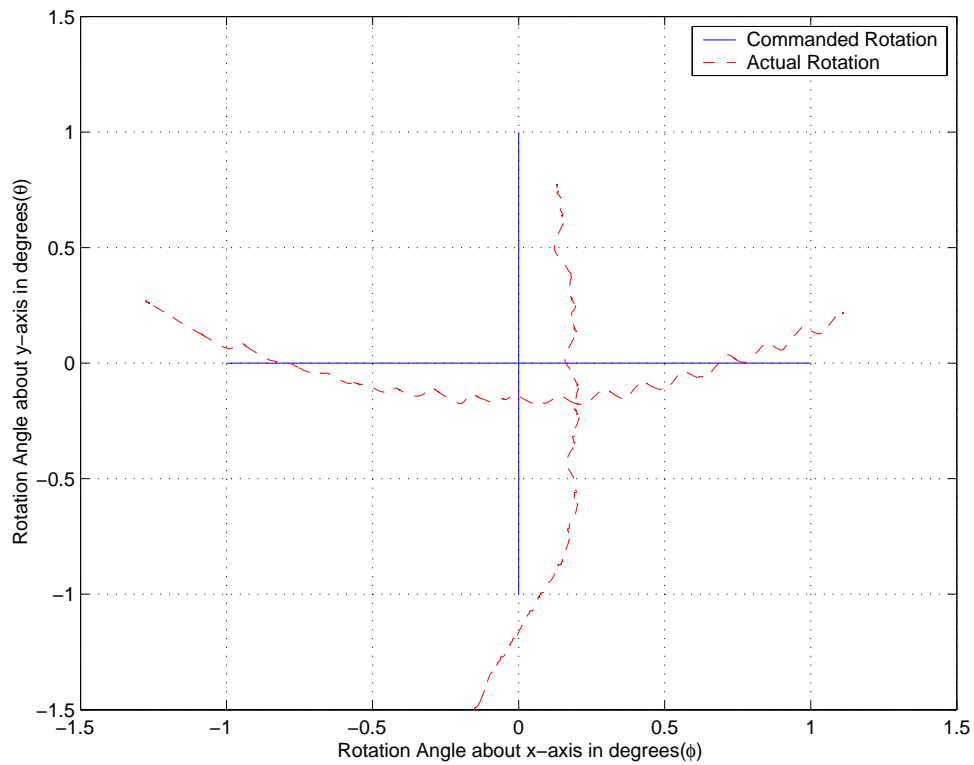


Figure 26 Response to Single-Axis Rotations using the Derived Jacobian Matrix

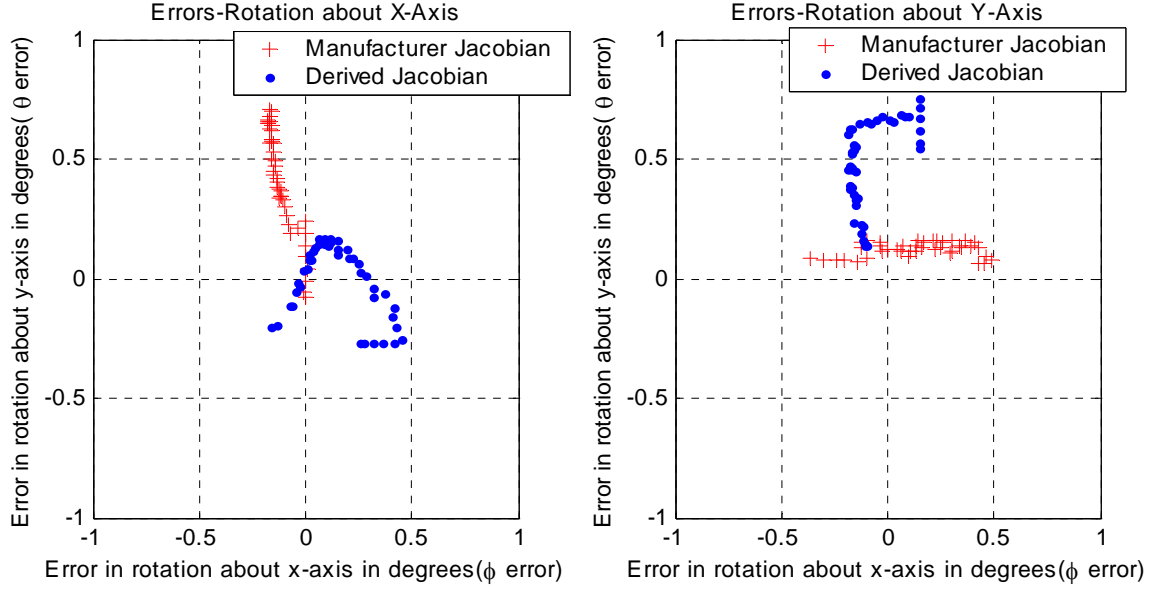


Figure 27 Error Comparison of the Different Transformation Matrices

there was some cross-coupling in both models especially for rotations about the x-axis. Furthermore, the errors seen in the manufacturer provided matrix seemed to be a nearly linear offset from the axis orthogonal to the axis of rotation as shown in Figure 27. This was not the case for the derived matrix, which exhibited a curved trajectory when compared to the commanded trajectory, although the magnitudes of the offsets were nearly the same. One possible explanation for this difference is that the manufacturer provided matrix considers payload moments of inertia and actuator stiffness, while the derived Jacobian requires merely the distance between plates and the actuator length. Thus the manufacturer provided matrix provides a better, albeit linear, approximation of the hexapod dynamics resulting in the linear offset observed. Additionally, the manufacturer provided matrix caused the ends of the actual trajectories to be clipped, shortening them when compared to the commanded trajectory, while the derived Jacobian matrix did not. This is most likely a result of the normalization done on the manufacturer provided matrix, causing an insufficient actuator length to be commanded because all values within the matrix were normalized to one. In the end, there was little difference between the accuracy of one transformation matrix over the other. The derived Jacobian matrix was used for the remainder of the experiments to eliminate the need for manufacturer assistance should a decoupling problem arise later.

2. Standard PID Controller

The first PID compensator used is illustrated in Figure 28. The compensator was fairly standard in that it had gains on the displacement error, its integral, and its derivative. One addition was the incorporation of an anti-wind up algorithm on the integral compensator. This prevented the generation of a large actuator output resulting from a large instantaneous difference in commanded position to actual position. This anti-wind up algorithm prevented the integral command from affecting the compensator output if its contribution was greater than or equal to 2° . If the command was greater or equal to 2° a zero gain was applied to the integral compensator until the error was less than 2° . The PID compensator with the PSD mounted on the payload platform was tuned as described in Section A and the gains were determined to be $K_p=2$, $K_i=6$, and $K_d=0.17$. The bode diagram for this PID compensator is shown in Figure 29.

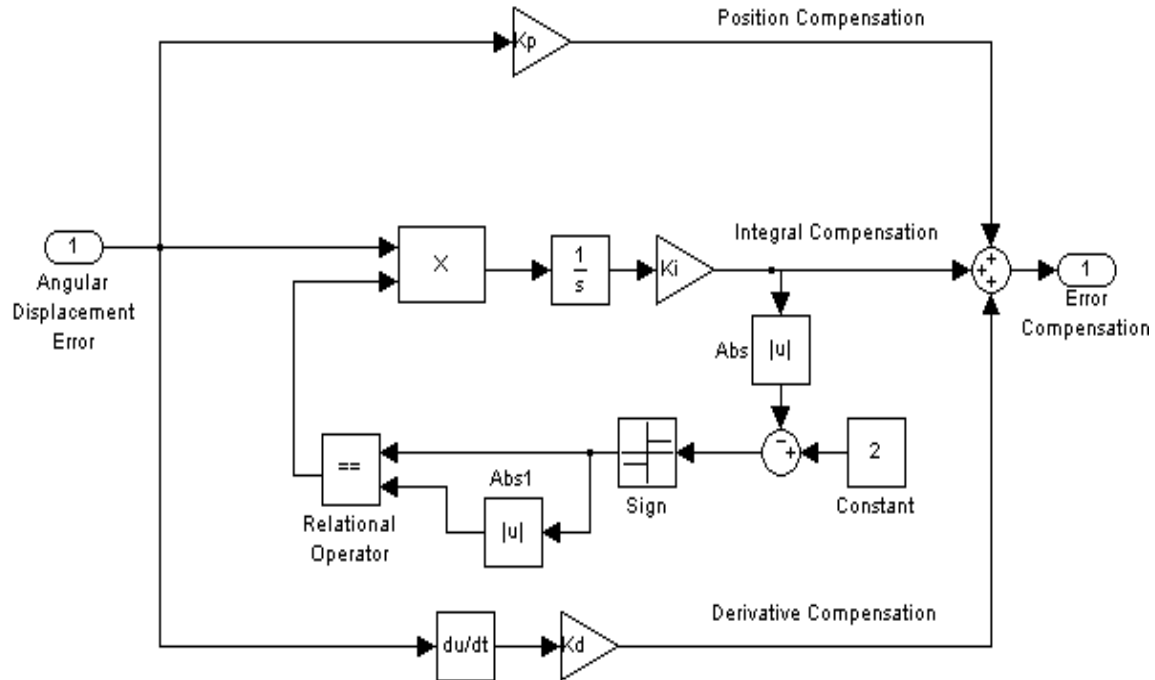


Figure 28 PID Controller Block Diagram

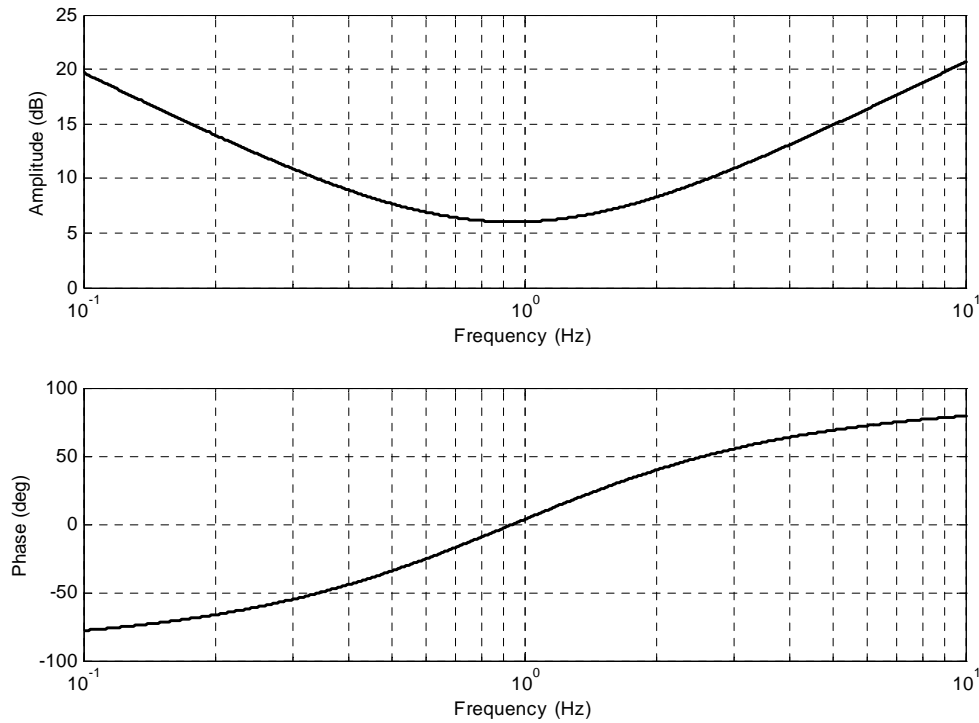


Figure 29 Bode Diagram for the Standard PID Compensator ($K_p=2$, $K_i=6$, and $K_d=0.17$)

a. Static Pointing Results for Standard PID Controller

The results of the static pointing experiment are shown in Figure 30. The open loop commands had angular errors that were around $\pm 0.4^\circ$. The closed loop errors with the standard PID compensator showed well over an order of magnitude improvement over the open loop with errors that were within $\pm 0.008^\circ$ (Figure 44 shows the magnified view of the closed loop errors). Figure 31 illustrates the transient performance of the PPH using the standard PID compensator. What was noted was the instantaneous error immediately after the commanded time, followed by a single overshoot and convergence to the steady state solution of $\pm 0.008^\circ$ within 2 seconds. The amount of overshoot was dependent on the axis of rotation and the magnitude of the command, but was no greater than 0.2° for either axis for commands up to $\pm 1.0^\circ$ ($+1^\circ$ command shown).

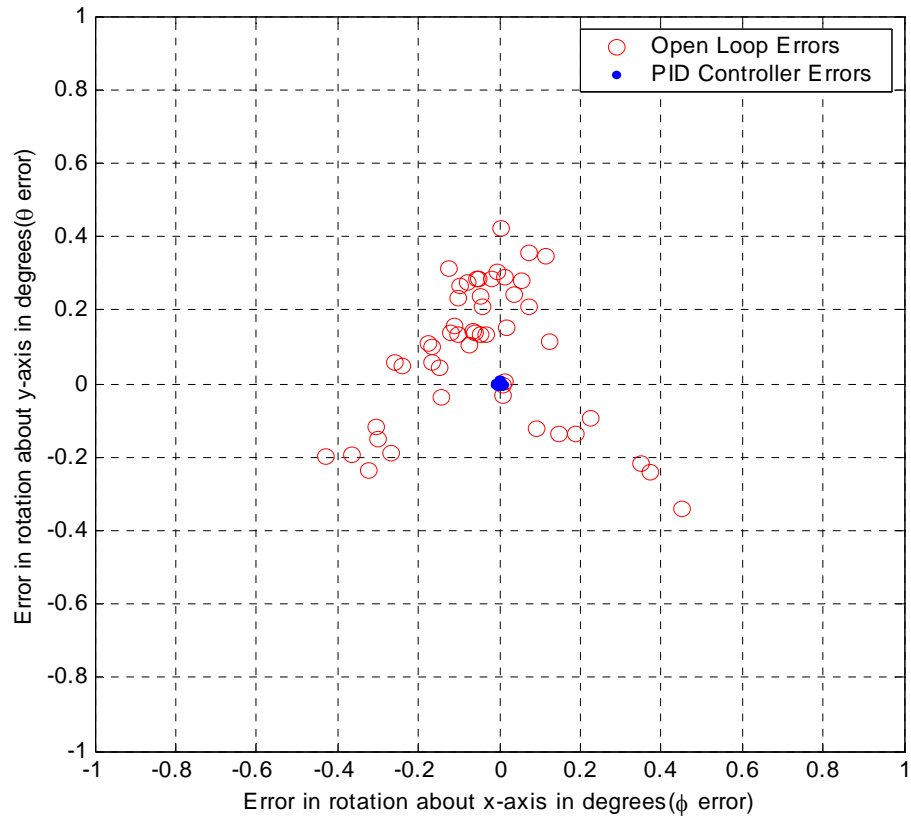


Figure 30 ϕ and θ Errors for Static Commands

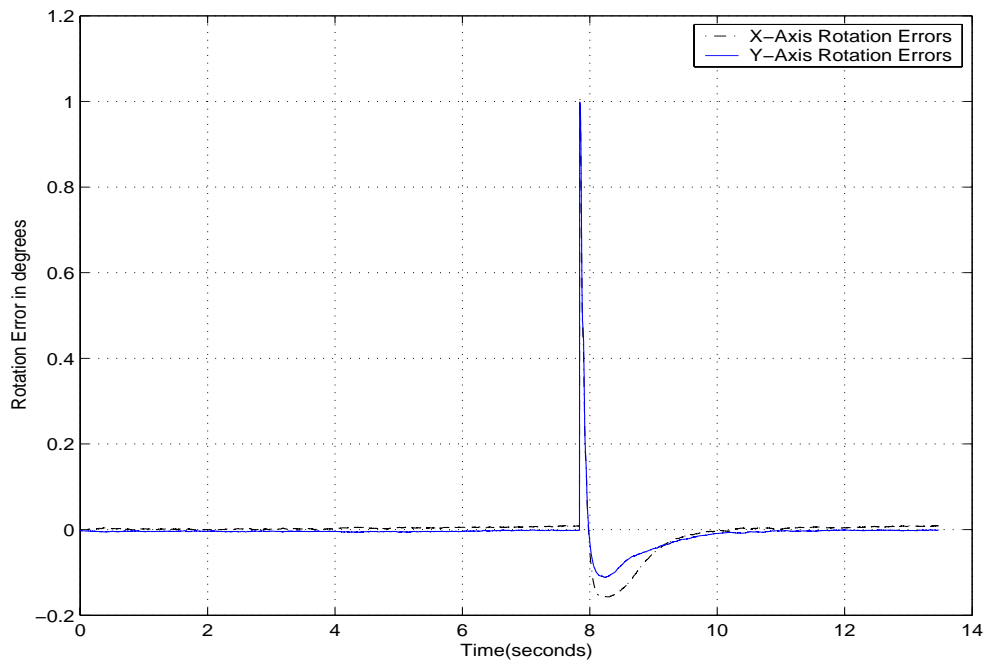


Figure 31 PID Transient Performance for Simultaneous $+1^\circ$ Rotations about the x and y-axes

Actuator bushing static friction was also investigated for its effect on pointing accuracy. Figure 32 illustrates the payload rotations about the x-axis when 0° was commanded about both the x and y-axes. Rather than observing a straight line at 0° , what was seen was a phenomenon known as hunting [37]. In this instance, the static friction force of the bushings in the actuators opposed the commanded force (which translates to actuator displacement distance) initiated by the controller. As the commanded force was built up (due to the integrator portion of the PID compensator), the static friction force was eventually overcome, resulting in sudden actuator movement and payload platform rotation. The force generated however, was greater than the force required to rotate the payload platform to the commanded position, and an overshoot occurred. The cycle was thus repeated (at approximately 1 Hz) making the controller appear to “hunt” for the commanded position. The result was that a static pointing accuracy of less than $\pm 0.005^\circ$ could not be achieved about the x-axis. Similar results were obtained for the y-axis.

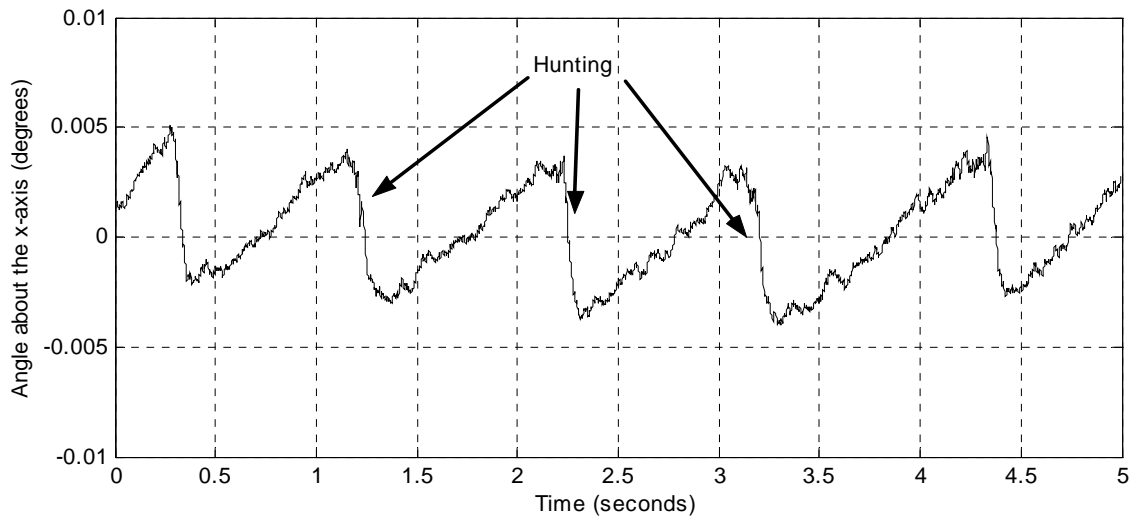


Figure 32 Static Hunting about the X-axis

b. Dynamic Tracking Results for Standard PID Controller

(1) Single Axis Tracking. The single axis tracking results of the standard compensator are shown in Figure 33 and Figure 34. Figure 34 shows tracking errors that were less than $\pm 0.05^\circ$ for rotations about either axis, which was an order of magnitude improvement over the open loop case.

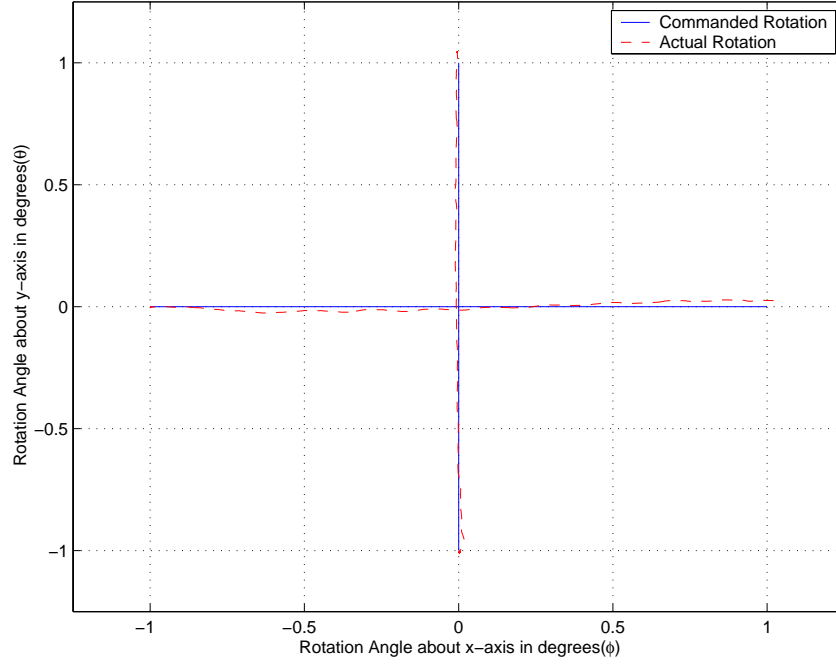


Figure 33 Commanded and Actual Trajectories for Single Axis Rotations

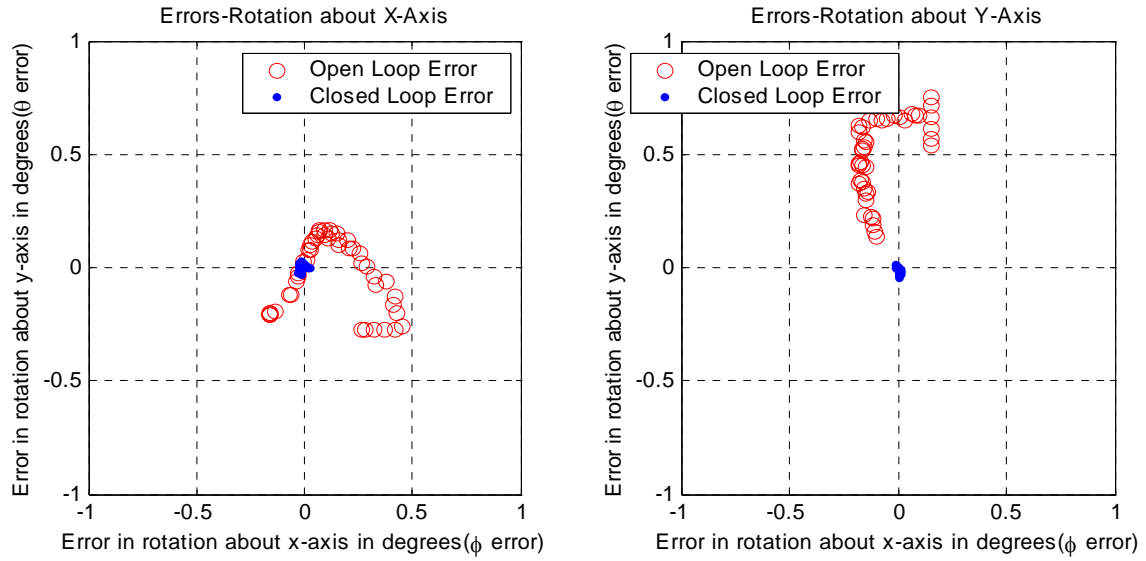


Figure 34 Differences between Open Loop and Closed Loop ϕ and θ Errors for Single Axis Rotations

(2) Circular Trajectory Tracking. Figure 35 through Figure 42 show the results of the circular trajectory experiments using the standard compensators. Figure 35 compares the open loop and closed loop trajectories for the nominal trajectory ($\pm 1^\circ$ at 0.1 Hz) with the commanded trajectory. Figure 36 shows the errors for this

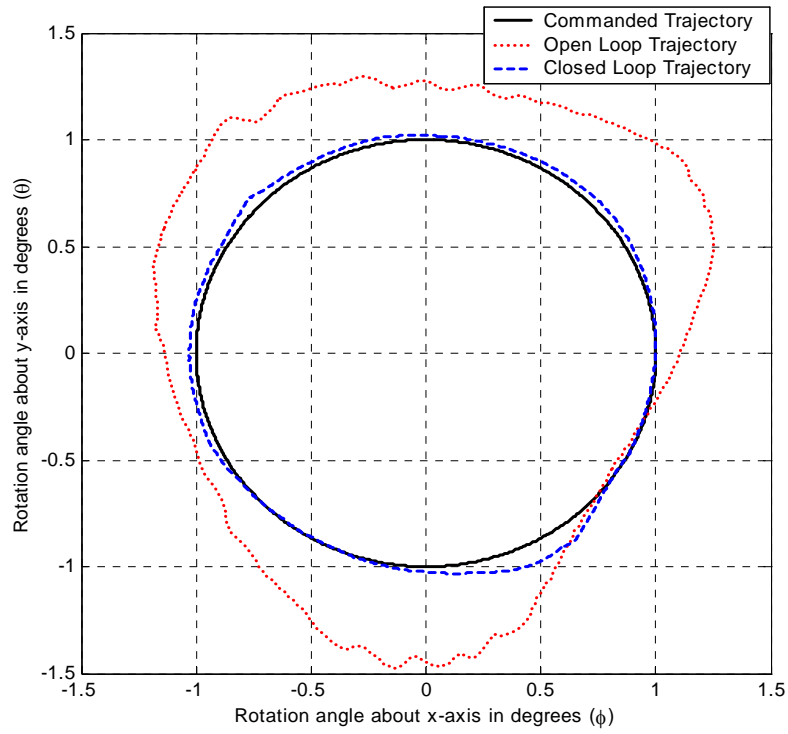


Figure 35 Nominal Circular Tracking Trajectories ($\pm 1^\circ$ at 0.1 Hz)

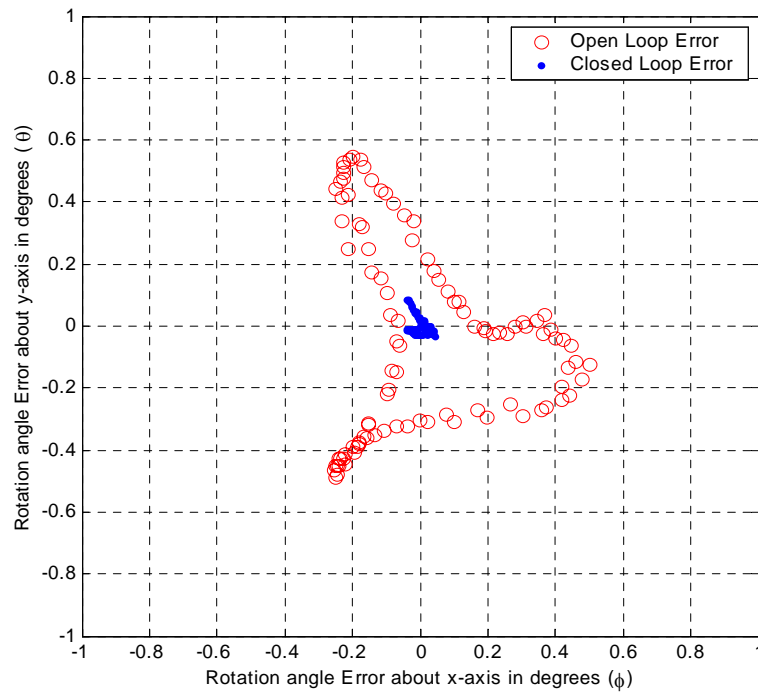


Figure 36 ϕ and θ Errors for Nominal Circular Tracking Trajectories ($\pm 1^\circ$ at 0.1 Hz)

tracking trajectory which resulted in open loop errors of $\pm 0.6^\circ$ and closed loop errors of $\pm 0.1^\circ$; a factor of 6 improvement. Interestingly, the shapes of the error plots were similar for the open loop and closed loop rotations, indicating that the same phenomenon (possibly actuator static friction) was occurring in both cases. These error plots were also repeatable between cycles and between runs, again indicating that a specific phenomenon was occurring, thus leading to the evaluation of the actuator commands shown in Figure 37. This figure shows two significant time frames where actuators # 1 and #6 (the actuators straddling the x-axis) were stationary (3.5 – 6 sec and 9 – 11 sec (start of next circle)). Correspondingly, there were large errors between the commanded trajectory and the actual closed loop trajectory at those times. This seems to indicate that the presence of static friction in actuators #1 and #6 may have contributed to these errors at those times. However, the lack of significant tracking errors during times when other actuators were stationary, and the fact that the local maximum tracking error at 9 seconds occurred just as the #1 and #6 actuators became stationary and not at some later time, indicate that some other phenomenon was contributing to the tracking error in addition to static friction. While further tests are required to better characterize these errors, it is reasonable to assert that static friction may have contributed to the large tracking errors seen at 3.5 and 9 seconds. The similarity in shape of the open loop and closed loop error plots and the repeatability of these errors tend to substantiate that assertion.

Figure 38 shows the resultant tracking errors for various radii during the 0.1 Hz circle trajectories. Not surprisingly, the error was not significantly different at different radii because of the slow speed. However, as the speed of the circle increased to 2 Hz, the errors were no longer independent of radius size as seen in Figure 39. Figure 40 further illustrates the dependence between circle speed and error. Clearly, increasing the tracking speed increases the error invoked, with errors as great as $\pm 0.2^\circ$ seen at 2 Hz. What was also seen was that the error plots also tended to rotate counterclockwise as the circle trajectory speed increased. Figure 41 shows that the direction of rotation of the error plots were also reversed when circle direction was reversed. The lag in response was consistent with the phase change expected from the PID compensator (as seen in the bode diagram in Figure 29).

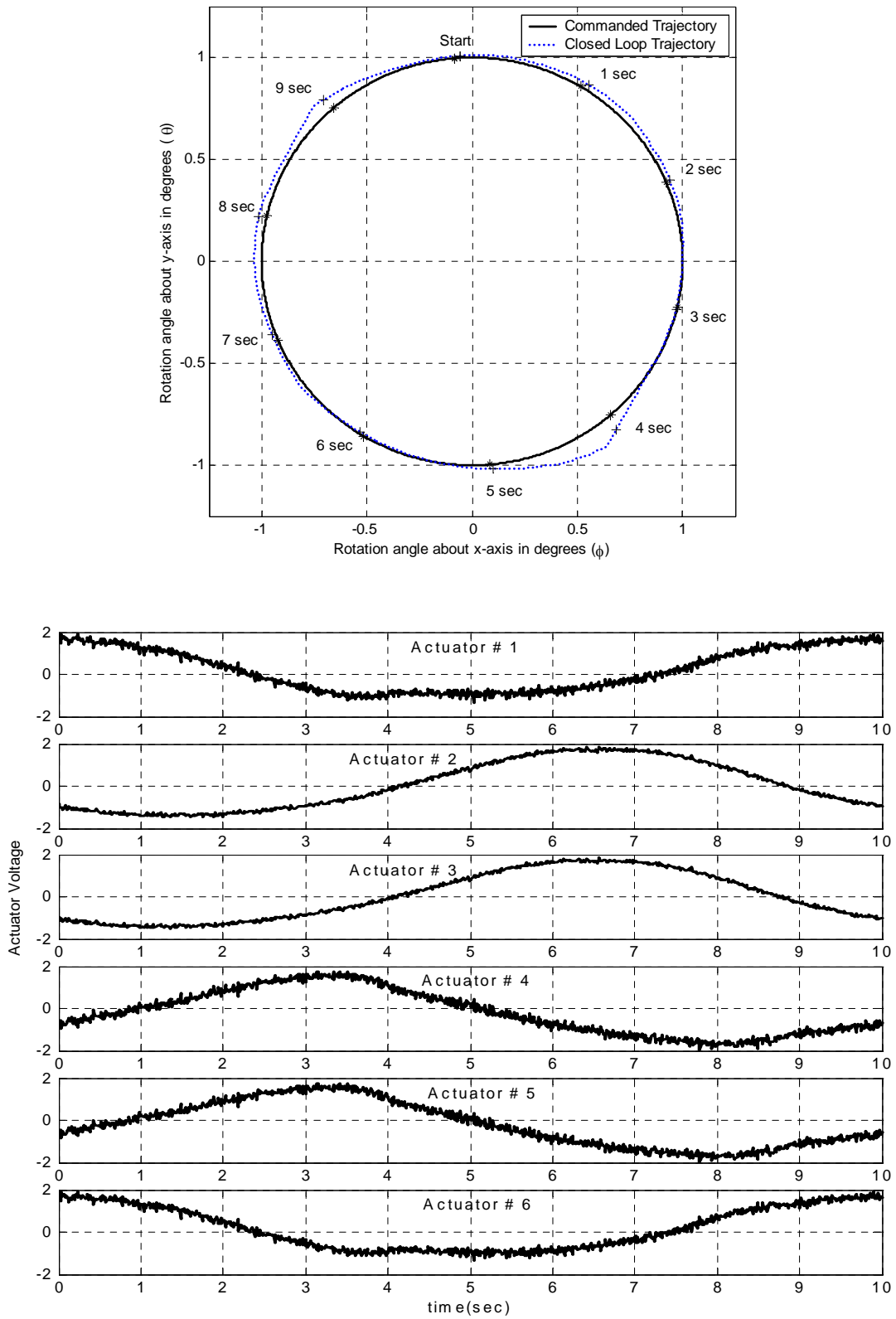


Figure 37 Actuator Voltage Commands for Nominal Circular Trajectory

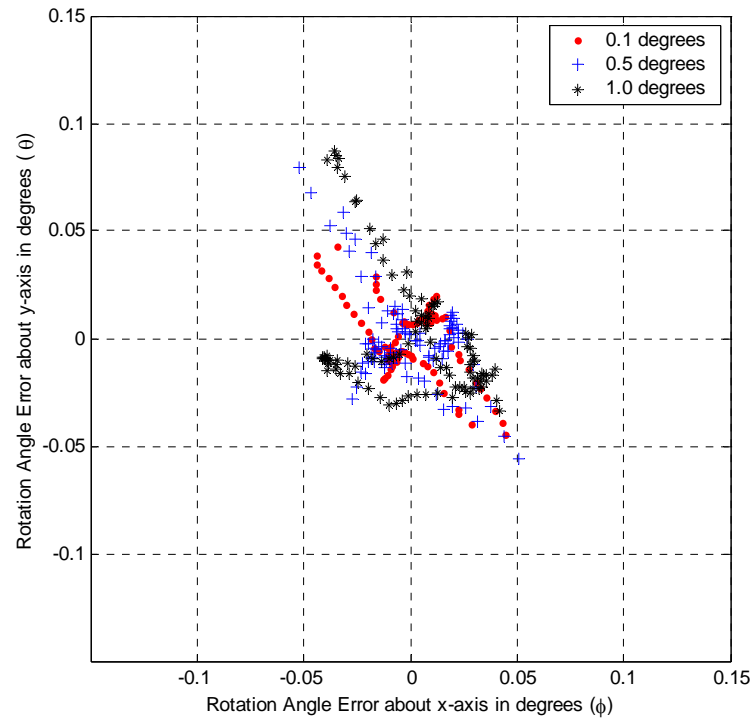


Figure 38 ϕ and θ Errors Corresponding to 0.1 Hz Circular Trajectories for Various Radii

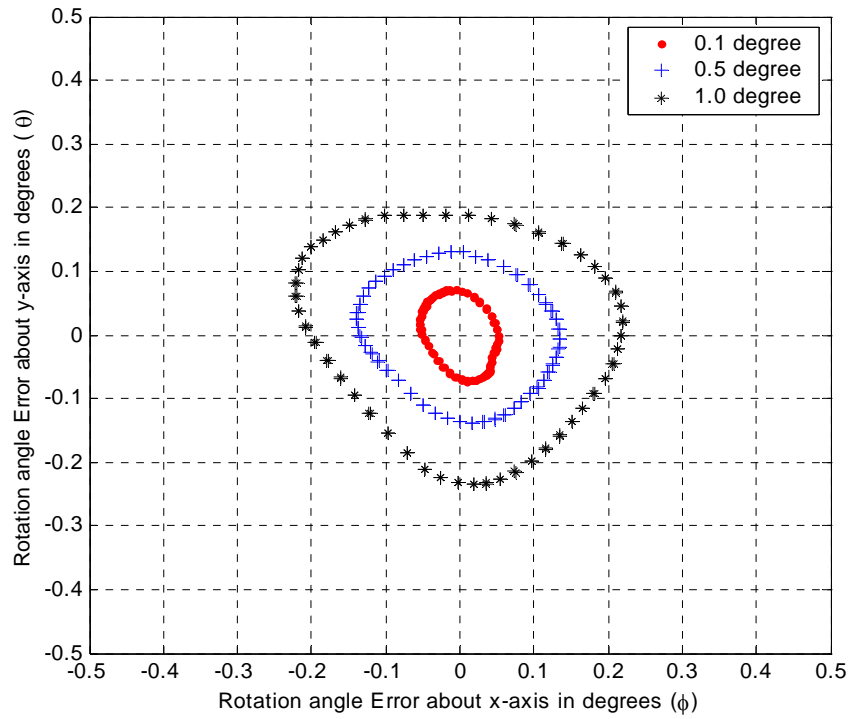


Figure 39 ϕ and θ Errors Corresponding to 2.0 Hz Circular Trajectories for Various Radii

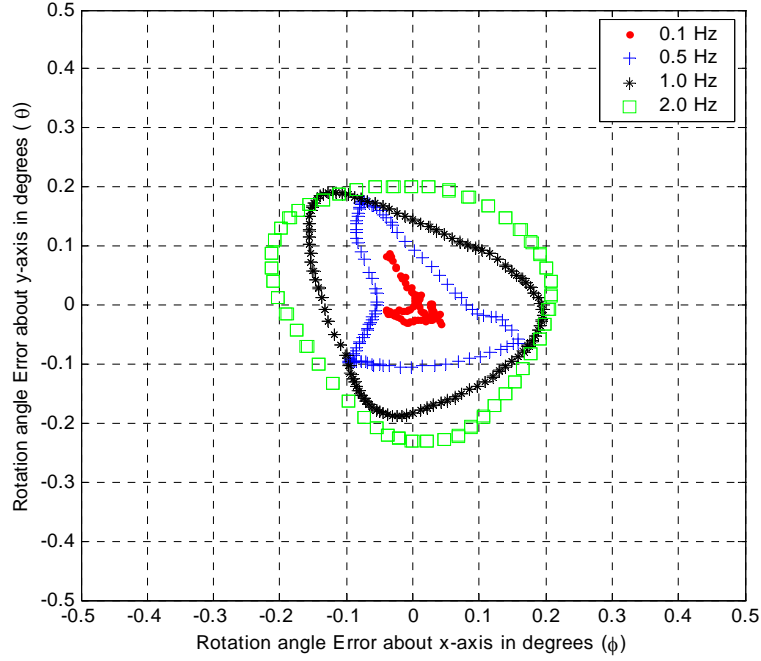


Figure 40 ϕ and θ Errors Corresponding to Clockwise, 1.0° Radius, Circular Trajectories for Various Tracking Speeds

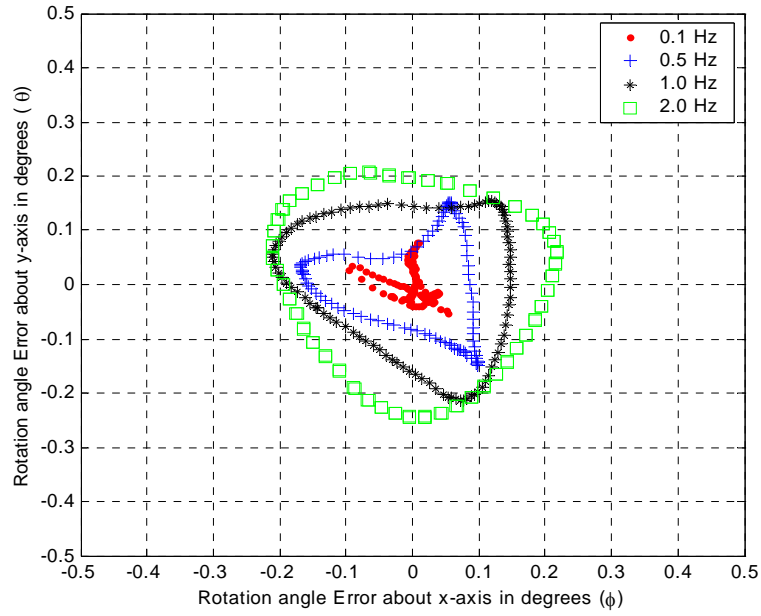


Figure 41 ϕ and θ Errors Corresponding to Counter-Clockwise, 1.0° Radius, Circular Trajectories for Various Tracking Speeds

Figure 42 illustrates the circular tracking trajectories for various tracking speeds with the PID gains fixed. The trace of the 0.1 Hz and 2 Hz circles were nearly coincident on the command trace. In the first case (0.1 Hz), the command and actual trajectories were nearly synchronized; however for the 2 Hz trajectories, a lag existed between the actual and commanded traces resulting in the large pointing errors. The 0.5 Hz and the 1 Hz traces were not coincident with the commanded trace and in fact were both larger than the commanded trajectory. Since the PID gains were tuned for one frequency (2 Hz), it became clear that these same gains were not sufficient at different speeds to minimize the error. Thus, this compensator was dependent on tracking speed, requiring gain adjustments accordingly to compensate for the changes in payload speed for optimal pointing performance. Unfortunately, such analysis is beyond the scope of this thesis but could be implemented with an adaptive algorithm or a look-up table.

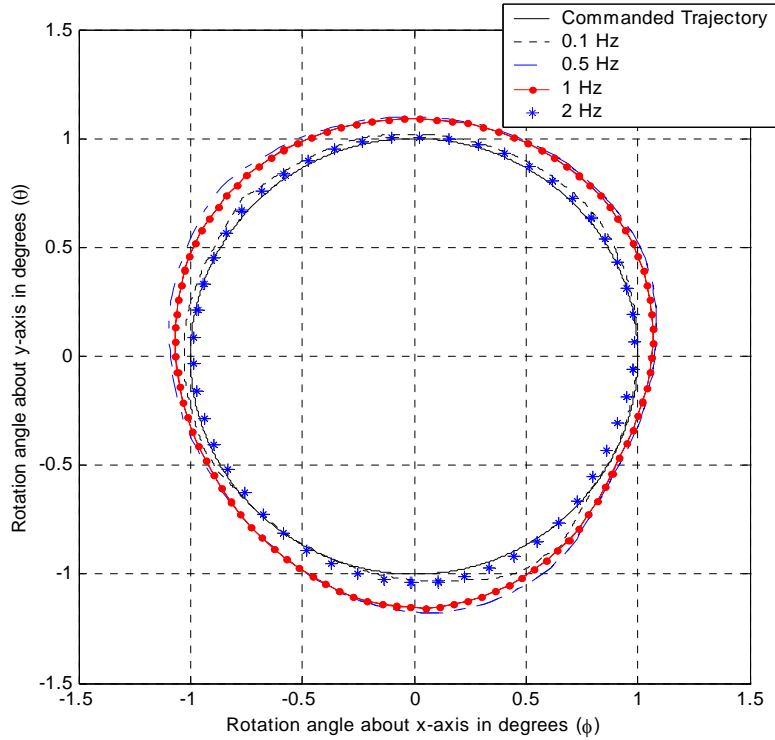


Figure 42

Circular Tracking Trajectories for Various Tracking Speeds (1° radius)

3. Modified-PID Compensator

The second PID compensator evaluated, referred to as the modified-PID (mod-PID) compensator, is illustrated in Figure 43. The difference between this compensator and the standard PID compensator was in the derivative compensation part of the compensator. Essentially, a low pass filter was implemented to filter the high frequency noise accompanying the derivative of the error signal. This noise could be heard audibly, however it was at a too high of frequency to be captured by the accelerometers. This filter was applied to both axes identically with the same taming factor, $N=150$, in both axes [34]. For these experiments, the gains and payload configuration was identical to that of the standard PID compensator (i.e. $K_p=2$, $K_i=6$, and $K_d=0.17$ with the PSD mounted on payload platform). The bode diagram was also nearly identical (not shown).

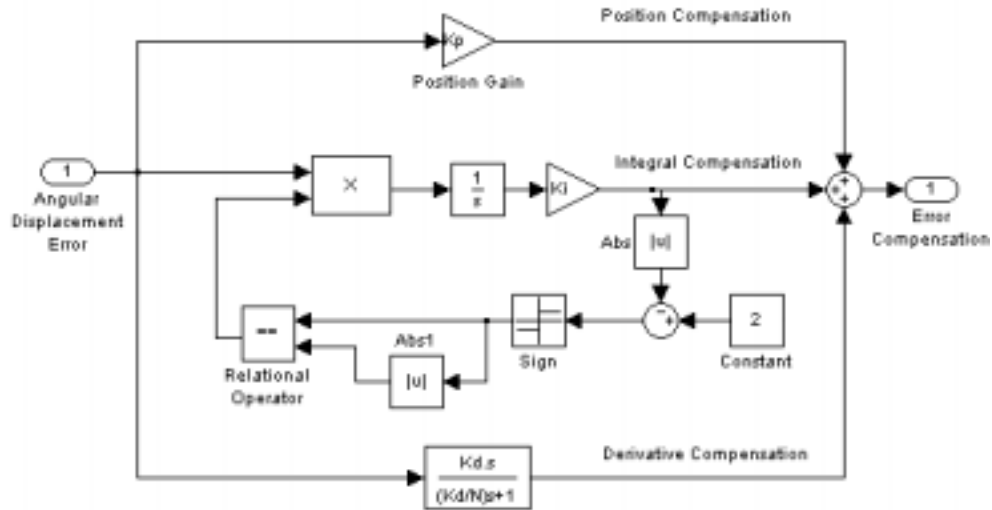


Figure 43 Modified PID Compensator Block Diagram

a. Static Pointing Results for Modified-PID Compensator

Figure 44 illustrates the differences between the standard PID controller and the modified-PID controller during static pointing. The modified-PID compensator had a slight improvement in pointing accuracy ($\pm 0.005^\circ$) over the standard PID compensator ($\pm 0.008^\circ$). Figure 45 illustrates the transient performance of the modified-PID compensator. When compared to the transient performance of the standard PID compensator (Figure 31), both compensators had nearly identical performance. The

modified PID compensator was successful in eliminating the audible high frequency noise experienced with the standard PID compensator.

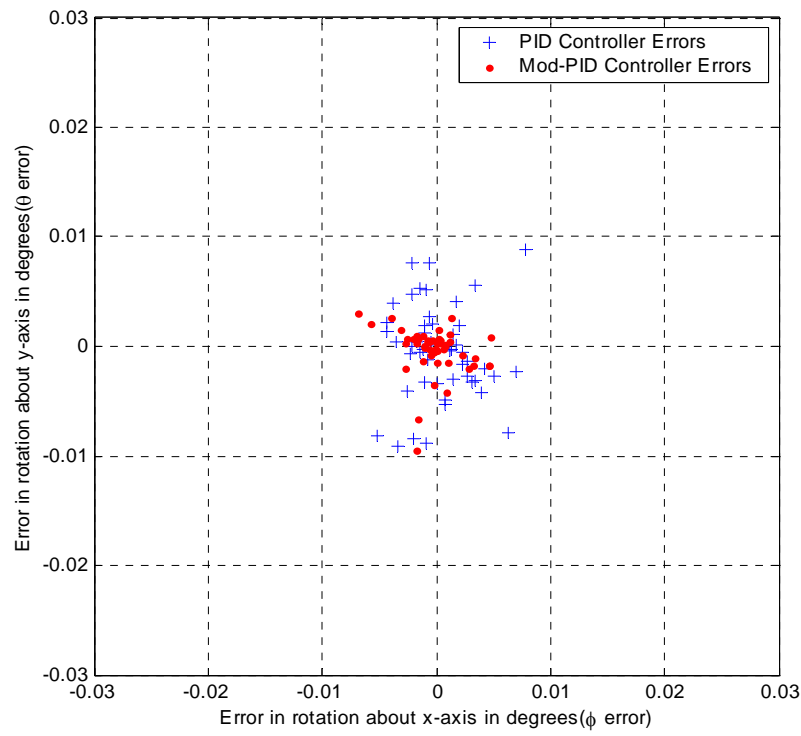


Figure 44 Comparison of ϕ and θ Errors for Static Commands Between PID and Modified PID Compensators

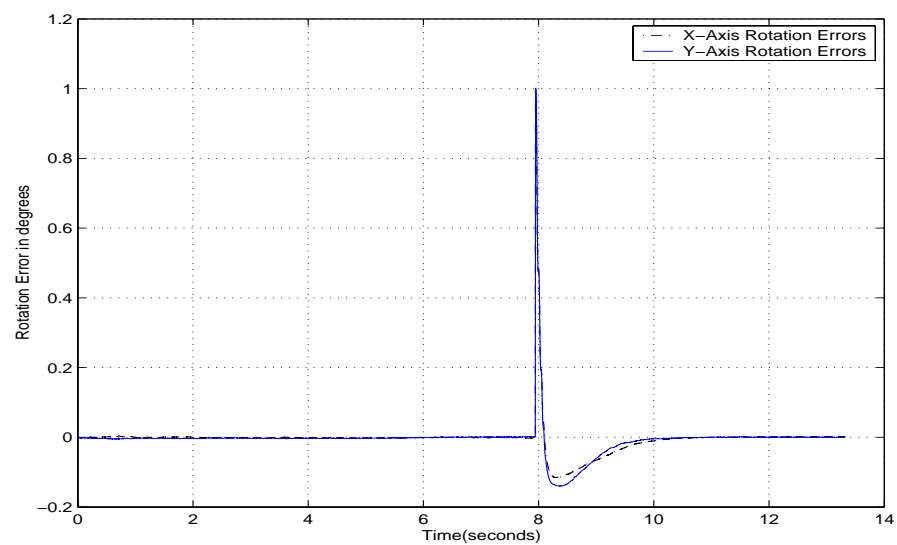


Figure 45 Modified PID Compensator Transient Performance for Simultaneous $+1^\circ$ Rotations about the x and y-axes

b. Dynamic Tracking Results for Modified PID Compensator

(1) Single Axis Tracking. The results of the single axis tracking experiments are shown in Figure 46, with Figure 47 illustrating the similarities between the modified PID and the standard PID compensators. There was not a significant difference in pointing performance between the standard and modified PID compensators; both compensators had a pointing accuracy that was less than $\pm 0.05^\circ$. Again the audible high frequency noise of the standard PID compensator was eliminated with the modified PID compensator.

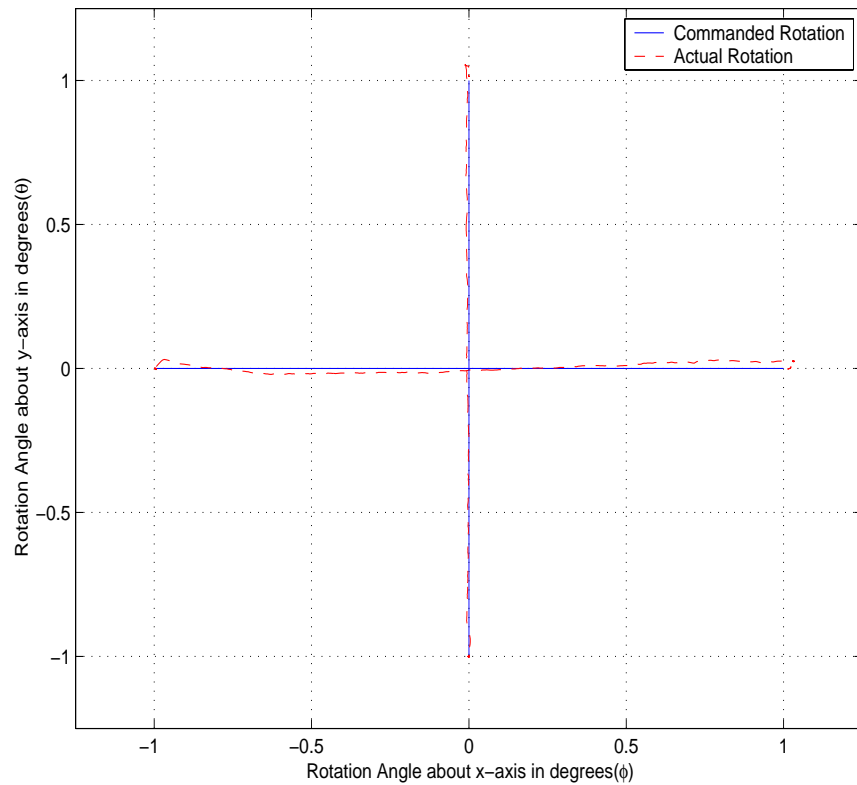


Figure 46 Commanded and Actual Trajectories for Single Axis Rotations using the Modified PID Compensator

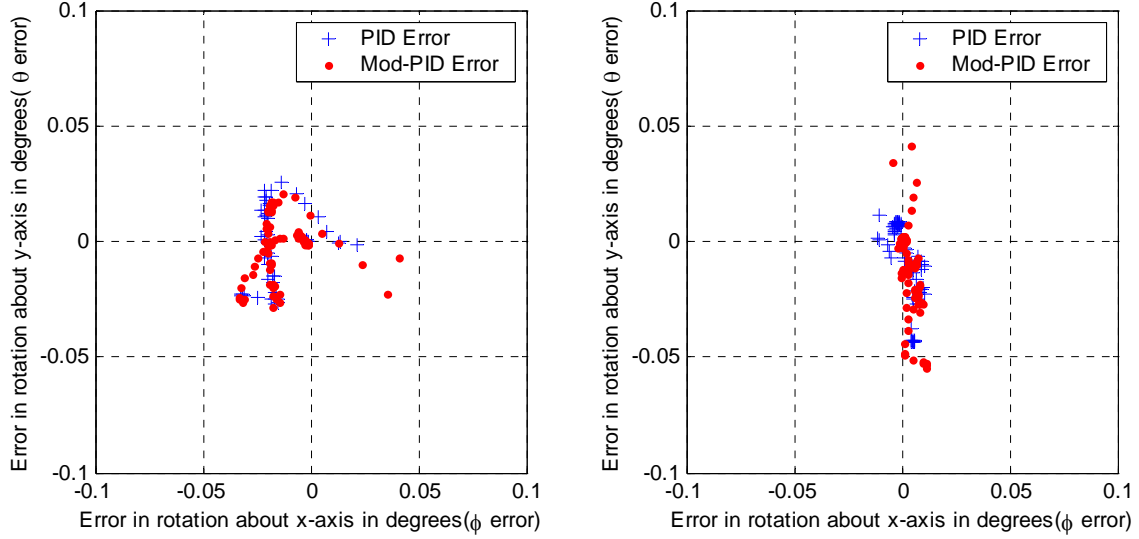


Figure 47 Differences in the ϕ and θ Errors for Single Axis Rotations of the PID and Modified PID Compensators

(2) Circular Trajectory Tracking. The circular trajectory tracking results are shown in Figure 48 through Figure 51. Figure 49 illustrates that the modified PID compensator performed almost identically to the standard PID compensator for the nominal circular trajectory ($\pm 1^\circ$ at 0.1 Hz). Comparison of Figure 48, Figure 50, and Figure 51 with the same plots for the standard PID compensator (i.e. Figure 35, Figure 38, and Figure 40) further illustrates that the performance of the modified-PID compensator was nearly identical to the standard PID compensator, however without the audible high frequency noise.

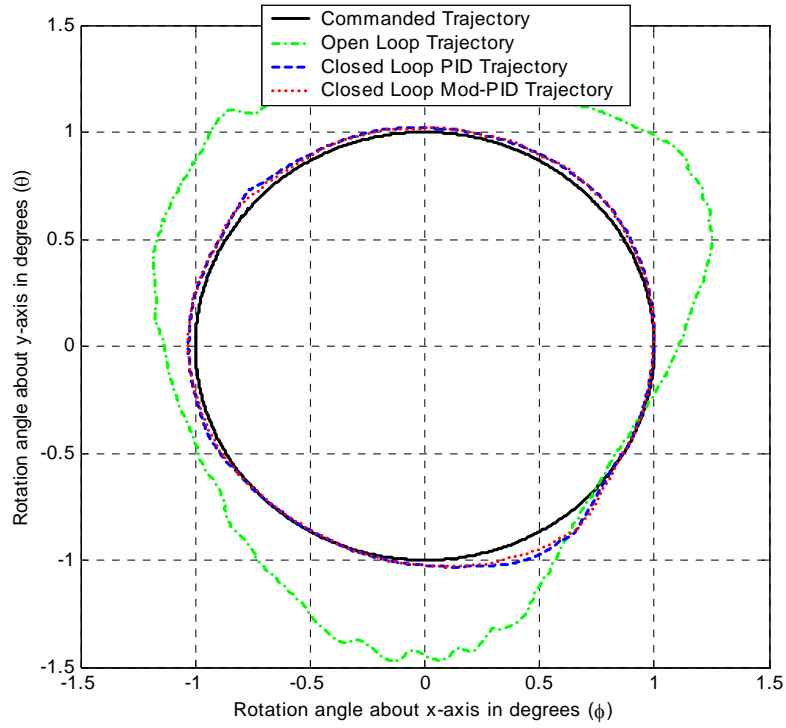


Figure 48 Comparison of the Nominal Circular Tracking Trajectories between the PID and Modified PID Compensators

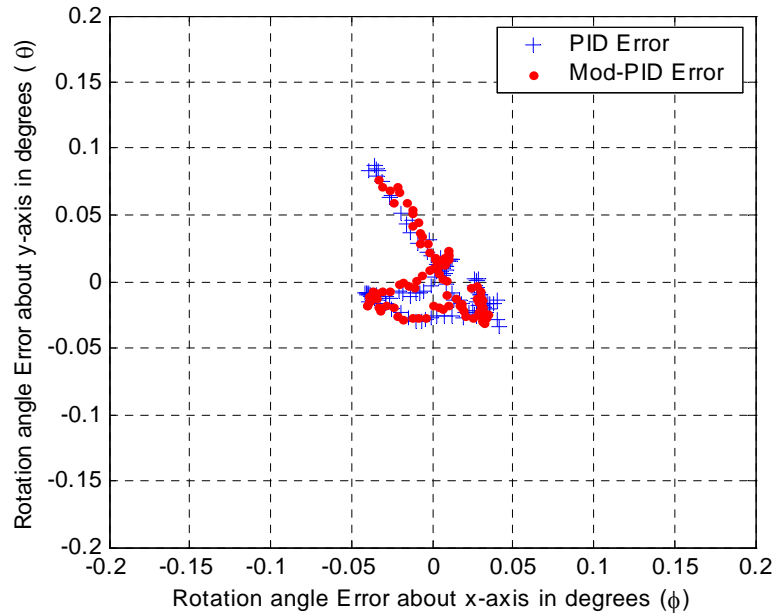


Figure 49 Comparison of ϕ and θ Errors for the Nominal Circular Tracking Trajectories between the PID and Modified PID Compensators

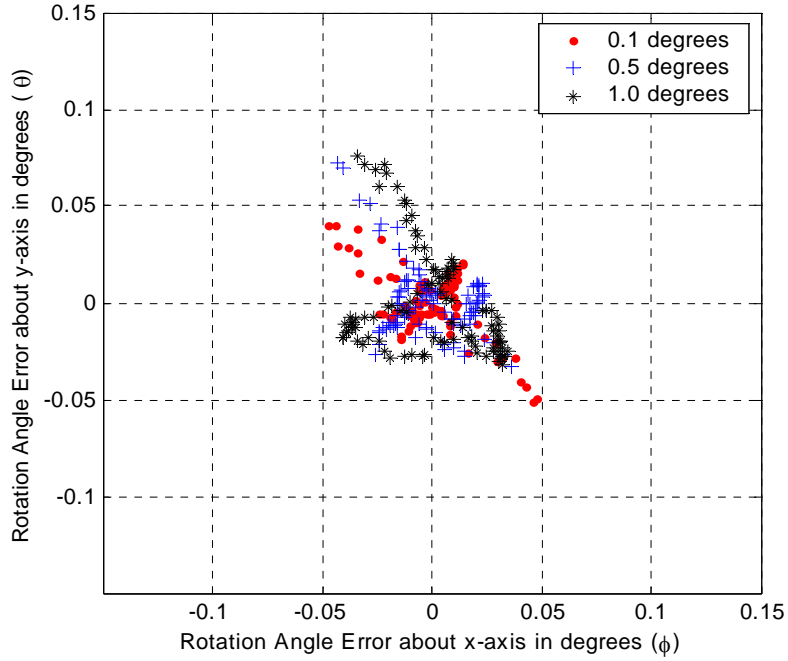


Figure 50 ϕ and θ Errors Corresponding to 0.1 Hz Circular Trajectories for Various Radii using the Modified PID Compensator

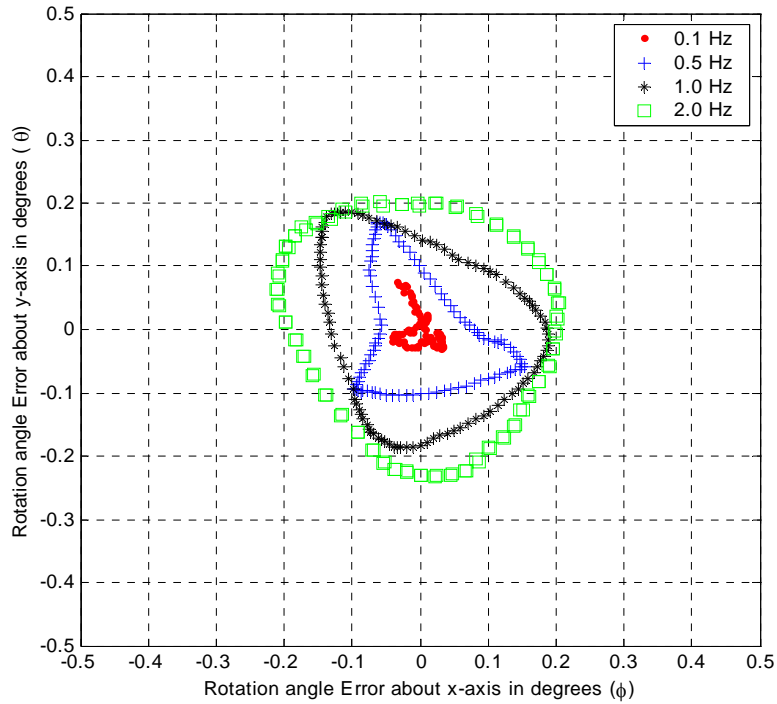


Figure 51 ϕ and θ Errors Corresponding to Clockwise, 1.0° Radius, Circular Trajectories for Various Tracking Speeds using the Modified PID Compensator

D. LARGE ANGLE CONTROLLER MODEL

1. Actuator Length Equation Implementation

The second controller implemented was the large angle controller shown in Figure 52. This controller implemented equation (5) with the PID compensators evaluated previously. For this controller it was assumed that a command of ± 0.706 volts to an actuator resulted in a change in length of ± 1 mm. This was experimentally determined based on the maximum and minimum displacements possible with ± 4 volt commands and was slightly less than that used in the small angle controller. The same evaluations conducted on the small angle controller were also conducted on the large angle controller with both the standard PID and modified PID compensators. Unfortunately, truly large angles ($>10^\circ$) were not possible due to inadequate actuator stroke length and the small angle approximations used for the Kaman position sensors. However the model was constructed and tested to prove the concept. The compensator was tuned in a similar manner to the small angle controller and the following gains were used: $K_p=4$, $K_i=6$, and $K_d=0.15$. The results between the standard PID and modified PID compensators were again nearly identical, therefore in general, only the modified PID results will be shown.

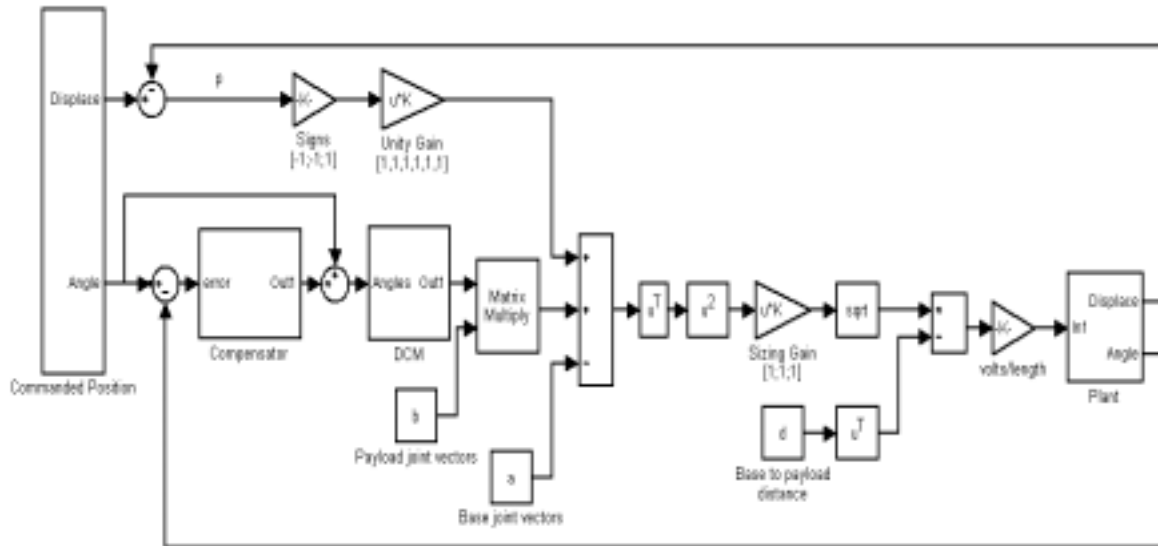


Figure 52 Large Angle Controller Block Diagram

2. Large Angle Controller Static Results

The large angle controller static pointing results are shown in Figure 53 through Figure 55. Figure 53 shows that the open loop performance of the large angle controller was similar to the small angle controller and the PID compensator significantly improved the pointing performance by two orders of magnitude (i.e. from an accuracy of $\pm 0.5^\circ$ to $\pm 0.005^\circ$). Figure 54 illustrates that the performance of the standard PID compensator and the modified PID compensator were nearly identical except for a slight ($\pm 0.003^\circ$) improvement using the modified PID compensator; a result similar to that found using the small angle controller. Figure 55 illustrates that the two compensators also have similar transient performance with a single overshoot of less than 0.2° for a 1.0° command and steady state conditions being obtained within 3 seconds of the commanded orientation. The steady state orientation of the large angle controller was 1 second longer than that obtained from the small angle controller. The primary reason for this was the necessary increase in K_p in order to obtain the proper trajectories in the large angle controller with a minimum of error, resulting in slower transient performance.

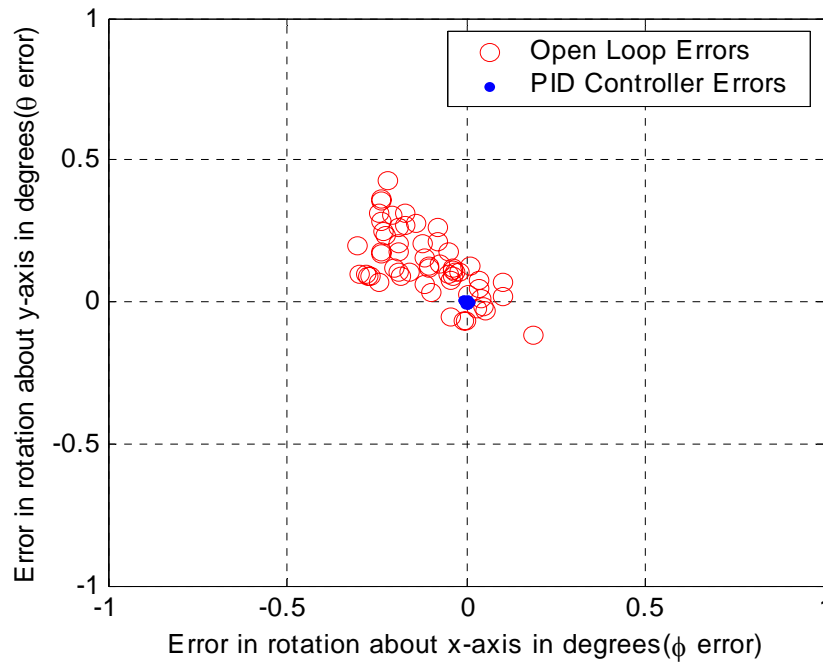


Figure 53 ϕ and θ Errors for Static Commands using the Large Angle Controller with Modified PID Compensator

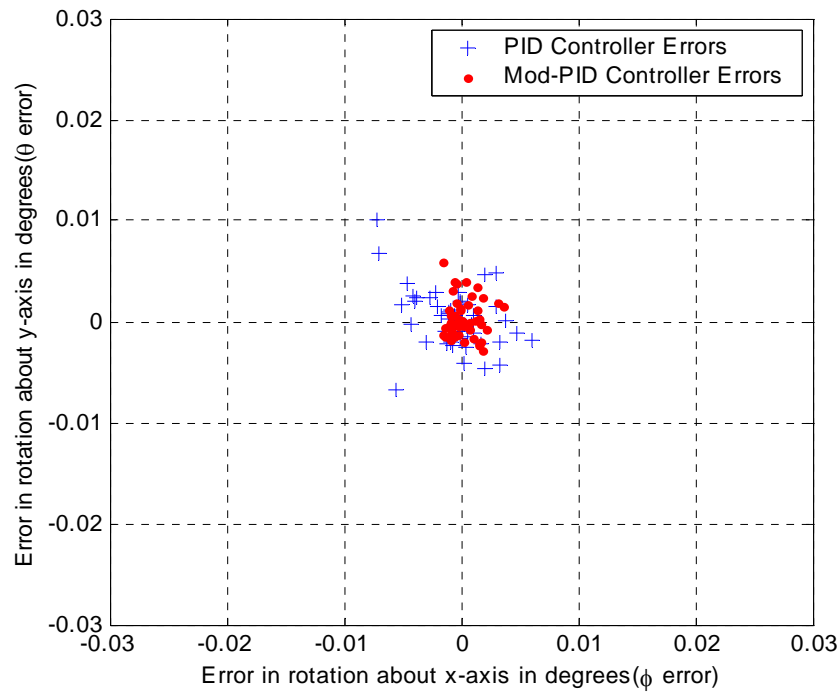


Figure 54 Comparison of the Large Angle Controller Static Errors between the PID and Modified PID Compensators

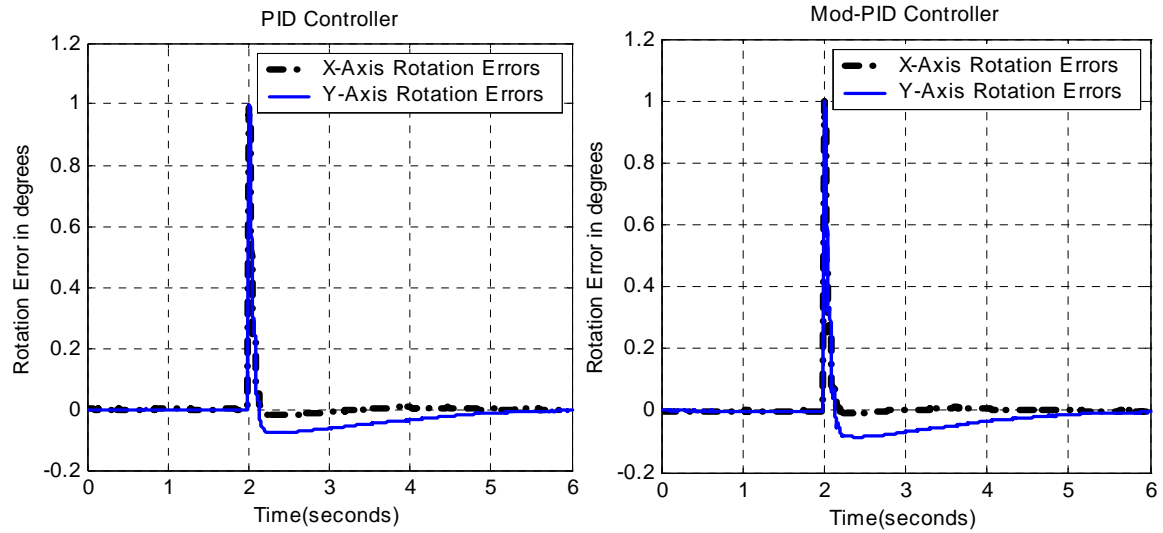


Figure 55 Large Angle Controller Transient Performance for Simultaneous $+1^\circ$ Rotations about the x and y-axes (PID vs. Mod-PID)

3. Large Angle Controller Dynamic Results

a. Single Axis Tracking

The single axis tracking results are shown in Figure 56 and Figure 57. Figure 56 shows both the open loop and the closed loop performance with the modified PID compensator. The large error in the y-axis rotations at the start of the rotation (circled region on Figure 56) was a consistent phenomenon and was probably a result of static friction in at least one actuator. Figure 57 shows that pointing accuracy using the modified PID compensator improved from more than $\pm 0.6^\circ$ down to $\pm 0.05^\circ$ with one excursion to greater than $\pm 0.1^\circ$ again possibly due to the static friction encountered at the start of the y-axis rotation.

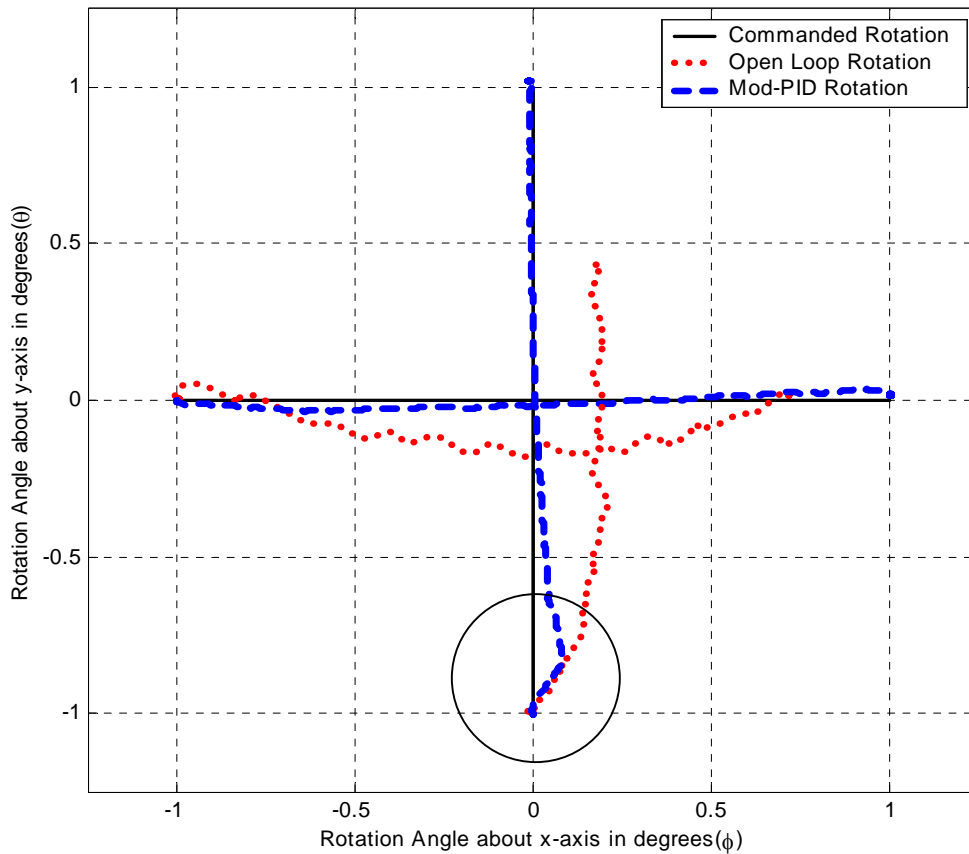


Figure 56 Large Angle Controller ϕ and θ Commanded and Actual Trajectories for Single Axis Rotations

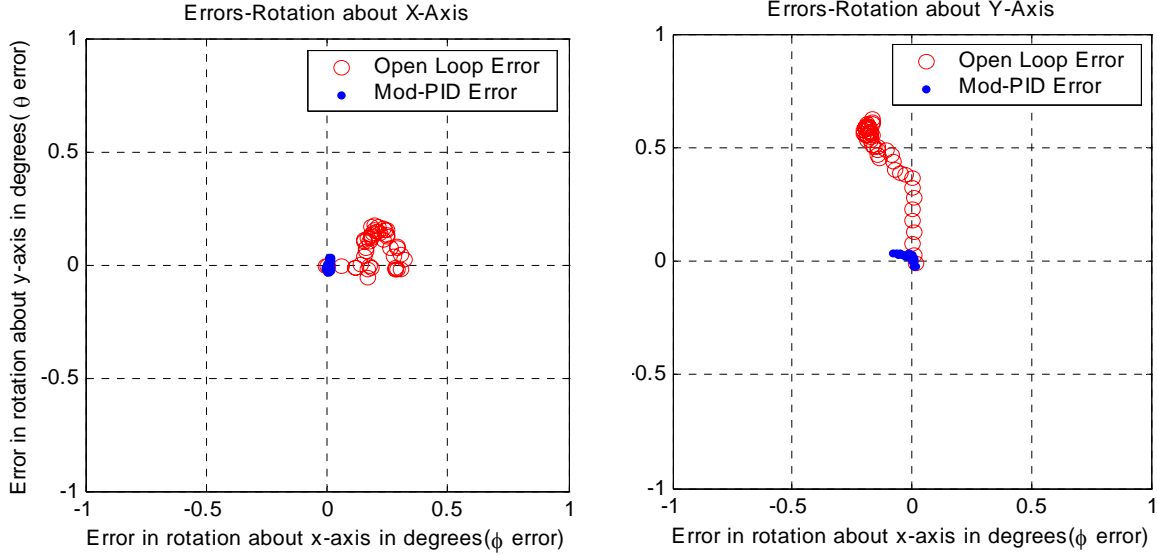


Figure 57 Large Angle Controller ϕ and θ Errors for Single Axis Rotations

b. Circular Trajectory Tracking

The circular trajectory tracking results of the large angle controller are shown in Figure 58 through Figure 61. Figure 58 shows the nominal trajectories (1° radius at 0.1 Hz) for the open loop and closed loop controllers. The main difference between the response of the small angle controller and the large angle controller was that the open loop trajectory was generally less than the commanded trajectory for the large angle controller, while the open loop trajectory was generally greater than the commanded trajectory for the small angle controller. In other words, the tracking errors between the two controllers had opposite signs. This was probably a result of the differences between the gains used in the small and large angle controller to convert volts to actuator displacement. The small angle controller used ± 1 volt/mm while the large angle controller used a smaller value of ± 0.706 volts/mm, resulting in the differences in open loop trajectories. While this gain certainly affects open loop performance, the use of a properly tuned PID compensator corrects for any such conversion error. Figure 59 illustrates this fact showing that the modified PID compensator could bring pointing errors to $\pm 0.06^\circ$ of the commanded trajectory. This was similar to that achieved with the small angle controller (Figure 49).

This controller also behaved in a similar manner to the small angle controller with regards to varying the circle radius (Figure 60) and circle tracking speed (Figure 61). Radius size had little effect on the size of the pointing error at 0.1 Hz; the pointing error remained less than $\pm 0.08^\circ$ regardless of the circle size. Additionally, circular tracking speed was a significant factor in the magnitude of the pointing error as it was in the small angle controller, ranging from $\pm 0.05^\circ$ for 0.1 Hz up to $\pm 0.2^\circ$ for 2 Hz circles.

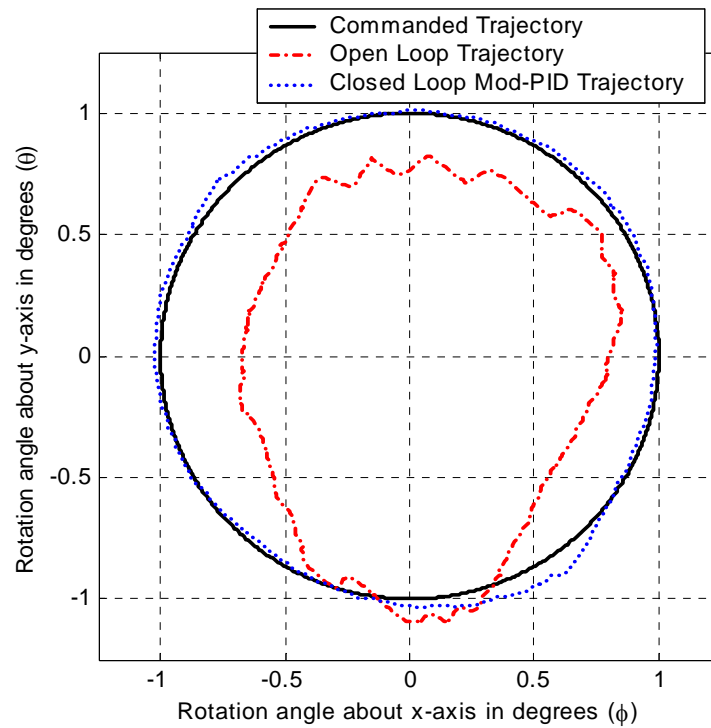


Figure 58 Large Angle Controller Nominal Circular Tracking Trajectory ($\pm 1^\circ$ at 0.1 Hz)

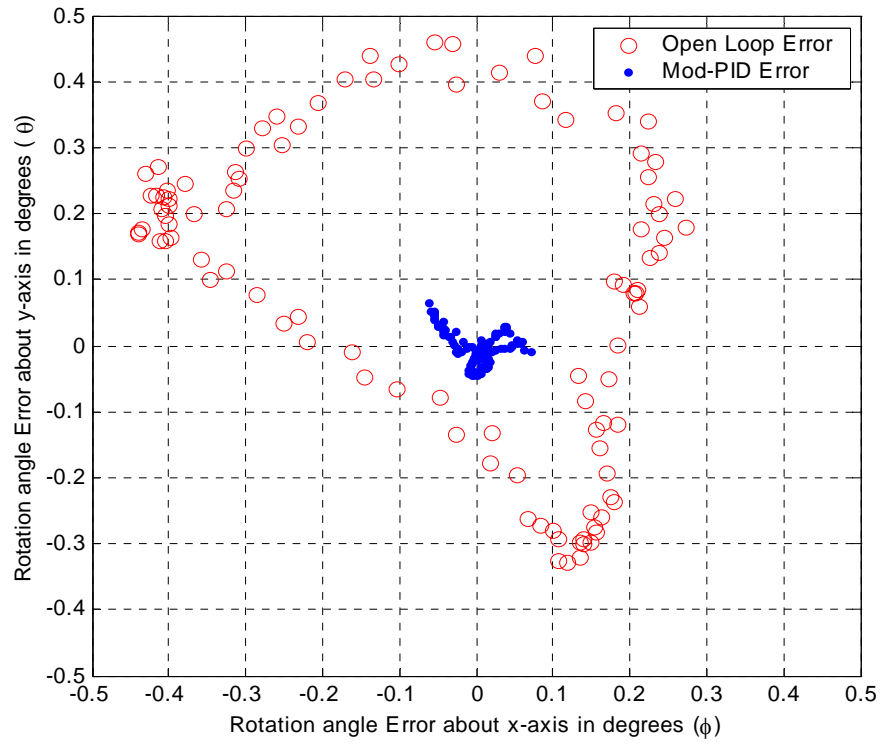


Figure 59 Large Angle Controller ϕ and θ Errors for Nominal Circular Trajectory

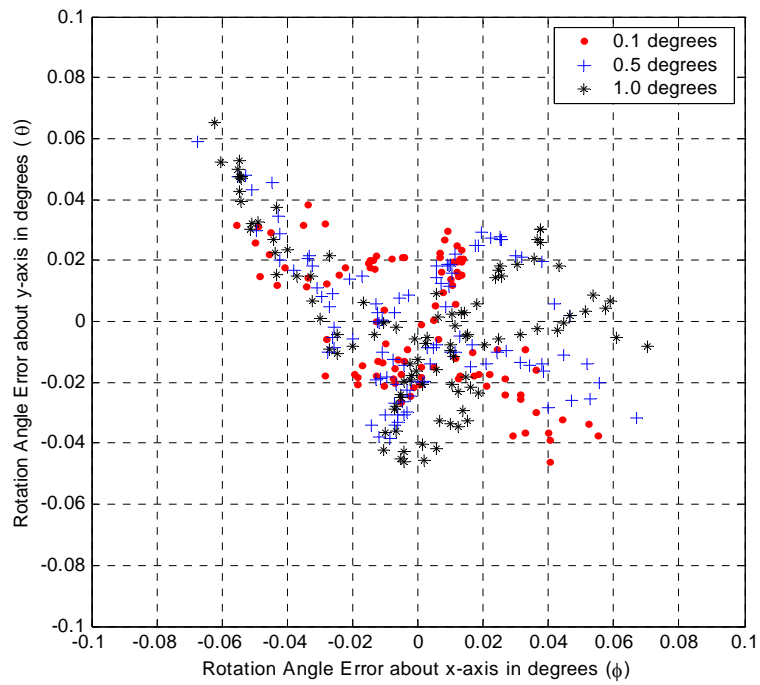


Figure 60 Large Angle Controller ϕ and θ Errors Corresponding to 0.1 Hz Circular Trajectories for Various Radii

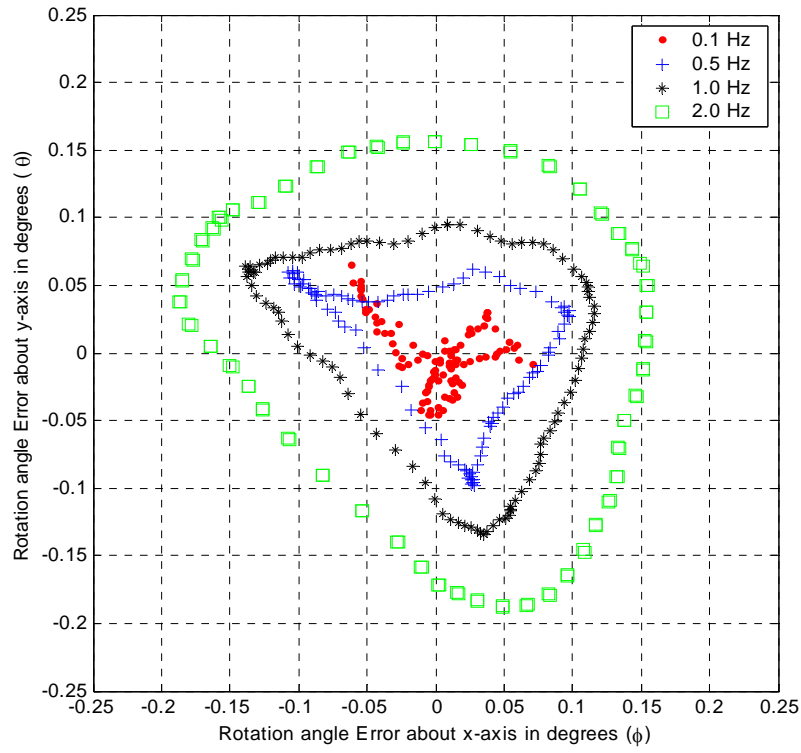


Figure 61 Large Angle Controller ϕ and θ Errors Corresponding to Clockwise, 1.0° Radius, Circular Trajectories for Various Tracking Speeds

THIS PAGE INTENTIONALLY LEFT BLANK

V. PRECISION POINTING CONTROLLER WITH VIBRATION SUPPRESSION EXPERIMENTAL RESULTS

A. SCOPE AND SETUP

The scope of the combined vibration suppression and precision pointing experiments was to evaluate the pointing accuracy and vibration suppression capability of the PPH in the presence of a single tone disturbance, while using the small angle controller with the standard PID compensator and the adaptive disturbance canceller (ADC). A 40 Hz disturbance was used as an example throughout this thesis to demonstrate the implementation. This evaluation was conducted for static poses (fixed orientation) and for dynamic circular tracking trajectories.

Before this evaluation could be conducted, several preliminary experiments were conducted. First, the ambient noise of the PPH was taken from the strut-mounted accelerometers with the PID compensator on and off to baseline the system noise level. This was done at the nominal payload platform orientation. Next the vibration environment for each of the fixed orientation and dynamic circular tracking trajectories was baselined with the PID compensator on but without any additional disturbances. The frequency range of the data was restricted by the accelerometers to a bandwidth of 200 Hz, however this was sufficient to demonstrate active vibration suppression. Then the performance of the PPH in the presence of a single tone disturbance was evaluated both for pointing accuracy and for ensuring the stability of the PID compensator in the presence of the disturbance. Finally, ADC performance was verified for the nominal payload pose (i.e. no tip/tilt/twist/translation) and the learning factors, μ , for the disturbance tone (40 Hz) and its first two harmonics (80 Hz and 120 Hz) were determined. Following these experiments, the static and dynamic tasks were evaluated.

For the static orientation evaluations, the payload platform was oriented in the four combinations of $\pm 1.0^\circ$ rotations about the x and y-axes simultaneously (i.e. $+1.0^\circ$ about the x-axis and $+1.0^\circ$ about the y-axis, -1.0° about the x-axis and $+1.0^\circ$ about the y-axis, etc). The orientation remained fixed during each experiment for at least 10 seconds prior to recording data, then for an additional 10 seconds during recording of the data.

The pointing accuracy and vibration suppression were evaluated with and without the ADC operating.

The dynamic performance experiments used circular trajectories of 2 different speeds (0.1 Hz and 2 Hz) and a variety of different radii (0.1°, 0.5°, and 1.0°) to evaluate both pointing accuracy and vibration suppression capability. Performance with and without the ADC operating was recorded over a period of 10 seconds after the controller had been operating for at least 10 seconds prior.

For all experiments, the Aura Bass Shaker was mounted on the payload platform in place of the PSD laser module and mounting bracket. The single tone (40 Hz) disturbance level was set at -5 dB (0.1 g²/Hz) referenced to 1 g measured at nominal static conditions and remained the same throughout all of the experiments. This was the maximum disturbance level obtainable with this equipment. All accelerometer data was passed through a high pass filter in Simulink (corner frequency = 2 Hz or 12.56 rad/sec) before being used by the ADC. For illustration purposes, all referenced noise measurements were taken directly from the accelerometer mounted on the number 4 actuator (i.e. without any filtering or post-processing), although all six accelerometers were used for the ADC. Finally, due to the change in payload mass, the standard compensator was tuned again as in Chapter IV, and the following gains were found: $K_p=3.5$, $K_i=6$, and $K_d=0.26$.

B. POINTING CONTROLLER PERFORMANCE WITH SINGLE TONE (40 HZ) DISTURBANCE

The ambient noise environment of the nominal system with and without the standard PID compensator operating was sampled and shown in Figure 62. In general, the ambient noise environment was at -60dB (0.0121 g_{rms}) with the compensator off and was slightly higher with the compensator operating (-56 dB or 0.0154 g_{rms}). In both instances, there was an obvious ambient disturbance at 120 Hz, which was seen throughout the experiments. The power spectral densities for the ambient noise environment of each orientation and dynamic tracking trajectory to be evaluated were similar to Figure 62 and therefore not shown. Table 10 summarizes the ambient noise environment in g_{rms} for each of those orientations and trajectories. In general, the g_{rms} of

the ambient noise environment increased as the trajectory increased in radius or in speed, as would be expected due to the increased motion of the actuators.

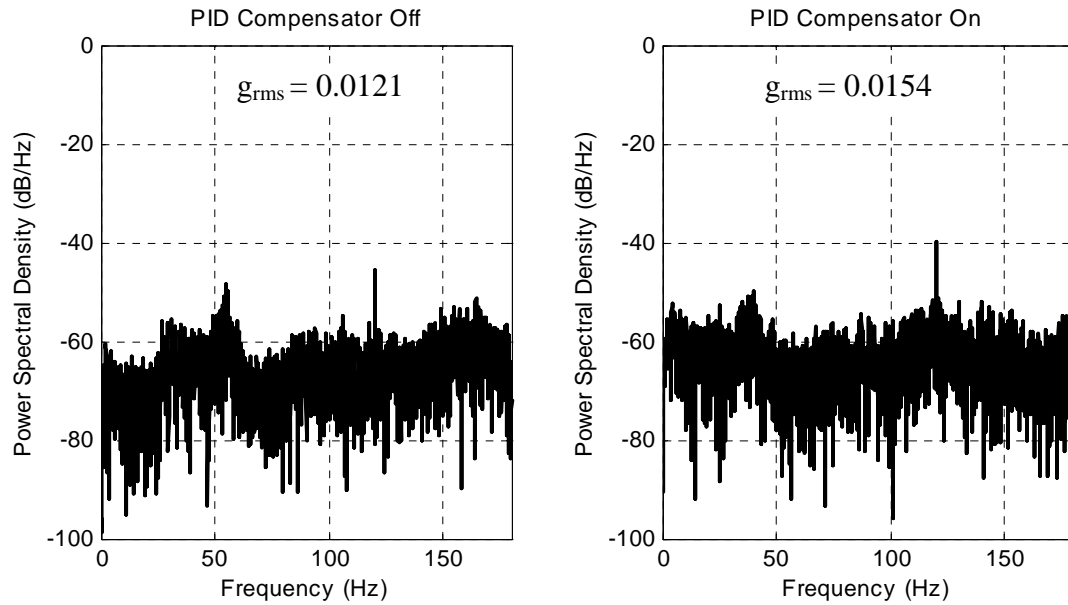


Figure 62 Ambient Noise Power Spectral Density

Table 10 Ambient Noise Environment Baseline for Fixed Orientation and Dynamic Tracking Trajectories without Disturbance

Orientation/Trajectory	g_{rms}
Static Orientations	
Nominal without PID Compensator	0.0121 g_{rms}
Nominal with PID Compensator	0.0154 g_{rms}
+1° about x-axis and -1° about y-axis with PID Compensator	0.0144 g_{rms}
Dynamic Tracking Orientations	
Circular Trajectory with 0.1° radius at 0.1 Hz	0.0226 g_{rms}
Circular Trajectory with 0.5° radius at 0.1 Hz	0.0275 g_{rms}
Circular Trajectory with 1.0° radius at 0.1 Hz (Nominal Dynamic Tracking Trajectory)	0.0466 g_{rms}
Circular Trajectory with 0.1° radius at 2.0 Hz	0.0344 g_{rms}
Circular Trajectory with 0.5° radius at 2.0 Hz	0.0495 g_{rms}
Circular Trajectory with 1.0° radius at 2.0 Hz	0.0726 g_{rms}

Applying a single tone disturbance of 40 Hz to the PPH resulted in the power spectral density shown in Figure 63. The harmonics at 80 Hz, 120 Hz, and 160 Hz were clearly apparent. Figure 64 illustrates the corresponding pointing accuracy performance. Without the disturbance, the pointing accuracy was $\pm 0.006^\circ$. Surprisingly, the pointing accuracy improved to $\pm 0.002^\circ$ with the disturbance. Presumably this improvement in pointing accuracy was due to the reduction in static friction of the actuator bushings as a result of the disturbance. The pointing accuracies achieved with the shaker mounted on the payload platform were consistent with the accuracies obtained in Chapter IV with the PSD mounted on the payload platform. Experiments also showed that the standard and modified PID compensators remained stable in the presence of single and multiple tone disturbances (10-100 Hz) for power spectral density magnitudes up to -5dB (0.1 g^2/Hz) for each disturbance.

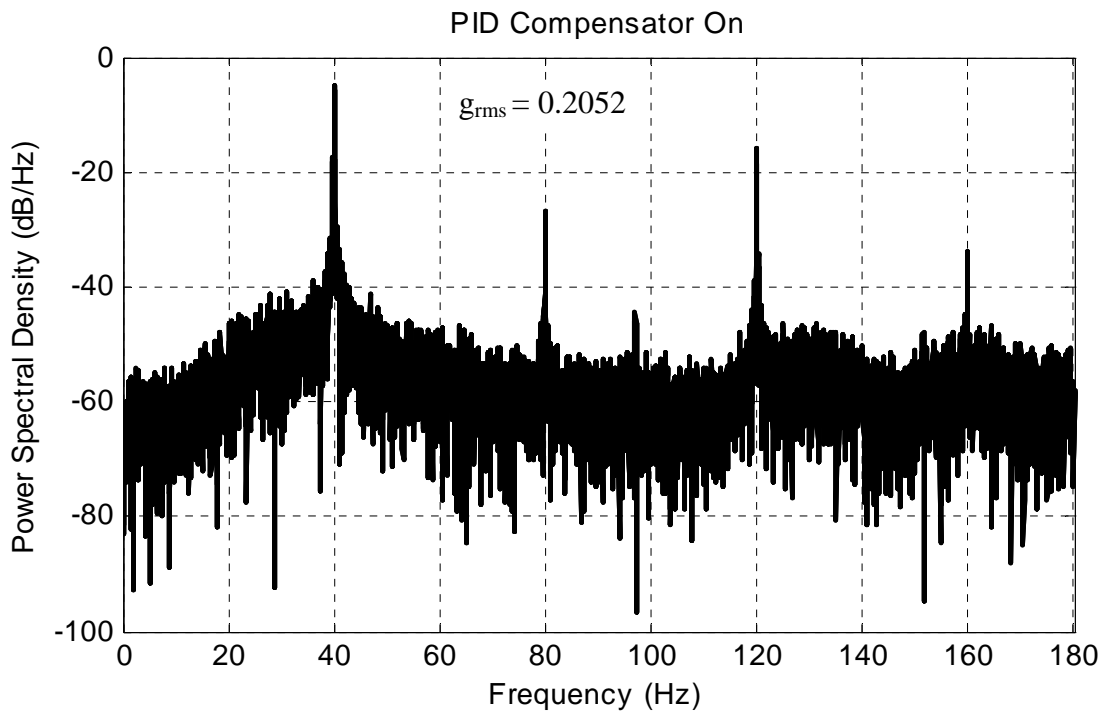


Figure 63 Power Spectral Density of the System Response to a Single Tone (40 Hz) Disturbance

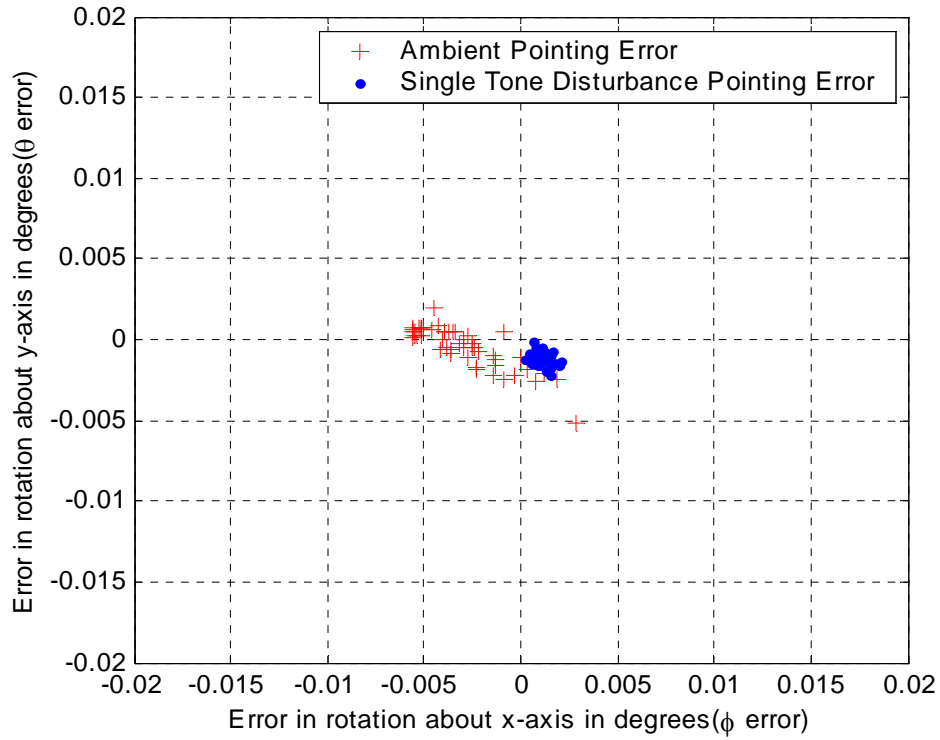


Figure 64 Pointing Error at the Nominal Payload Orientation with a Single Tone (40 Hz) Disturbance

C. BASELINE VIBRATION SUPPRESSION PERFORMANCE OF THE ADAPTIVE DISTURBANCE CANCELLER

With the pointing controller verified stable in the presence of a payload disturbance, the adaptive disturbance canceller (ADC) was incorporated into the pointing algorithm as seen in the simplified block diagram shown in Figure 65. Figure 66 illustrates the baseline performance of the ADC and verifies that the new combined pointing and vibration suppression model works and the ADC performed as expected. With cancellation on, there was a reduction in the g_{rms} by a factor of 6.5. The fundamental disturbance frequency (40 Hz) and the first harmonic (80 Hz) were attenuated to the noise floor, while the second harmonic at 120 Hz was attenuated to its ambient power spectral density of -40 dB. The third harmonic at 160 Hz, which was not suppressed by the ADC, became the dominant disturbance frequency with the ADC on. This was typical of past ADC performance, in that the energy from the lower frequencies being suppressed was transferred to the higher frequency harmonics.

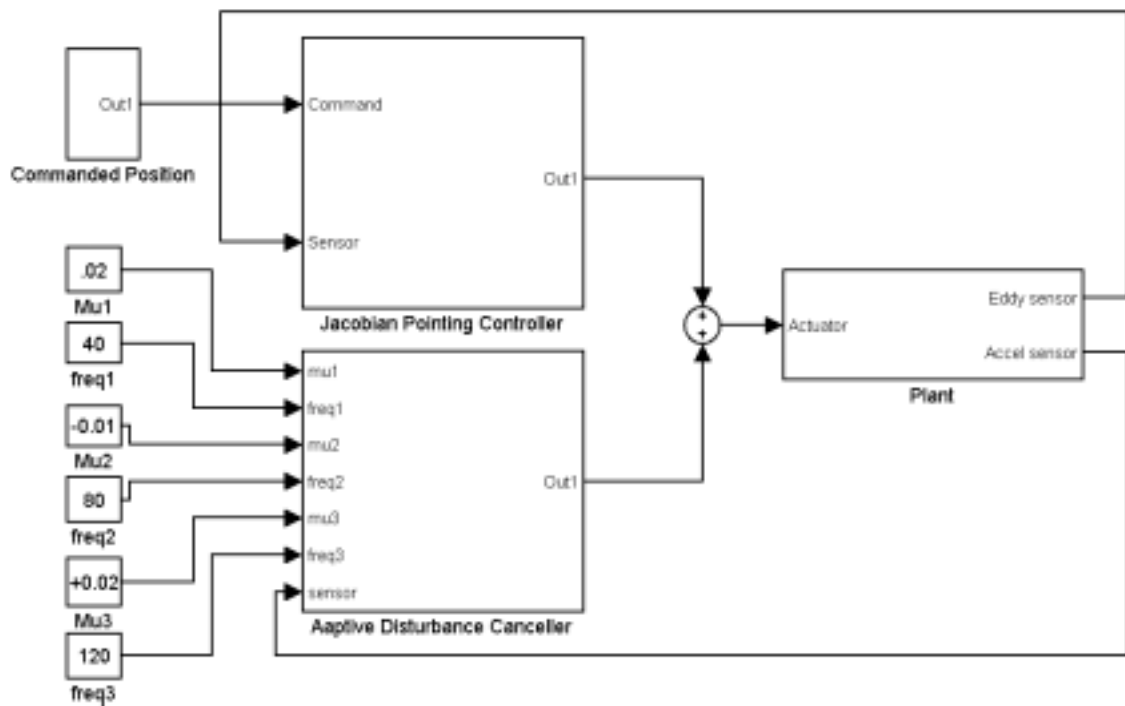


Figure 65 Combined Vibration Suppression and Pointing Controller (Simplified)

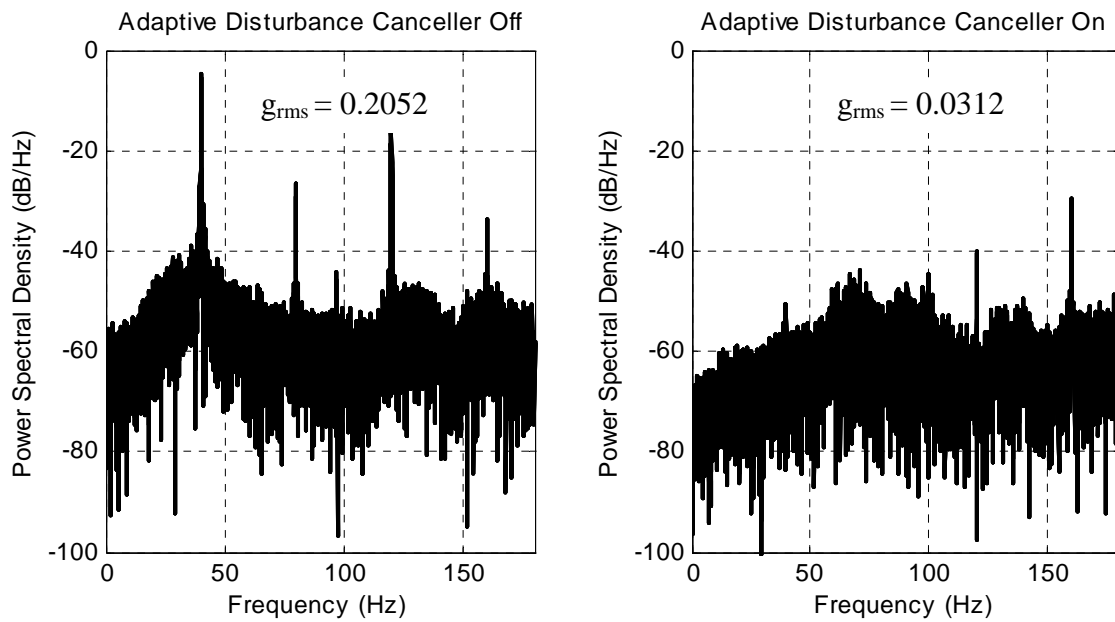


Figure 66 Adaptive Disturbance Canceller Baseline Performance

D. COMBINED VIBRATION SUPPRESSION AND PRECISION POINTING RESULTS

1. Static Pointing Performance

The static pointing performance results of the combined vibration suppression and pointing model are shown in Figure 67 and Figure 68. Figure 67 illustrates that even at orientations that were significantly off of the nominal ($+1^\circ$ about the x-axis and -1° about the y-axis shown) the ADC performed just as it did for the nominal baseline case (Figure 66). This was the case for all of the combinations of $\pm 1.0^\circ$ about the x and y-axes. In particular, g_{rms} was reduced by at least a factor of 2.5 (a factor of 3.5 is illustrated), and the fundamental frequency and first harmonic were suppressed to the noise floor, while the second harmonic at 120 Hz was suppressed to the ambient level. Figure 68 illustrates that the pointing accuracy with a disturbance (both cancelled and uncanceled) was improved over the disturbance-free pointing accuracy (accuracy went from $\pm 0.005^\circ$ to $\pm 0.002^\circ$), again, as was the case for the nominal pointing accuracy with a disturbance, presumably due to the reduction in actuator static friction. This pointing accuracy and that from the nominal orientation, represented the best seen throughout this research.

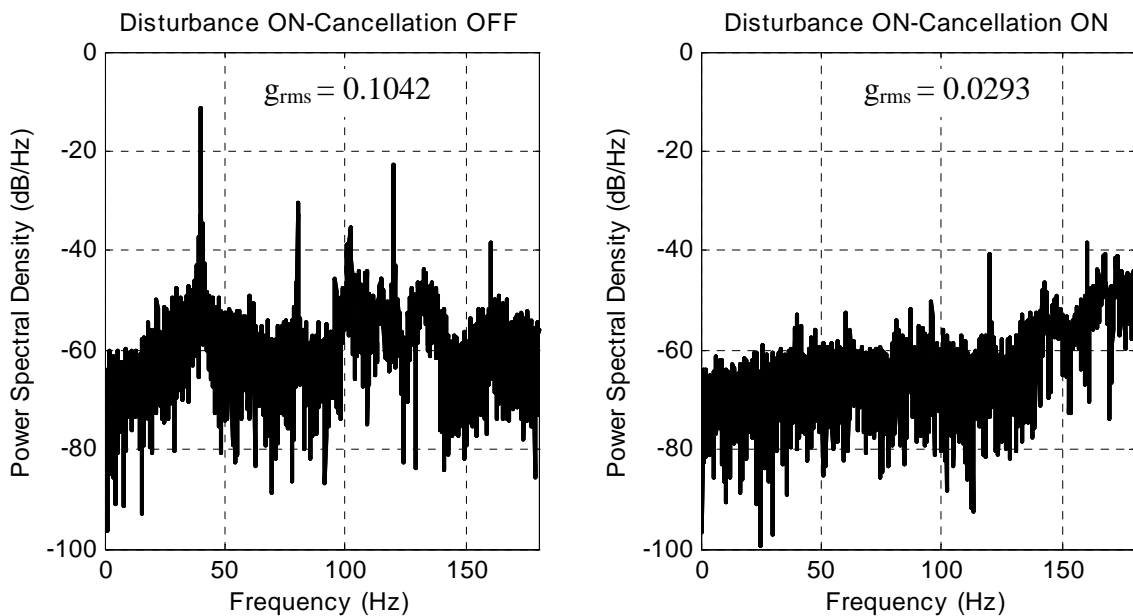


Figure 67 Power Spectral Density of the System Response to a Single Tone Disturbance (40 Hz) at an Orientation of $+1^\circ$ about the x-axis and -1° about the y-axis.

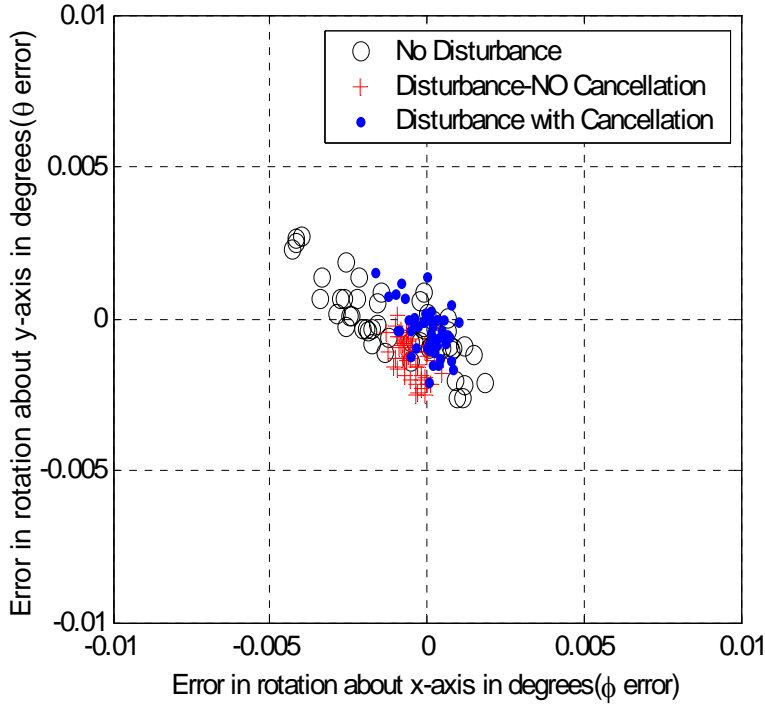


Figure 68 Pointing Error with a Single Tone Disturbance (40 Hz) at a Pose of $+1^\circ$ about the x-axis and -1° about the y-axis

2. Vibration Suppression Dynamic Tracking Performance (Circle Trajectory)

a. 0.1 Hz Circle Trajectory

The vibration suppression performance of the ADC during dynamic tracking tasks was first evaluated using the slow circular trajectory (0.1 Hz) at a variety of radii. Figure 69 through Figure 71 illustrate the results. Figure 69 illustrates that at the small radius (0.1°) and slow speed (0.1 Hz) the ADC performed reasonably well. There was a reduction in the g_{rms} from 0.0718 down to 0.0251, and at the fundamental disturbance frequency vibrations were suppressed by 25 dB, nearly to the noise floor. Vibrations at the second and third harmonic were suppressed to ambient levels. Figure 70 and Figure 71 reveal similar results at the larger radii. Specifically, the ADC was capable of reducing the g_{rms} by at least a factor of 2.7, nearly down to the baseline environment. Suppression of the primary disturbance by at least 20 dB and the second

harmonic (120 Hz) to nearly the ambient conditions was also achieved in all cases. The suppression of the first harmonic (80 Hz), degraded at radii larger than 0.5° , resulting in a disturbance level of approximately -40dB with the ADC active. Interestingly, when the first harmonic was not completely suppressed, the third harmonic did not have a strong presence since the disturbance energy was distributed in the lower harmonics.

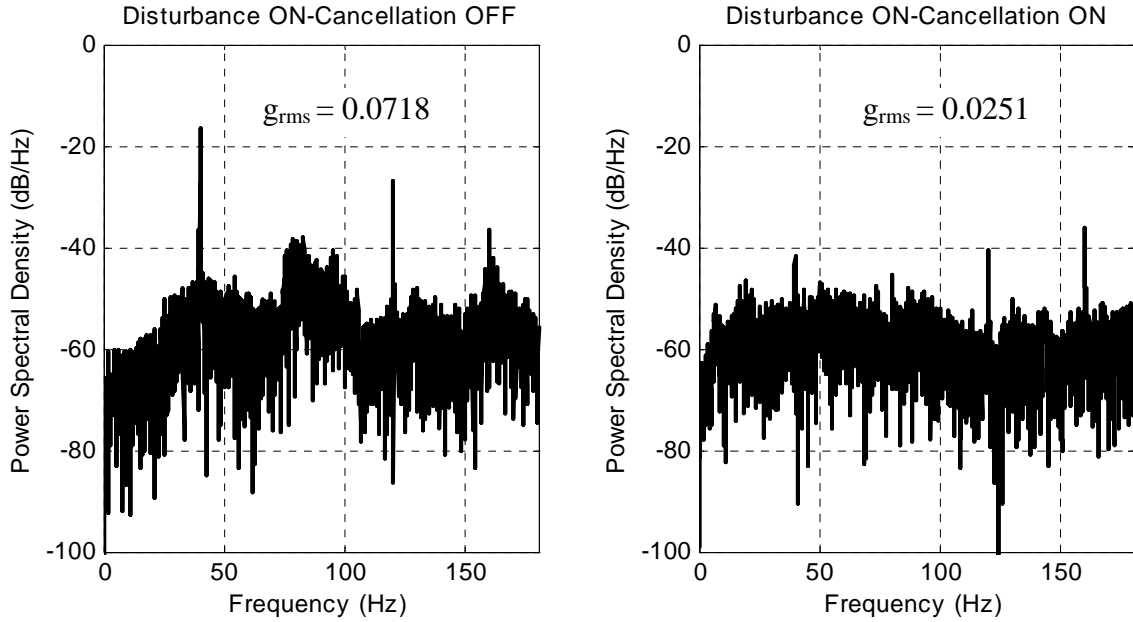


Figure 69 Performance of ADC with a 0.1° Radius Circular Trajectory at 0.1 Hz

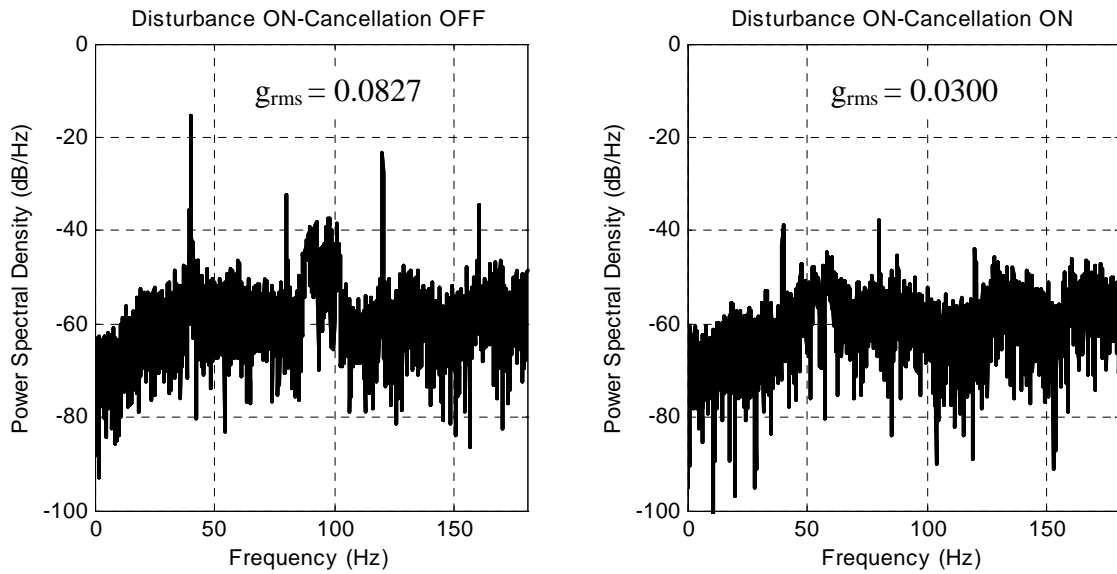


Figure 70 Performance of ADC with a 0.5° Radius Circular Trajectory at 0.1 Hz

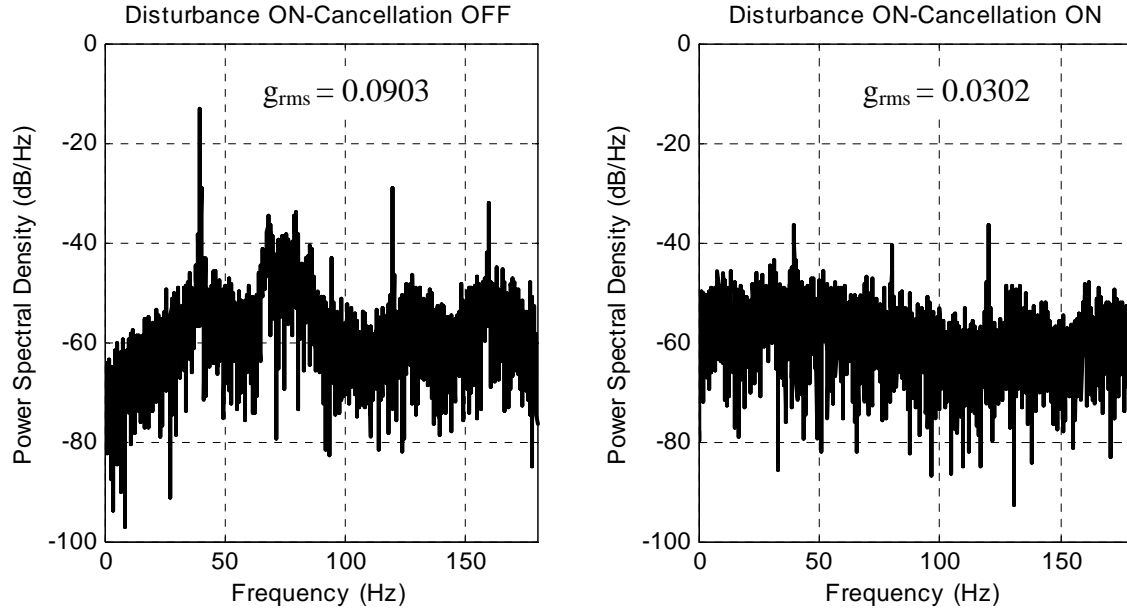


Figure 71 Performance of ADC with a 1.0° Radius Circular Trajectory at 0.1 Hz

b. 2 Hz Circle Trajectory

The vibration suppression performance of the ADC was then evaluated using the fast circular trajectory (2.0 Hz) at a variety of radii. The results for the fast circle trajectories at 2 Hz are shown in Figure 72 through Figure 74. All of these results show a presence of a 2 Hz disturbance (with harmonics) associated with the speed of the circle trajectory. As was the case for the 0.1 Hz trajectories, there was a suppression of the fundamental disturbance frequency by at least 20 dB. The first harmonic (80 Hz) for the smaller radius trajectories, was clearly present with the ADC off, and modest suppression was achieved (~5 dB) with a 0.1° radius trajectory. As the circle radius got bigger however, the disturbance harmonics were not present either with the ADC on or off and the noise floor increased approximately 5 dB (1.0° trajectory) when compared to the 0.1 Hz circle trajectories. The g_{rms} was reduced by at least a factor of two in all cases with the ADC on, resulting in a noise environment that was just slightly greater than the ambient baseline environment.

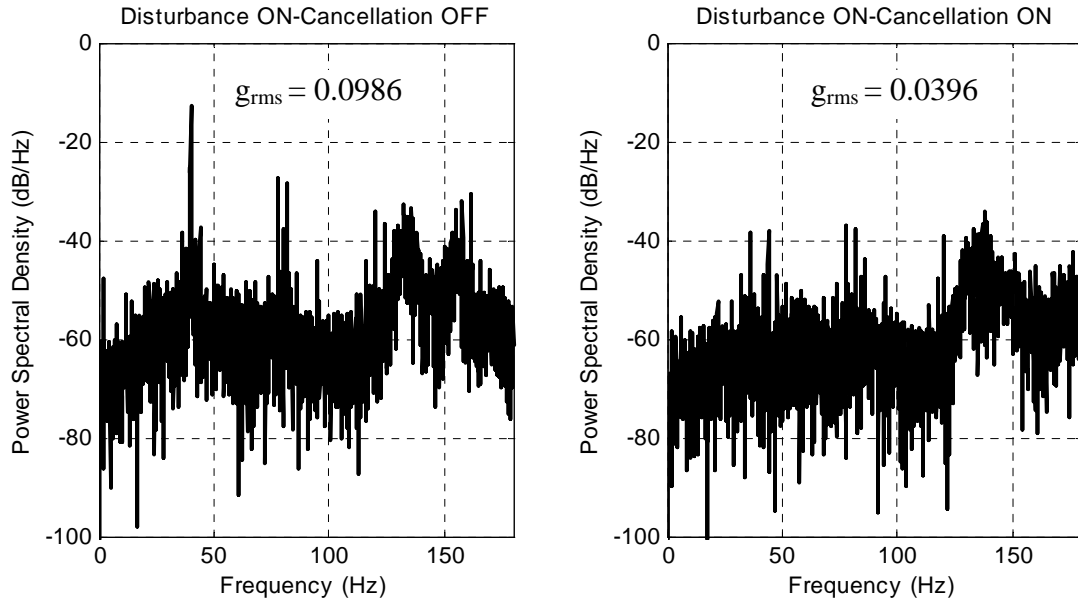


Figure 72 Performance of ADC with a 0.1° Radius Circular Trajectory at 2.0 Hz

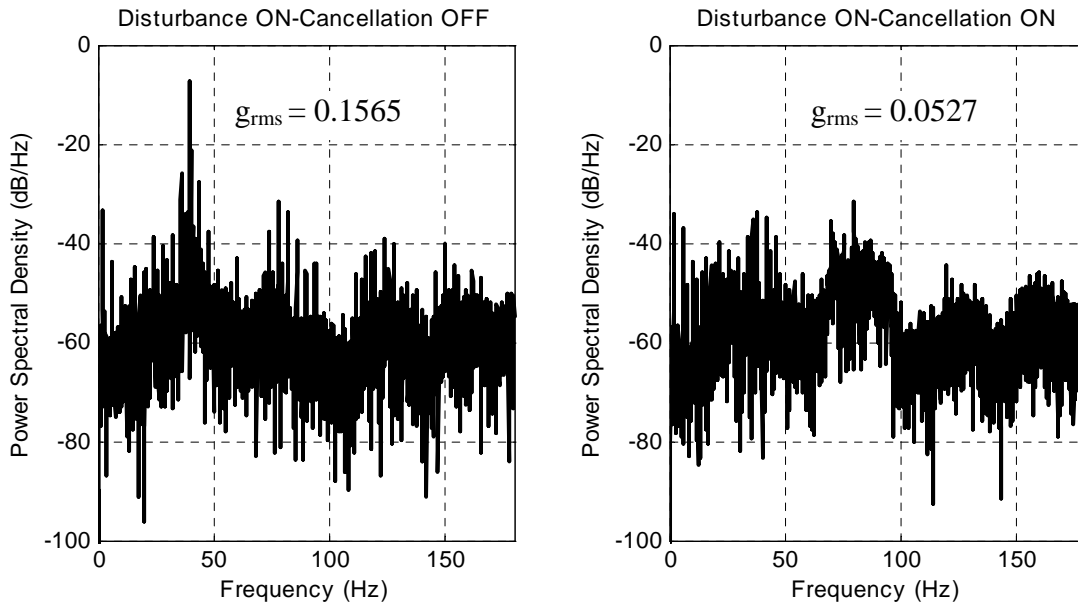


Figure 73 Performance of ADC with a 0.5° Radius Circular Trajectory at 2.0 Hz

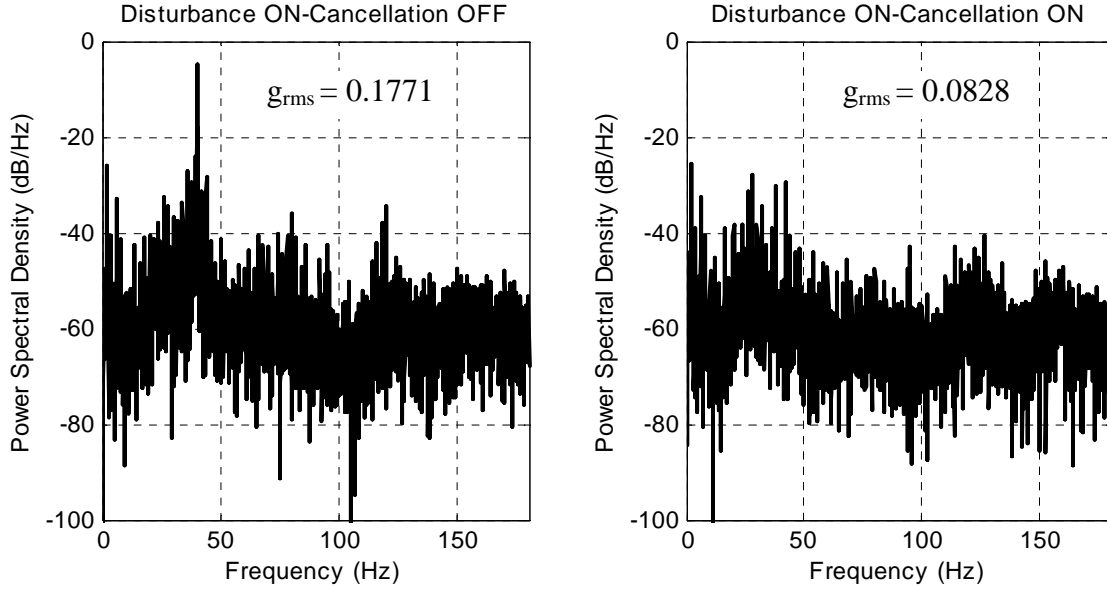


Figure 74 Performance of ADC with a 1.0° Radius Circular Trajectory at 2.0 Hz

3. Precision Pointing Dynamic Tracking Performance (Circular Trajectory)

The dynamic performance of the pointing controller (small angle controller with standard PID compensator) was evaluated for pointing accuracy at both the slow (0.1 Hz) and fast (2.0 Hz) circular trajectories at a variety of radii. The results are illustrated in Figure 75 through Figure 78.

a. 0.1 Hz Circle Trajectory

Figure 75 illustrates an improvement in pointing accuracy with the disturbance, both with and without vibration cancellation, similar to what was seen in the static performance experiments. Pointing accuracy improved from $\pm 0.03^\circ$ to $\pm 0.01^\circ$ with the disturbance for this case, and like the static case, there was not a significant difference in pointing accuracy depending on whether or not the ADC was on or not. As the circle trajectories got bigger, the improvements noticed in pointing accuracy began to diminish and were equivalent to the disturbance-free case at the 1.0° radius trajectory as seen in Figure 76. In all cases tested, the pointing performance never degraded to worse than the disturbance-free case.

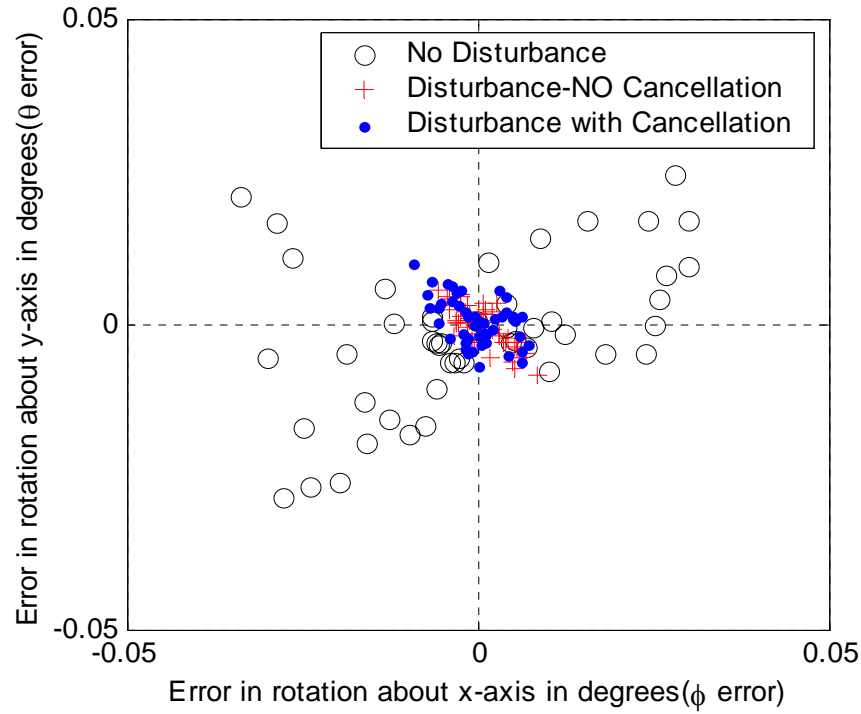


Figure 75 Pointing Error for 0.1° Radius Circular Trajectory at a Speed 0.1 Hz

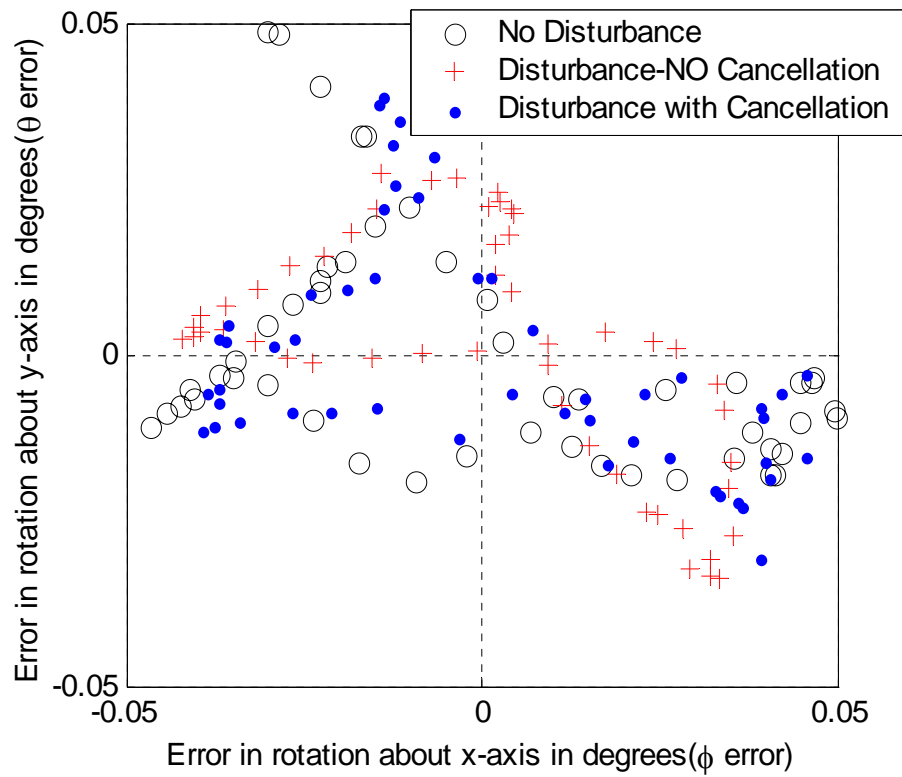


Figure 76 Pointing Error for 1.0° Radius Circular Trajectory at a Speed 0.1 Hz

b. 2 Hz Circle Trajectory

Similar to the results corresponding to the tracking of the slow circular trajectory, Figure 77 illustrates that for the fast circular trajectory with a disturbance and without cancellation (0.1° radius), the pointing error was actually reduced when the disturbance was present. However, unlike tracking a slow trajectory, the pointing accuracy with the ADC on was identical to the disturbance-free case. Also similar to the slow tracking trajectory, any pointing accuracy improvements observed with the disturbance on, were no longer present once the trajectory reached a 1.0° radius as seen in Figure 78. The pointing accuracy was $\pm 0.05^\circ$ for the 0.1° radius circular trajectory and degraded to $\pm 0.17^\circ$ for the 1.0° radius circular trajectory at 2 Hz with the cancellation applied. As with the 0.1 Hz circular trajectories, for all cases tested, pointing accuracy with a payload disturbance was not degraded beyond that seen in the disturbance free case. In general, as was seen in the disturbance-free cases of Chapter IV, during dynamic tracking tasks, the smaller or slower the circular trajectory, the smaller the pointing error.

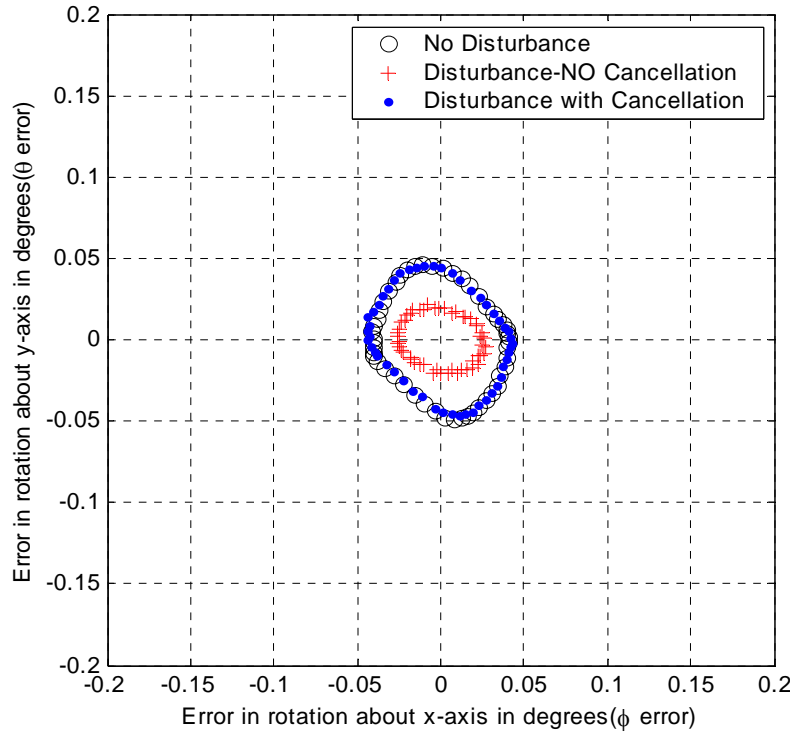


Figure 77 Pointing Error for 0.1° Radius Circular Trajectory at a Speed 2.0 Hz

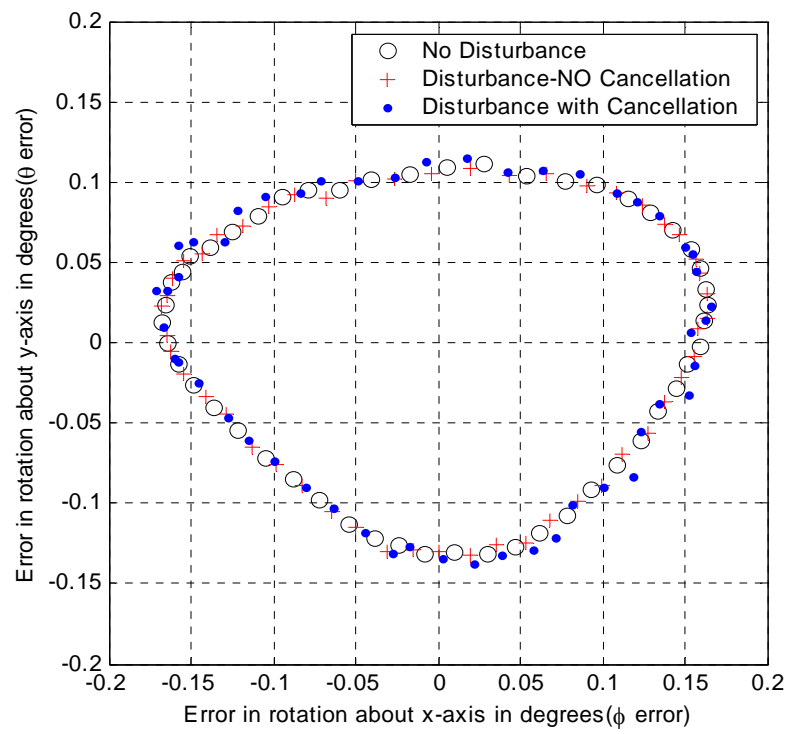


Figure 78 Pointing Error for 1.0° Radius Circular Trajectory at a Speed 2.0 Hz

THIS PAGE INTENTIONALLY LEFT BLANK

VI. CONCLUSIONS AND RECOMMENDATIONS

A. CONCLUSIONS

In conclusion, all of the objectives of this thesis were met. These included the development and experimental evaluation of both a small angle and large angle pointing controller using a PID compensator and payload platform mounted displacement sensors, and the combination of the small angle controller with the previously developed Adaptive Disturbance Canceller (ADC) for combined pointing and vibration suppression tasks. The following sections describe the specific conclusions as a result of this research.

1. Precision Pointing

From very early on during this research it was determined that the open loop performance of the PPH with either the dynamically derived (using a finite element model), manufacturer provided, transformation matrix or the kinematically derived Jacobian matrix was not acceptable for any type of precision pointing application due to pointing accuracies that were as poor as $\pm 0.5^\circ$. Incorporating the payload platform displacement sensors and a PID compensator resulted in significant improvements in pointing accuracy for both controllers. Pointing accuracy for fixed platform orientations was improved down to $\pm 0.008^\circ$ and pointing accuracy for dynamic tracking tasks ranging from $\pm 0.05^\circ$ to $\pm 0.2^\circ$ was achieved, depending on the size and speed of the circular trajectory commanded. There were however, several confounding issues that arose from the implementation of these controllers.

One such issue was the motion in the unconstrained degrees of freedom. As the payload platform rotated about the x or y-axis, there possibly existed a translation about the x, y, and/or z-axis and a twisting about the z-axis that was neither measured, nor accounted for in the controller. These motions made using the payload platform mounted laser and position sensing diode useless at rotations greater than $\pm 0.25^\circ$ and represented payload platform motion that would ultimately affect the pointing accuracy of the payload if implemented on an actual satellite. Another issue was that the large angle controller was physically restricted by the capability of the PPH and the

measurement range of the displacement sensors to $\pm 2.4^\circ$, thus limiting its evaluation at truly large angles ($>10^\circ$). This controller did, however, perform as well as the small angle controller for the given range of motion of the PPH, even though it was computationally more intensive.

Both PID compensators that were evaluated performed as expected. The modified PID compensator demonstrated equal pointing performance when compared to the standard compensator while eliminating the audible, high frequency noise created by the standard compensator. The drawback to these compensators, as with any PID compensator, was that a new set of gains was required for different payload configurations or if different tracking speeds were used. Most of the pointing errors observed appeared to be repeatable and possibly were a result of static friction within the PPH actuators. The presence of this static friction was a significant hinderance to achieving truly precise pointing (author defines as less than $\pm 0.001^\circ$). The hunting phenomenon, common to PID compensators in the presence of static friction, was clearly evident in the data. As a result, pointing errors varied at approximately 1 Hz even during poses with a fixed orientation, and accuracies less than $\pm 0.005^\circ$ were not possible.

2. Combined Vibration Suppression and Precision Pointing

The ADC and the small angle controller worked well together. Vibration suppression of a single tone disturbance down to the noise floor and a reduction of g_{rms} by a factor of at least 2.7 was achieved during all static pointing tasks evaluated. This validated the past performance of the ADC from reference [5] and demonstrated its capability to suppress vibrations at off-nominal orientations up to the maximum angle of rotation tested ($\pm 1.0^\circ$) about either axis. Furthermore, no less than a 20 dB reduction in the fundamental disturbance energy and a factor of two reduction in g_{rms} was achieved during all dynamic tracking experiments. Finally, the most interesting observation of the combined vibration suppression and precision pointing experiments was that the pointing errors were actually reduced for both fixed orientation and dynamic tracking tasks in the presence of a disturbance. This is most likely due to the reduction in static friction at the actuator bushings caused by the disturbance.

B. RECOMMENDATIONS

The recommendations for future work are all derived from the desire/need to improve the pointing accuracy of the PPH. At a minimum, the PID compensators gains should be optimized to give the best performance (smallest pointing error) over the largest range of tracking speeds. This refinement to the existing controllers is insignificant however, when compared to the problem of static friction. One course of action to address this problem would be to replace the actuator bushings with less resistive ones, this however, would not eliminate the problem completely. Modeling the static friction and including a robust static friction compensator to the controller would also be required to improve the pointing accuracy. Additionally, an adaptive compensator to handle the repetitive errors experienced during the dynamic tracking tasks, potentially as a result of static friction, could also be implemented to remove many of the pointing errors observed in this research. The modeling of the flexible joint dynamics and actuator voice coil dynamics could also prove to be beneficial in improving transient pointing performance and in improving the accuracy of dynamic tracking tasks both with and without vibration suppression. Finally, the translational/twist motion of the payload platform along/about the x and/or y-axes must be verified. If observed, this motion must be controlled if the payload-mounted sensors were to really be considered as a viable means of providing feedback of the payload orientation.

THIS PAGE INTENTIONALLY LEFT BLANK

LIST OF REFERENCES

-
- [1] S.J. Elliot, I.M. Stothers, and P.A. Nelson, "A Multiple Error LMS Algorithm and its Application to the Active Control of Sound and Vibration," in IEEE Transactions on Acoustics, Speech, and Signal Processing, number 10 in ASSP-35, pp 1432-1434, October 1987.
 - [2] Stephen G. Edwards, "Active Narrowband Disturbance Rejection on an Ultra Quiet Platform," PhD Dissertation, Naval Postgraduate School, September 1999.
 - [3] H. J. Chen and R. W. Longman, B.N. Agrawal, and M.P. Phan, "Frequency Domain Clear Box Disturbance Rejection on an Ultra Quiet Platform," in Advances in the Astronautical Sciences, Vol. 105 (Part I), 2000, Proceedings of the 10th AAS/AIAA Space Flight Mechanics Meeting, pp 73-92, January 23-26, 2000.
 - [4] H. J. Chen, R. W. Longman, B. N. Agrawal, M. Q. Phan, S. G. Edwards, "Rejection of Multiple Unrelated Periodic Disturbances Using MELMS with Disturbance Identification," Advances in the Astronautical Sciences, Vol. 108 (Part I), 2001, Proceedings of the 11th AAS/AIAA Space Flight Mechanics Meeting, pp 587-606, February 11-15 2001.
 - [5] Christian Taranti, "A Computationally Efficient Algorithm for Disturbance Cancellation to Meet the Requirements for Optical Payloads in Satellites," PhD Dissertation, Naval Postgraduate School, September 2001.
 - [6] Richard G. Cobb, Jeanne M. Sullivan, Alok Das, L Porter Davis, T. Tupper Hyde, Torey Davis, Zahidul H Rahman, and John T. Spanos, "Vibration Isolation and Suppression System for Precision Payloads in Space," Smart Material Structures, pp 798-812, 1999.
 - [7] Z. Rahman, J. Spanos, R. Laskin, "A Six-Axis Vibration Isolation, Suppression and Steering System for Space Applications," AIAA35th Aerospace Sciences Meeting and Exhibit, January 1997.
 - [8] Jeanne Sullivan, Zahidul Rahman, Richard Cobb, John Spanos, "Closed-Loop Performance of a Vibration Isolation and Suppression System," Proceedings of the American Control Conference, pp3974-3978, June 1997.
 - [9] James R. Wertz and Wiley J. Larson, "Space Mission Analysis and Design Third Edition," Space Technology Library, Microcosm Press, 1999.
 - [10] Hughes Corporation, www.hughespace.com, February 1990.
 - [11] NASA site, www.earth.nasa.gov , April 1999.

-
- [12] Ben K. Wada, Zahidul Rahman, Roland Kedikian, and C.P. Kuo, "Vibration Isolation, Suppression, and Steering (VISS)," *Journal of Intelligent Material System and Structures*, Vol. 7, pp 241-245, March 1996.
- [13] Massachusetts Institute of Technology site, ssl.mit.edu/programs/flight/mace.html, 2001.
- [14] Porter Davis, Delano Carter, T. Tupper Hyde, "Second Generation Hybrid D-Strut," SPIE Smart Structures and Materials Conference, February 1995.
- [15] Haomin Lin & John E. McInroy, "Adaptive Sinusoidal Disturbance Cancellation Strategy for Pointing Applications," *Proceedings of the 39th IEEE Conference on Decision and Control*, pp 1451-1452, December 2000.
- [16] V.E. Gough and S.G. Whitehall, "Universal Tyre Test Machine," *Proceedings of 9th International Technical Congress, F.I.S.I.T.A. (Institute of Mechanical Engineering)*, p 170, 1962.
- [17] D. Stewart, "A Platform with Six Degrees of Freedom," *Proceedings of Institute of Mechanical Engineering*, vol. 180, pp 371-386, 1965.
- [18] Lung-Wen Tsai, "Robot Analysis," John Wiley & Sons, Inc, 1999.
- [19] J.P. Merlet, "Parallel Manipulators Part I: Theory, Design, Kinematics, Dynamics and Control," INRIA Report, 1987.
- [20] E.F. Fichter, "A Stewart Platform Based Manipulator: General Theory and Practical Construction," *International Journal of Robotic Research*, vol. 5, no.2, pp 157-182, 1986.
- [21] W.Q.D. Do and D.C.H. Yang, "Inverse Dynamic Analysis and Simulation of a Platform Type Robot," *Journal of Robotic Systems*, vol. 5, no. 3, pp. 209-227, 1988.
- [22] Z. Geng, L. S. Haynes, J. D. Lee, and R. L. Carroll, "On the Dynamic Model and Kinematic Analysis of a Class of Stewart Platforms," *Robotics and Autonomous Systems*, 9, pp.237-254, 1992.
- [23] K. Liu, M. Fitzgerald, D.W. Dawson, F.L. Lewis, "Modelling and Control of a Stewart Platform Manipulator," *ASME DSC vol. 33, Control of Systems with Inexact Dynamic Models*, pp. 83-89, 1991.
- [24] Zhiming Ji, "Study of the Effect of Leg Inertia in Stewart Platforms," in *Proceedings of the IEEE International Conference of Robotics and Automation*, Vol.1, pp. 121-126, 1993.

-
- [25] B. Dasgupta and T.S. Mruthyunjaya, "A Newton-Euler Formulation for the Inverse Dynamics of the Stewart Platform Manipulator," *Mechanical Machine Theory*, Vol. 35, no. 8, pp. 1135-1152, 1998.
- [26] Claudio Pernechele, Favio Bortoletto, and Enrico Giro, "Neural Network Algorithm Controlling a Hexapod Platform," *IEEE*, 2000.
- [27] R. Scott Erwin and Leslie A. Sullivan, "Vibration Isolation, Supression, and Steering (VISS) Flight Experiment," Presentation at AFRL, 2001.
- [28] Eric H. Anderson, Michael E. Evert, Roger M. Glaese, James C. Goodding, and Scott C. Pendleton, Donald Camp, John Fumo, Marty Jessen, Richard G. Cobb, R. Scott Erwin, and Jonathan Jensen, "Satellite Ultraquiet Isolation Technology Experiment (SUITE): Electromechanical Subsystems," in *SPIE Conference on Industrial and Commerical Application of Smart Structures Technologies*, vol. 3674, pp 308-328, Newport Beach, CA, March 1999.
- [29] John E. McInroy, John F. O'Brien, and Gregory W. Neat, "Precise, Fault-Tolerant Pointing Using a Stewart Platform," *IEEE/ASME Transactions on Mechatronics*, vol. 4, no. 1, pp 91-95, March 1999.
- [30] John E. McInroy, J.F. O'Brien, G.W. Neat, "Method and Experimental Validation of a Precision, Reconfigurable Pointing Control Strategy," *Proceedings of the 36th Conference on Decision and Control*, pp. 3990-3995, December 1997.
- [31] John E. McInroy, Gregory W. Neat, and John F. O'Brien, "A Robotic Approach to Fault-Tolerant Precision Pointing," *IEEE Robotics & Automation Magazine*, pp 24-37, December 1999.
- [32] John E. McInroy and Jerry C. Hamann, "Design and Control of Flexure Jointed Hexapods," *IEEE Transactions on Robotics and Automation*, vol. 16, no. 4, pp 372-381, August 2000.
- [33] Haomin Lin & John E. McInroy, "Adaptive Sinusoidal Disturbance Cancellation Strategy for Pointing Applications," *Proceedings of the 39th IEEE Conference on Decision and Control*, pp 1451-1452, December 2000.
- [34] Eric M. Flint, PHEX-1 (Type 1 Pointing Hexapod) User Guide, CSA Engineering, Inc., 2565 Leghorn Street, Mountain View, CA, Aug 2000.
- [35] E. Bertran and G. Montoro, "Adaptive Suppression of Narrow-Band Vibrations," in *5th International Workshop on Advanced Motion Control*, pp. 288-292, June-July 1998.
- [36] KD2300 Instruction Manual, Kaman Instrumentation Corporation, 1996.

-
- [37] C. Canudas de Wit, H. Olsson, K.J. Astrom, and P. Lischinsky, "A New Model for Control of Systems with Friction," *IEEE Transactions of Automatic Control*, vol. 40, no. 3 pp 419-425, March 1995.

APPENDIX A

This appendix includes the Matlab code written by CSA Engineering, the manufacturers of the Precision Pointing Hexapod, to determine the transformation matrix of the hexapod. The code develops a finite element model of the hexapod, then determines the natural frequencies and transformation matrix of the hexapod at its nominal position. The normalized manufacturer-provided transformation matrix calculated from this program, which was used in this research, is shown below:

$$\begin{bmatrix} -0.49954 & 1.00000 & 1.00000 & -0.32816 & 1.00000 & 1.00000 \\ 1.00000 & 0.00035 & 1.00000 & -1.00000 & -0.20603 & -1.00000 \\ -0.50046 & -0.99929 & 1.00000 & -0.67282 & -0.79397 & 1.00000 \\ -0.50046 & 0.99929 & 1.00000 & 0.67282 & -0.79397 & -1.00000 \\ 1.00000 & -0.00035 & 1.00000 & 1.00000 & -0.20603 & 1.00000 \\ -0.49954 & -1.00000 & 1.00000 & 0.32816 & 1.00000 & -1.00000 \end{bmatrix}$$

MAIN PROGRAM EIG_AND_TF

% This code calculates the nominal eigenvalues and transformation matrices for a generic hexapod about its nominal centered operating position. Variables are as defined in P1 Users Manual.

% Hexapod Configuration variables

rua = 4.5*2.54/100 % meters (m preferred)
rla = 4.5*2.54/100 % meters (m preferred)
h = (10.175-2.35)*2.54/100 % meters (m preferred)
dtu = 25/2 % 1 sided angle, degrees (deg required)
dtl = 25.1/2 % 1 sided angle, degrees (deg. required) cannot = dtu!

% Passive isolator details

kps = 2350 % 275610.31, N/m (N/m preferred)
cps = 0.1 % unitless (damping)

% Payload variables, original values

xcg = [0, 0, 0]; % (m) center of gravity not including struts!!!
M_pay = 4.2; % (Kg) payload only excluding struts
Ixy_pay = 0; % -8.196e-6; % (Kg*m^2)
Ixz_pay = 0; % 1.915e-6; % (Kg*m^2)
Iyz_pay = 0; % -2.254e-3; % (Kg*m^2)

% Build Mass matrix

M=zeros(6);
M(1:3,1:3) = M_pay*diag([1 1 1]);
M(4,4) = 0.039; % Ixx payload (Kg*m^2) payload only, excluding struts !!!
M(5,5) = 0.039; % Iyy payload (Kg*m^2) payload only, excluding struts !!!
M(6,6) = 0.046; % Izz payload (Kg*m^2) payload only, excluding struts !!!
M(4,5) = Ixy_pay;
M(4,6) = Ixz_pay;
M(5,6) = Iyz_pay;
M(5,4) = Ixy_pay;
M(6,4) = Ixz_pay;
M(6,5) = Iyz_pay;

% Build additional information

stewgeom

% calculate eigenvalues

M6 = M;% Mass Matrix
K6=kps*Ts_r;% Stiffness Matrix
C6=cps*Ts_r;% Damping Matrix

```

% generation of the 6 dof rigid body plant matrix A
on = eye(size(K6));
ze = zeros(size(K6));
A = [ze on ; -inv(M6)*K6 -inv(M6)*C6];

% determination of eigenvalues
[V,D] = eig(A);
r = diag(D);
wn = abs(r);
z = -cos(atan2(imag(r),real(r)));

% Sorted eigenvalues
rs = esort(r);
wns = abs(rs);
zs = -cos(atan2(imag(rs),real(rs)));
ev=abs(V);

% print out damping and natural frequencies
disp("")
disp('          Eigenvector Components')
disp(' Freq. (Hz) X      Y      Z      MX      MY      Mz')
disp("")
j=1;
for j=1:2:11
    disp([wn(j)/(2*pi),ev(7:12,j)'])
end

% Transformation Matrix from Strut to cg
uvx= suv(:,1)';
uvy=suv(:,2)';
uvz=suv(:,3)';

delx=(xcg(1)-u(:,1))';
dely=(xcg(2)-u(:,2))';
delz=(xcg(3)-u(:,3))';

Fs2cg=[uvx;uvy; uvz; uvy.*delz-uvz.*dely; -uvx.*delz+uvz.*delx; uvx.*dely-uvy.*delx];
Fcg_max=[sum(abs(Fs2cg(1,:)))      sum(abs(Fs2cg(2,:)))      sum(abs(Fs2cg(3,:)))
sum(abs(Fs2cg(4,:))) sum(abs(Fs2cg(5,:))) sum(abs(Fs2cg(6,:)))']';

% AS defined in PH-1 Users Manual
Transformation_Matrix = Fs2cg'

```

FUNCTION STEWGEOM

```
% stewgeom(rua,rla,h,dtu,dtl)
% calculates the geometry and various transformation matrices of a stewart platform
% based on the basic variables
% unit system: doesn't matter, mks preferred
%
% Coordinate system is defined in cartesian coordinates
% Stewart platform XYZ locus is defined as the center of the actual upper platform ring,
% with the x axis aligned through the nominal middle of the u1-u6 connection point.
%
% input
% rua Actual radius of upper platform (currently assumed narrower)
% rla Actual radius of lower platform (currently assumed wider)
% h Separation between actual upper and lower rings
% dtu Delta theta upper(in deg.) One sided angle spread from the nominal
%      (accomodates actuator separation) (must be between 0 and 30)
% dtl Delta theta lower(in deg.) One sided angle spread from the nominal
%      (accomodates actuator separation) (must be between 0 and 30)
% xcg Center of gravity of rigid payload
%
% output
% u Definition of upper connector points (rows are connector #, columns are x,y,z
point
% l Definition of lower connector points (rows are connector #, columns are x,y,z
point)
% suv Strut unit vectors (rows are strut #, columns are x,y,z unit vector component)
% Ts_r Transformation matrix from input along a strut(s) axis to rigid(r) mass 6 d.o.f.
response at defined locus
%
% Strut definitions
% s1 : between points u1 and l1
% s2 : between points u2 and l2
% s3 : between points u3 and l3
% s4 : between points u4 and l4
% s5 : between points u5 and l5
% s6 : between points u6 and l6

%XXXXXXXXXXXXXXXXXXXXXXXXXXXXXXXXXXXXXXXXXXXXXXXXXXXXXXXXXXXXX
% definition of actual strut connection point location in local x,y,z coordinates
% upper strut points (uX)
u1 = [rua*cos((0+dtu)*pi/180),rua*sin((0+dtu)*pi/180),0];
u2 = [rua*cos((120-dtu)*pi/180),rua*sin((120-dtu)*pi/180),0];
u3 = [rua*cos((120+dtu)*pi/180),rua*sin((120+dtu)*pi/180),0];
u4 = [rua*cos((240-dtu)*pi/180),rua*sin((240-dtu)*pi/180),0];
u5 = [rua*cos((240+dtu)*pi/180),rua*sin((240+dtu)*pi/180),0];
u6 = [rua*cos((0-dtu)*pi/180),rua*sin((0-dtu)*pi/180),0];
```

```

u=[u1;u2;u3;u4;u5;u6];

%lower strut points (IX)
l1 = [rla*cos((60-dtl)*pi/180),rla*sin((60-dtl)*pi/180),-h];
l2 = [rla*cos((60+dtl)*pi/180),rla*sin((60+dtl)*pi/180),-h];
l3 = [rla*cos((180-dtl)*pi/180),rla*sin((180-dtl)*pi/180),-h];
l4 = [rla*cos((180+dtl)*pi/180),rla*sin((180+dtl)*pi/180),-h];
l5 = [rla*cos((300-dtl)*pi/180),rla*sin((300-dtl)*pi/180),-h];
l6 = [rla*cos((300+dtl)*pi/180),rla*sin((300+dtl)*pi/180),-h];
l=[l1;l2;l3;l4;l5;l6];

% strut midpoint (or c.g.) calculations
m1=(u1+l1)/2;
m2=(u2+l2)/2;
m3=(u3+l3)/2;
m4=(u4+l4)/2;
m5=(u5+l5)/2;
m6=(u6+l6)/2;

% old sanity checks
% combination for plotting in 3d format
legplot=[u1;l1;l2;u2;u3;l3;l4;u4;u5;l5;l6;u6;u1];

% sanity check
% plot points on three-d plot
% plot3(legplot(:,1),legplot(:,2),legplot(:,3));

% strut unit vectors
suv1=uv(u1,l1);
suv2=uv(u2,l2);
suv3=uv(u3,l3);
suv4=uv(u4,l4);
suv5=uv(u5,l5);
suv6=uv(u6,l6);
suv=[suv1;suv2;suv3;suv4;suv5;suv6];

% unit vector definitions
ux=[1 0 0];
uy=[0 1 0];
uz=[0 0 1];

% strut

% strut rotational transformation matrices
% C1=[dot([suv1(1) 0 0],ux) dot([suv1(1) 0 0],uy) dot([suv1(1) 0 0],uz);
%     dot([0 suv1(2) 0],ux) dot([0 suv1(2) 0],uy) dot([0 suv1(2) 0],uz);

```

```

%      dot([0 0 suv1(3)],ux) dot([0 0 suv1(3)],uy) dot([0 0 suv1(3)],uz)];
C1 = diag(suv1,0);
C2 = diag(suv2,0);
C3 = diag(suv3,0);
C4 = diag(suv4,0);
C5 = diag(suv5,0);
C6 = diag(suv6,0);

% Transformation Matrix
% 6 Axis Strut -Rigid 6DOF
Ts_r=zeros(6);
topology =      [1 2 3 4 5 6;...
                  1 2 3 4 5 6];
for i=1:6;
    eval(['x1 = u',num2str(topology(1,i)),';']);
    eval(['x2 = l',num2str(topology(2,i)),';']);
    [matrix] = strut1(xcg,x1,x2,[0 0 0]);
    Ts_r=Ts_r+matrix;
end
% XXXXXXXXXXXXXXXXXXXXXXXXXXXXXXXXXXXXXXXXXXXXXXXXXXXXXXXXXXXXXXX

```

FUNCTION CROSS2

```

function [y]= cross2(u,v)
y = zeros(1,3);
y(1) = det([u([2 3]);v([2 3])]);
y(2) = -det([u([1 3]);v([1 3])]);
y(3) = det([u([1 2]);v([1 2])]);

```

FUNCTION INERTIATRANS

```

function [T]=inertiATRANS(p1,p2)
% taken from Rogers book
%
%p1: point 1 (in x,y,z coordinates)
%p2: point 2 (in x,y,z coordinates)

abc=(p1-p2);
a= abc(1);
b= abc(2);
c= abc(3);
T=[b^2+c^2 -a*b -a*c; -a*b c^2+a^2 -b*c; -a*c -b*c a^2+b^2];

```


FUNCTION STRUT1

```
function [return_matrix] = strut1(xcg,x1,x2,xv)

% Created on: 12/2/97
% Created by: Eric Flint
% Modified from: strut.m of Smitty
% function [return_matrix] = strut1(xcg,x1,x2,xv)
%
% This function computes the basic matrix of a given strut with respect to
% a global 6 dof reference system. The two ends of the strut element are specified
% by the points x1 (node number n1) and x2 (node number n2). The bar
% geometry, element coordinate system and roll axis orientation are described
% using the two end points and an orientation vector xv. The tail of this
% vector coincides with point x1.

K=zeros(6);
K_strut=K;
return_matrix=K;

Length = sqrt((x2-x1)*(x2-x1));
Lambda = cordtran(x1,x2,xv);
K = Lambda(:,1)*1*Lambda(:,1)';
K_strut(1:3,1:3) = K;

a = x2-xcg;
K_strut(1,4:6)=cross2(a,K(1,:));
K_strut(2,4:6)=cross2(a,K(2,:));
K_strut(3,4:6)=cross2(a,K(3,:));
K_strut(4:6,1:3)=K_strut(1:3,4:6)';

K_strut(4,4) = K(2,2)*a(3)^2+K(3,3)*a(2)^2 -2*K(3,2)*a(2)*a(3);
K_strut(4,5) = K(1,3)*a(2)*a(3) + K(2,3)*a(1)*a(3) - K(3,3)*a(1)*a(2)...
    - K(2,1)*a(3)^2;
K_strut(4,6) = K(1,2)*a(2)*a(3) + K(2,3)*a(1)*a(2) - K(2,2)*a(1)*a(3)...
    - K(1,3)*a(2)^2;
K_strut(5,4) = K_strut(4,5);
K_strut(6,4) = K_strut(4,6);
K_strut(5,5) = K(1,1)*a(3)^2+K(3,3)*a(1)^2 -2*K(3,1)*a(1)*a(3);
K_strut(6,6) = K(1,1)*a(2)^2+K(2,2)*a(1)^2 -2*K(2,1)*a(1)*a(2);

return_matrix=K_strut;
```

FUNCTION UV

```
function [unit_vector] = uv(p1,p2)

% y =uv(p1,p2)
% This function takes the two given points and computes the unit vector (or direction
% cosines, if you will) routine calculates the unit vector (or for those who like it, the
% direction cosines) of the lines between the points.
%
% Points: p1, p2, should be defined in a x,y,z cartesian coordinate and passed to this
% function as a vector

uv_a= p2(1) - p1(1);
uv_b= p2(2) - p1(2);
uv_c= p2(3) - p1(3);

uv_l=sqrt(uv_a^2+uv_b^2+uv_c^2);

unit_vector=[uv_a/uv_l, uv_b/uv_l, uv_c/uv_l ];
```

FUNCTION COSIN

```
% This routine computes the cosin of the the angle between
% two vectors. It returns zero if one or both vectors is the
% zero vector.
% Calls Made: none
% Called By: cordtran.m

function y = cosin(u,v);

if (u==0 | v==0)
    y = 0;
else
    y = u*v'/(sqrt(u*u')*sqrt(v*v'));
end
```

FUNCTION CORDTRAN

```
function Lambda = cordtran(x,y,vec)
```

```
% y = cordtran(x,y,z)
```

% This function considers two points in space and a vector. The first point x defines the origin of a second coordinate system. The first two points (x,y) define a vector which corresponds to the x axis of this new coordinate system. The tail of the vector (vec) is situated on the point x. The z-axis of the second coordinate system is then defined as the cross product of the two vectors. Finally the y-axis of the new system is defined as the cross product of the two unit vectors in the new system.

```
%
```

% The coordinate transformation which relates the global coordinate system (in which the points are defined) to the secondary system (defined by the three points) is then defined and yields the output.

```
% Called by: strut.m
```

```
% Calls Made: cosin.m
```

```
u = y-x;
```

```
% Define the normal to the plane spanned by u and v
```

```
w = cross(u,vec);
```

```
% ... and an additional vector orthogonal to u and w
```

```
v = cross(w,u);
```

```
% Normalize
```

```
if u==0
```

```
    uN = 0;
```

```
else
```

```
    uN = u/sqrt(u*u');
```

```
end
```

```
if w==0
```

```
    wN = 0;
```

```
else
```

```
    wN = w/sqrt(w*w');
```

```
end
```

```
if v==0
```

```
    vN = 0;
```

```
else
```

```
    vN = v/sqrt(v*v');
```

```
end
```

```
y = zeros(3);
```

```
e1 = [1 0 0];
```

```
e2 = [0 1 0];
```

```
e3 = [0 0 1];
```

```
Lambda(1,1:3) = [cosin(e1,uN) cosin(e1,vN) cosin(e1,wN)];
```

```
Lambda(2,1:3) = [cosin(e2,uN) cosin(e2,vN) cosin(e2,wN)];
```

```
Lambda(3,1:3) = [cosin(e3,uN) cosin(e3,vN) cosin(e3,wN)];
```

```
function [return_matrix]=struttrans(xcg,x1,x2)

%
% function struttrans(xcg,x1,x2)
% this file generates the transformation matrix of a generic pinned strut element
% from the local uniaxial geometry to the global rigid body 6 dof.
% Used primarily for computing transformation of axial forces to global forces
% and moments
%
% input = geometry
%     xcg = coordinates of global cg. (in x,y,z)
%     x1 = coordinates of point 1 (in x,y,z)
%     x2 = coordinates of point 2 (in x,y,z)
%
% output = transformation matrix between uniaxial input and rigid body 6 dof exciation
%     return_matrix
%
%%%%%%%%%%%%%%%%%%%%%%%%%%%%%%%%%%%%%%%%%%%%%%%%%%%%%%%%%%%%%%%%%%%%%%%%%%%%%%

% calculations
uv1 = uv(x1,x2);

%matrix 1: tranformation from local axial to local 3dof.
matrix1=[uv1 0 0 0];

%matrix 2: tranformation from local 3dof to global rigid body 6dof
matrix2=strut1(xcg,x1,x2,[0 0 0]);

return_matrix = matrix2*matrix1';
```

INITIAL DISTRIBUTION LIST

1. Defense Technical Information Center
Ft. Belvoir, VA
2. Dudley Knox Library
Naval Postgraduate School
Monterey, CA
3. Department Chairman
Department of Aeronautics and Astronautics
Monterey, CA
4. Professor Brij N. Agrawal
Department of Aeronautics and Astronautics
Monterey, CA
5. Dr. Hong-Jen Chen
Department of Aeronautics and Astronautics
Monterey, CA
6. SRDC Research Library
Department of Aeronautics and Astronautics
Monterey, CA
7. LCDR Ronald Bishop, USN
Warrenton, VA